ANALYSIS OF EQUILIBRIUM AND TOPOLOGY OF TOKAMAK PLASMAS

ANALYSE VAN EVENWICHT EN TOPOLOGIE VAN TOKAMAK PLASMAS

(MET EEN SAMENVATTING IN HET NEDERLANDS)

PROEFSCHRIFT

TER VERKRIJGING VAN DE GRAAD VAN DOCTOR IN DE WISKUNDE EN NATUURWETENSCHAPPEN AAN DE RIJKSUNIVERSITEIT TE UTRECHT, OP GEZAG VAN DE RECTOR MAGNIFICUS PROF. DR. J.A. VAN GINKEL, VOLGENS BESLUIT VAN HET COLLEGE VAN DECANEN IN HET OPENBAAR TE VERDEDIGEN OP WOENSDAG 20 NOVEMBER 1991 DES NAMIDDAGS TE 2.30 UUR

DOOR

BOUDEWIJN PHILIP VAN MILLIGEN

GEBOREN OP 25 AUGUSTUS 1964 TE VUGHT

DRUKKERIJ ELINKWIJK – UTRECHT

Table of contents

			page
1	**Introduction**		**1**
	1.1	Plasma	1
	1.2	Fusion and fusion research	1
	1.3	The tokamak	2
	1.4	This thesis	5
	1.5	Publications produced in the course of this work	8
2	**MagnetoHydroDynamics**		**11**
	2.1	Introduction	11
	2.2	Coordinate systems	11
	2.3	Representation of the magnetic field	12
		2.3.1 The flux function	12
		2.3.2 Toroidal symmetry	13
	2.4	The plasma model	14
		2.4.1 The macroscopic description	14
		2.4.2 The one-fluid description	14
		2.4.3 The assumption of quasi-neutrality	17
		2.4.4 The assumption of quasi-static flow	18
		2.4.5 The assumption of low collisionality	19
		2.4.6 The ideal MHD model	19
	2.5	Solving the ideal MHD equations	21
		2.5.1 General considerations	21
		2.5.2 A conventional equilibrium solver method	22
	2.6	Analogy with fluid dynamics	24
		2.6.1 Analogy between Ideal MHD and Fluid Dynamics	24
		2.6.2 Analogy between Resistive MHD and Viscous Fluid Dynamics	24
	2.7	MHD modes and stability	26
		2.7.1 The safety factor	26
		2.7.2 Tearing modes	26

3 Multipole and current moments **29**

3.1 Introduction 29

3.2 Exact relations between multipole moments of the flux and moments of the toroidal current density in tokamaks 30

3.2.1 Abstract 30

3.2.2 Introduction 31

3.2.3 Toroidal coordinates and multipole moments 32

3.2.4 Expression of current moments in terms of multipole moments 33

3.2.5 Acknowledgements 37

3.3 Interpretation of the current moments 38

3.3.1 Approximation of the current density profile from the current moments 38

3.3.2 Definition of characteristic parameters from the current moments 40

3.4 Application to RTP 41

3.4.1 Determination of multipole moments from the measurements 41

3.4.2 Sensitivity to measurement errors of multipole and current moments 42

3.4.3 Reconstruction of the magnetic field at RTP 47

3.5 Discussion 48

4 Function parametrization **49**

4.1 Introduction 49

4.2 Function Parametrization: a fast inverse mapping method 50

4.2.1 Abstract 50

4.2.2 Introduction 51

4.2.3 Theory of Function Parametrization 52

4.2.3.1 Introduction 52

4.2.3.2 Dimension reduction 53

4.2.3.3 Regression 58

4.2.3.4 Error Analysis 60

4.2.4 Application to the RTP tokamak 62

4.2.4.1 Introduction 62

4.2.4.2 Parametrization 64

4.2.4.3 Principal Component Analysis 65

4.2.4.4 Regression and error analysis 66
4.2.4.5 Results 69
4.2.5 Summary and Conclusions 71
4.2.5.1 Principle and Advantages of Function Parametrization 71
4.2.5.2 Power and Limitations of Function Parametrization 71
4.2.5.3 Application to Tokamak Physics: RTP 72
4.2.5.4 Conclusions 72
4.2.6 Appendix 73
4.2.6.1 Database generation: Method of parameter selection 73
4.2.6.2 Database generation (RTP) 74
4.2.6.3 Table of notation 75
4.2.7 Acknowledgements 75
4.3 Application of Function Parametrization to the Analysis of Polarimetry and Interferometry data at TEXTOR 76
4.3.1 Abstract 76
4.3.2 Introduction 77
4.3.3 Interferometry and polarimetry at TEXTOR 78
4.3.4 Data analysis 80
4.3.4.1 Conventional method 80
4.3.4.2 Function Parametrization 81
4.3.5 Application to TEXTOR data and comparison to Method I 88
4.3.6 Discussion 91
4.3.6.1 Results for discharge # 14214 91
4.3.6.2 Future extensions of the method 93
4.3.7 Acknowledgements 94

5 The safety factor and MHD mode activity 95
5.1 Introduction 95
5.2 Methods used in the analysis of MHD activity 95
5.3 MHD activity and density limit disruptions at RTP 98
5.4 Observation of pressure inside magnetic islands at JET 107
5.5 Shear reversal and MHD activity during Pellet Enhanced Performance plasmas in JET 109

5.5.1 Abstract 109
5.5.2 Introduction 110
5.5.3 Diagnostics and data analysis 111
5.5.3.1 Diagnostics 111
5.5.3.2 Data analysis and correlation between diagnostics 112
5.5.4 Results and discussion 112
5.5.4.1 A typical PEP H-mode shot 112
5.5.4.2 MHD behaviour during the PEP phase 114
5.5.4.3 Determination of the q-profile 115
5.5.4.4 Transport simulation of the PEP mode 119
5.5.4.5 Mode stability computation 121
5.5.4.6 Topology of a rotating (m,n) = (1,1) mode 123
5.5.5 Conclusions 127
5.5.6 Acknowledgements 128

References 129

Appendix: Table of symbols and definitions 137

Samenvatting 139

Curriculum Vitae 141

Dankwoord / Acknowledgements 143

PROPOSITIONS
(Stellingen)

Submitted in conjuction with the thesis
Analysis of equilibrium and topology of tokamak plasmas
by B.Ph. van Milligen

Utrecht, 20 november 1991

(1) The perturbed electron temperature inside magnetic islands depends on the the local value of the shear and can be either higher or lower than the environment temperature; the electron density and pressure perturbations, however, display no such dependency on the shear.
This thesis, chapter 5.

(2) Radial transport is significantly reduced in regions of negative shear.
This thesis, chapter 5.

(3) The analysis of MHD modes provides a powerful tool for local determination of the safety factor.
This thesis, chapter 5.

(4) The main obstacle in the analysis of MHD modes is not the quality of measuring equipment, nor of analysis techniques, but the availability of *fast* sampled data (i.e. > 40 kHz) from various relevant diagnostics on *overlapping* time windows *during* the occurrence of MHD phenomena.

(5) Function parametrization is a generally applicable labour saving technique for inverting computer models that can provide fast analyses with error estimates of experiments that are repeated often; therefore it deserves more attention in the physical community than it has received so far.
This thesis, chapter 4.

(6) Given the striking similarity of the equations of fluid dynamics and magnetohydrodynamics, the two branches of physics involved should work together more closely, in particular where investigations into chaos and turbulence are concerned.
This thesis, chapter 2.

(7) The great quantity of reports erroneously confirming the heat and neutron production in the electrolysis experiment of Pons and Fleischmann following their announcement in April 1990 is partly due to the fact that the difficulty of calorimetry and neutron measurement is generally underestimated.

(8) Scientific lectures would be less boring and Dutch science would be stimulated if more attention was paid on the Universities to the subject of presentation.

(9) Recent occurences in Eastern Europe allow computation of the lifetime of communist regimes at about 45 years. It is perhaps no coincidence that this is also the time for a young man to grow old.

(10) The true cause of many important ecological problems (global warming, pollution, traffic congestion etc.) is overpopulation.

(11) Raising the cost of owning or driving a car will not result in a significant reduction of car use. Therefore it is to be recommended that car use be made unattractive by other means, e.g. by severely limiting access to the areas that form the goals for excursions by car, such as city centres. As a side effect, these areas will then become more quiet, clean and beautiful.

(12) The introduction of the concept of functionality in design and architecture has not led to greater enjoyment of their products nor to an improvement in the quality of life and this concept should therefore be abandoned.

(13) Fusion remains a hot topic even after Pons and Fleischmann.

(14) Hoewel het aloude spreekwoord dat *arbeid adelt* ook heden ten dage nog opgeld doet, geldt voor het merendeel van het werk slechts dat *arbeid vermoeit*.

1. Introduction

1.1 Plasma

Conditions in the universe are quite different from those on earth. Whereas in the low-temperature earthly environment matter is primarily solid, liquid or gaseous, most observable matter in the universe (over 99%) is in the plasma state.

Natural examples of plasmas on earth are lightning (whether ball lightning is a plasma is still a matter of debate at the time of this writing) and related phenomena (sparks). Attempts to create plasmas under laboratory conditions on earth generally involve exciting a gas by heating it, applying electromagnetic radiation or passing electric currents through it until it ionizes.

Because plasmas are rare in the natural earthly environment, research into its characteristics did not start until the end of the previous century. Since then this has become an important branch of physics, and a number of successful applications for plasmas have been developed, amongst which the familiar fluorescent tube and the dry-etching process used in microchip fabrication.

1.2 Fusion and fusion research

Once it was realized that our main energy source, the sun, is a gigantic plasma and a fusion reactor kept together (confined) by its own gravitation, the question arose whether it is possible to mimic the conditions of the sun and generate energy in a similar way here on earth. It is clear, however, that a plasma in a laboratory must be confined by some other force than gravitation.

There are a number of reactions between light elements that yield energy, but some are easier to initiate than others. The light elements involved in 'easy' fusion reactions have long been used up in the sun, while they are still available on earth as relics of early cosmological processes. Profiting from this gift of nature, the goal of fusion research is to create a mixture of deuterium, D, and tritium, T, or alternatively D and helium, ^{3}He, at such temperatures and densities that fusion will occur at a sufficient rate. The reaction

$$^2\mathrm{D} + {}^3\mathrm{T} \rightarrow {}^4\mathrm{He} + {}^1\mathrm{n} + 17.6\ \mathrm{MeV},$$

the fastest reaction occurring in a fusion plasma, produces an enormous amount of energy in accordance with the mass deficit $E = mc^2$. Theoretically, 1 kg of D-T gas might yield as much

energy as ten million liters of oil. And since the raw materials (D and Li which is used to breed T) are abundant, a fusion reactor might solve the problems of energy supply for thousands of years, even at low reactor efficiencies.

Thus motivated, the European Community has set a clear goal for its fusion program: the objective is to obtain a source of energy that: (a) produces electricity at an acceptable cost while operating reliably; (b) does not produce carbon dioxide or harmful chemicals; (c) produces only a small amount of nuclear waste during normal operation and after termination of operation; (d) cannot cause disruptive accidents; (e) does not impose a large demand on scarce natural resources; and finally (f) does not have any military applications. The USA, the USSR and Japan have similar programs, and forces are joined in an international cooperation project: ITER.

1.3 The tokamak

In the course of a number of decennia several schemes were developed for generating plasmas in the required conditions (hot and dense). Amongst these are inertial or laser fusion and magnetic confinement devices of many types. The most successful concept has so far been the tokamak, originally developed in the USSR ('tokamak' is an acronym of *toroidal'naya kamera* and *magnitnaya katushka*, meaning 'toroidal chamber' and 'magnetic coil'). A tokamak is a doughnut-shaped (i.e. toroidal) device with a strong magnetic field in the toroidal direction (Fig. 1.1). A gas is injected into the vessel and ionized, after which a toroidal current is induced in the plasma. The plasma current then induces a poloidal magnetic field that provides an inward pinch force on the particles that are now closely bound to the magnetic field lines, and thus the plasma may detach itself (partly) from the wall. The main advantage of this concept is that it is a closed system so that there are no end-losses such as in a linear device.

Advantages of tokamak fusion energy generation

Given the enormous energy yield from a small amount of fuel the natural fuel resources can be considered to be essentially limitless: the oceans contain enough D to supply energy for millenia to come, and it can be won cheaply. The first generation fusion reactors will also need tritium, T, which can be bred from Lithium, Li, that must be mined. The exhaust of a fusion reactor will consist mainly of He, a harmless inert gas; no CO_2 or any other climate-affecting gases will be produced. A fusion reactor is inherently safe: a 'meltdown' or runaway reaction is not possible as there is always only a very limited amount of fuel present in the device: e.g. the

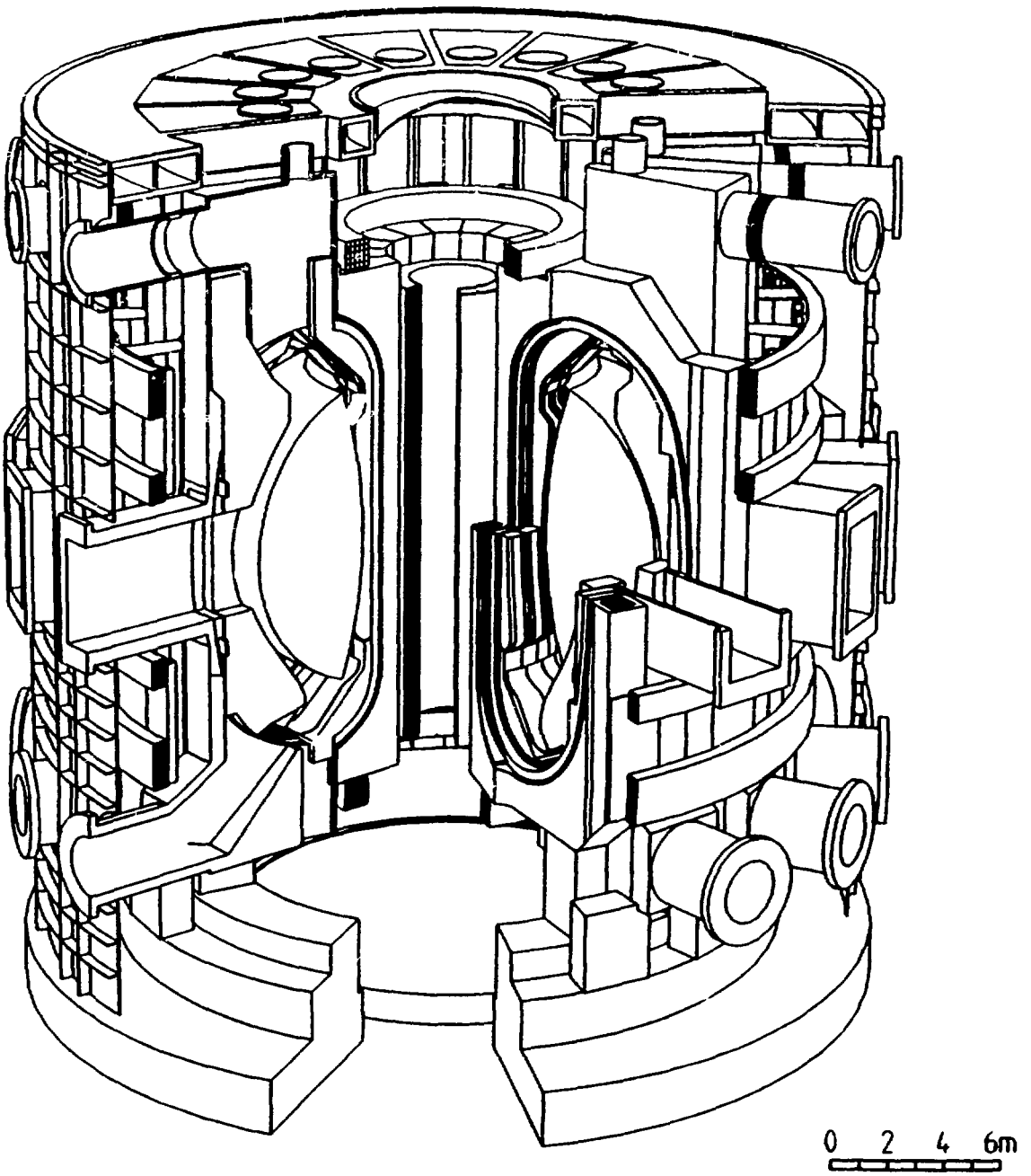

Fig. 1.1 Design of the ITER tokamak. The toroidal vacuum vessel in which the plasma is held can be seen, as well as several external coils that generate the magnetic field that confines and shapes the plasma.

energy content of the plasma of a JET-size device is at any time during operations less than that of 10 liter of boiling water. Finally, a serious technical failure will always result in a termination of the burn.

Disadvantages of tokamak fusion energy generation

A major disadvantage of the tokamak concept is that power stations based on this idea will be very costly and large, and that they can only be used where large electricity distribution grids are available. Also, such power stations require a high level of technology, comparable to space travel, which does not favour developing countries. Some people fear that concentrated power generation increases the political vulnerability of a country to terrorism. However, some of these disadvantages also apply to other forms of concentrated electricity generation such as hydroelectric power.

Another disadvantage is that, while the exhaust is reasonably safe, parts of the power stations become highly radioactive. Materials research aiming at finding materials able to withstand an intense neutron flux for a prolonged period of time is advancing. Yet it is estimated that the average lifetime of components in a power station is about 10 years, implying that substantial amounts of highly radioactive waste are produced in this way. This problem reduces the advantage of having low-level radioactive exhaust, even though this waste may have a relatively short half-life depending on the choice of materials.

Problems in achieving the fusion goal

Apart from the political problem of obtaining enough money to continue the research, there are several unresolved scientific and technical problems, of which some of the main ones are: (a) achieving the conditions (temperatures, densities) as required for successful power station operation. There has been a steady progress in this field and there is little doubt that this goal can be reached; (b) suppressing those instabilities that terminate operation and damage the device. Major progress has already been made in this field and it will probably be possible to suppress or avoid all major instabilities successfully; (c) removing exhaust (He) from an operating reactor. Under certain circumstances, helium tends to amass near the centre of the reactor, thus choking the process. Several operating schemes have been suggested to deal with this problem, amongst which the scheme with controlled central instabilities is perhaps most promising because the plasma constituents are remixed regularly.

1.4 This thesis

In a tokamak, the plasma is confined by means of a magnetic field. There exist an equilibrium between outward forces due to the pressure gradient in the plasma and inward forces due to the interaction between currents flowing inside the plasma and the magnetic field. The equilibrium magnetic field is characterized by helical field lines that lie on nested toroidal surfaces of constant flux. The equilibrium yields values for global and local plasma parameters (e.g. plasma position, total current, local pressure). Thus, precise knowledge of the equilibrium is essential for plasma control, for the understanding of many phenomena occurring in the plasma (in particular departures from the ideal equilibrium involving current filamentation on the flux surfaces that lead to the formation of islands, i.e. nested helical flux surfaces, Fig. 1.2), and for the interpretation of many different types of measurements (e.g. the translation of line integrated electron density measurements made by laser beams probing the plasma into a local electron density on a flux surface).

The problem of determining the equilibrium magnetic field from external magnetic field measurements has been studied extensively in literature. The problem is 'ill-posed' which means that the solution is unstable to small changes in the measurement data, and the solution has to be constrained in order to stabilize it. Various techniques for handling this problem have been suggested in literature. Usually ad-hoc restrictions are imposed on the equilibrium solution in order to stabilize it. Most equilibrium solvers are not able to handle very dissimilar measurement data which means that information on the equilibrium is lost. They generally do not allow a straightforward error estimate of the obtained result to be made, and they require large amounts of computing time. These problems are addressed in this thesis.

The investigations presented here can be divided into three parts: (1) determining the magnetic field outside the plasma and determining the plasma boundary and some characteristic plasma parameters; (2) determining the full equilibrium inside the plasma; and (3) studying departures from the equilibrium known as MHD modes.

The first part is addressed using moment methods. Moment methods allow a systematic treatment of the ill-posedness of the problem without introducing arbitrary restrictions of the equilibrium solution. Exact relations between known sets of moments are found. The methodology is successfully applied to the RTP tokamak, and the external magnetic field, the plasma boundary and moments of the current distribution inside the plasma are determined from magnetic field measurements.

The second part, determining the full plasma equilibrium, is addressed by means of the method of Function Parametrization (FP). FP is a technique to obtain the inverse of complex mappings. Pioneering work on this method has been done by B.J. Braams. In this thesis, the existing theory of FP is elaborated further and in detail. Advantages of FP are that it is quite generally applicable; it can deal with large numbers of diverse measurement data to obtain a consistent result; it provides error estimates of the obtained result, and differentiates between systematic and random errors; and it is fast so that it can be used in on-line data analysis. It is applied to the inversion of an existing forward computer mapping of plasma parameters onto measurements, the HBT equilibrium code that was developed at Rijnhuizen by H. Goedbloed. This inverse mapping is used to obtain the plasma equilibrium from magnetic data at RTP and from polarimetry / interferometry data at TEXTOR.

Thirdly, the departure from the ideal equilibrium with nested toroidal flux surfaces caused by helical MHD modes is studied. These instabilities arise because under certain circumstances field lines for which the ratio of the number of toroidal turns to the number of poloidal turns is rational can be easily displaced. Due to finite resistivity the field lines reconnect so that the topology of nested toroidal flux surfaces is changed and nested helical flux surfaces appear (Fig. 1.2). These 'islands' affect radial heat transport profoundly, causing increased heat loss from the plasma such that they are an obstacle in obtaining the high central temperatures needed for fusion. Knowledge of the precise nature of these modes is essential in improving the performance of tokamaks. The study of MHD modes presented in this thesis leads both to a better understanding of the modes and their topology and to a re-evaluation of the underlying equilibrium. Observation of MHD modes at JET during Pellet Enhanced Performance (PEP) discharges leads to the discovery of a central region of negative shear with improved confinement.

Chapter 2 serves as a general introduction to the subject matter of this thesis. The basic MHD theory is treated and the plasma equilibrium equations are derived in a slightly unconventional way. Also, the matter of turbulence and mode activity is addressed briefly. The remainder of the work can be divided into three parts as outlined above, each of which is presented in a separate chapter. Firstly, moment expansions are investigated in chapter 3. In this chapter, the relationship between two sets of moments is established and they are applied to the determination of the magnetic field and characteristics of the current distribution from magnetic measurements at the Rijnhuizen Tokamak RTP. In chapter 4 more complete information about the plasma equilibrium is obtained by means of Function Parametrization (FP). The theory of FP is treated in detail. FP is applied to the determination of the plasma

equilibrium at RTP and at the TEXTOR tokamak. Finally, magnetohydrodynamic (MHD) mode activity is studied in chapter 5. Mode activity at RTP and at JET in PEP discharges is investigated with a range of diagnostics. The measurement of the position of some modes leads to a better determination of the safety factor (q) profile, which, in the case of the PEP discharges, is found to be non-monotonic, with important consequences for local transport. The appendix provides a list of symbols and their definitions.

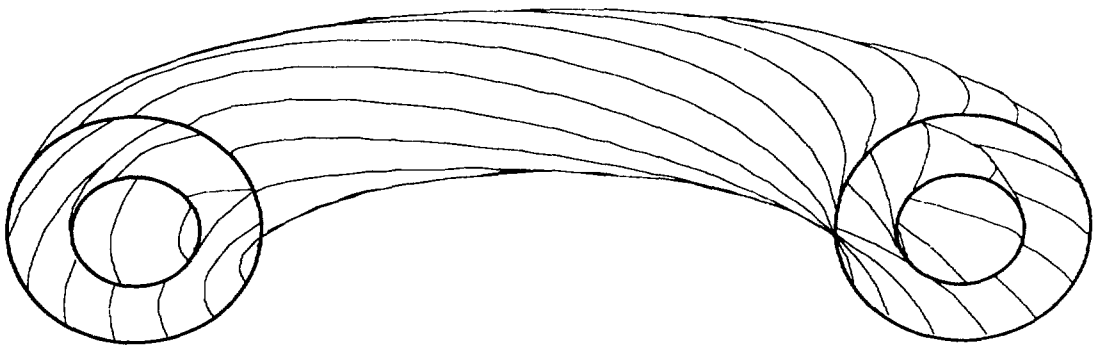

Fig. 1.2a Schematic representation of an ideal MHD equilibrium with nested toroidal flux surfaces in which helical magnetic field lines are embedded.

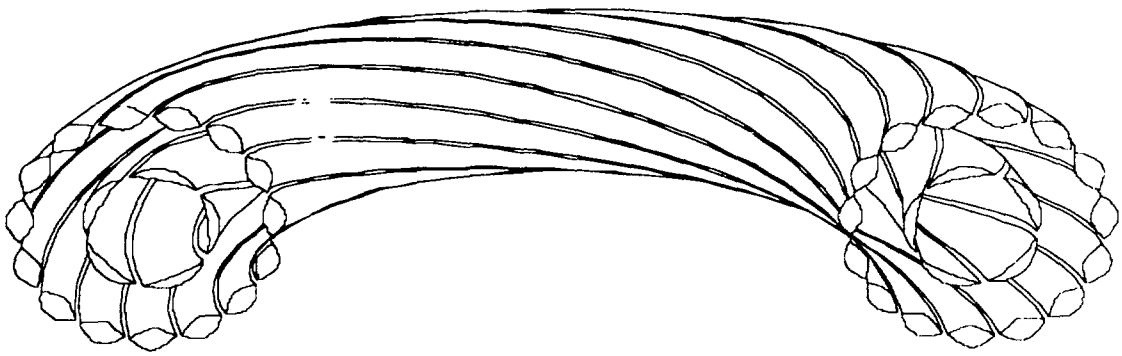

Fig. 1.2b The topology is altered by the appearance of islands, sets of nested helical flux surfaces.

1.5 Publications produced in the course of this work

Below a complete list of the publications that were produced in the course of the work described in this thesis is given. The publications that are listed under *Journals* are reproduced in this thesis (sections 3.2, 4.3, 4.2 and 5.5 respectively). Material from the conference contribution *Expansion of the flux and current density in toroidal systems and applications in fusion research,* Venezia (1989) I-459 is used in section 3.3.1.

Journals

B.Ph. VAN MILLIGEN, *Exact relations between multipole moments of the flux and moments of the toroidal current density in tokamaks,* Nucl. Fusion **30** (1990) 157 (also IR 89/06)

B.Ph. VAN MILLIGEN, H. SOLTWISCH, N.J. LOPES CARDOZO, *Application of Function Parametrization to the analysis of polarimetry and interferometry data at TEXTOR,* Nucl. Fusion **31** (1991) 309

B.Ph. VAN MILLIGEN, N.J. LOPES CARDOZO, *Function Parametrization: a fast inverse mapping method,* Accepted for publication in Comp. Phys. Comm. 1991

M. HUGON, B.Ph. VAN MILLIGEN, P. SMEULDERS, L. APPEL, D. BARTLETT, D. BOUCHER, A. EDWARDS, L. ERIKSSON, C. GOWERS, T.C. HENDER, G. HUYSMANS, J. JACQUINOT, P. KUPSCHUS, L. PORTE, P.H. REBUT, D. START, F. TIBONE, B.J.D. TUBBING, M. WATKINS, W. ZWINGMANN, *Shear reversal and MHD activity during Pellet Enhanced Performance plasmas in JET,* Submitted to Nucl. Fusion 1991

Conferences

B.Ph. VAN MILLIGEN, N.J. LOPES CARDOZO, *Tokamak evenwicht bepaling d.m.v. functieparameterisering,* Inventarisatie-conferentie over de plasma- en gasontladingsfysica in Nederland, Lunteren, 21 en 22 maart '88

B. Ph. VAN MILLIGEN, N.J. LOPES CARDOZO, *Tokamak equilibrium determination through function parametrization,* in Contr. Fusion and Plasma Phys. (Proc. 15th Eur. Conf. Dubrovnik, 1988), Vol. 12B, Part I, European Physical Society (1988) I-318

B.Ph. VAN MILLIGEN, *Expansion of the flux and current density in toroidal systems and applications in fusion research,* in Contr. Fusion and Plasma Phys. (Proc. 16th Eur. Conf. Venezia, 1989), Vol. 13B, Part I, European Physical Society (1989) I-459

B.Ph. VAN MILLIGEN, N.J. LOPES CARDOZO, *Bepaling van de magnetische veldconfiguratie in de Rijnhuizen Tokamak RTP,* Tweedaags symposium plasma- en gasontladingsfysica, Lunteren, 2 en 3 april 1990

B.Ph. VAN MILLIGEN, H. SOLTWISCH, N.J. LOPES CARDOZO, *Application of Function Parametrization to the analysis of polarimetry and interferometry data at TEXTOR*, in Contr. Fusion and Plasma Phys. (Proc. 17th Eur. Conf. Amsterdam, 1990), Vol. 14B, Part IV, European Physical Society (1990) IV-1660

R. POLMAN, R. VAN ANDEL, R. BOSMAN, R. DAMSTRA, D.F. DA CRUZ JR., B. DE GROOT, C.A.J. HUGENHOLTZ, J.J. KONING, W. KOOIJMAN, O.G. KRUYT, J. LOK, B.Ph. VAN MILLIGEN, A.A.M. OOMENS, F.C. SCHÜLLER, F.M.A. SMITS, P.H.M. SMEETS, J. STAKENBORG, A.J.H. TIELEMANS, C.J. TITO, A.G.A. VERHOEVEN, E. WESTERHOF, *ECRH sustained breakdown plasmas in RTP*, in Contr. Fusion and Plasma Phys. (Proc. 17th Eur. Conf. Amsterdam, 1990), Vol. 14B, Part III, European Physical Society (1990) III-1121

P. KUPSCHUS, B. BALET, D. BARTLETT, D. BOUCHER, C. CHALLIS, G. CORRIGAN, S. CORTI, A. EDWARDS, L.G. ERIKSSON, R. GILL, C. GORMEZANO, C. GOWERS, H. HOLM, M. HUGON, J. JACQUINOT, K. LAWSON, H. MORSI, G. NEILL, H. OOSTERBEEK, J. O'ROURKE, D. PASINI, L. PORTE, F. RIMINI, G. SADLER, G. SCHMIDT, G. SIPS, P. SMEULDERS, D. START, P.M. STUBBERFIELD, A. TARONI, F. TIBONE, B.J.D. TUBBING, M. VON HELLERMANN, B.Ph. VAN MILLIGEN, W. ZWINGMANN, *High thermonuclear yield on JET by combining enhanced plasma performance of ICRH-heated, pellet-peaked density profiles with H-mode confinement*, in Contr. Fusion and Plasma Phys. (Proc. 18th Eur. Conf. Berlin, 1991), Vol. 15C, Part I, European Physical Society (1991) I-1

M. HUGON, B. BALET, J.P. CHRISTIANSEN, A. EDWARDS, G. FISHPOOL, C.G. GIMBLETT, N. GOTTARDI, R.J. HASTIE, P. LOMAS, B.Ph. VAN MILLIGEN, G. NEILL, J. O'ROURKE, G. SIPS, P. SMEULDERS, P.M. STUBBERFIELD, T. TAGLE, S. WOLFE, *Current rise studies*, in Contr. Fusion and Plasma Phys. (Proc. 18th Eur. Conf. Berlin, 1991), Vol. 15C, Part I, European Physical Society (1991) I-41

P. SMEULDERS, D. BARTLETT, A. EDWARDS, G. FISHPOOL, T.C. HENDER, M. HUGON, B.Ph. VAN MILLIGEN, C. NARDONE, G. NEILL, L. PORTE, S. WOLFE, W. ZWINGMANN, *MHD studies in JET*, in Contr. Fusion and Plasma Phys. (Proc. 18th Eur. Conf. Berlin, 1991), Vol. 15C, Part II, European Physical Society (1991) II-53

F.C. SCHÜLLER, C.J. BARTH, A.J.H. DONNÉ, D. FERREIRA DA CRUZ, B. DE GROOT, P.C. VAN HAREN, S.H. HEIJNEN, G.M.D. HOGEWEIJ, C.A.J. HUGENHOLTZ, L.C. INGESSON, S.K. KIM, J.A. KONINGS, W. KOOIJMAN, A.C.A.P. VAN LAMMEREN, K.W. LEE, J. LOK, N.J. LOPES CARDOZO, A.C. MAAS, B.Ph. VAN MILLIGEN, A.A.M. OOMENS, R.W. POLMAN, B.C. SCHOKKER, F.M.A. SMITS, P.H.M. VAESSEN, A.G.A. VERHOEVEN, M. VERRECK, *Experimental observations of ohmic and ECR heated tokamak plasmas in RTP*, in Contr. Fusion and Plasma Phys. (Proc. 18th Eur. Conf. Berlin, 1991), Vol. 15C, Part I, European Physical Society (1991) I-121

2. MagnetoHydroDynamics

2.1 Introduction

The equation that describes the toroidally symmetric plasma as a single-species conducting fluid is the well known Grad-Shafranov equation. It is the basis for a large part of the methodology described in this thesis. Therefore its derivation from basic MagnetoHydroDynamic (MHD) equations is described step by step, explicitly displaying the most important assumptions, although in a somewhat unusual manner. The derivation is only ment as an introduction; more rigourous treatment can be found in many textbooks. Some equations derived as intermediate results are subject to less restraints or assumptions than the Grad-Shafranov equation and are therefore important in research that looks to the plasma in more detail than is permitted by the Grad-Shafranov equation, such as the study of the three-dimensional equilibrium or magnetic turbulence. Sections 2.6 and 2.7 deal briefly with the breakdown of the ideal MHD equilibrium due to turbulence and mode activity.

2.2 Coordinate systems

When studying tokamak devices such as described in Chapter 1, two obvious choices of coordinate systems facilitate the description. Here, both systems are used alternately. In addition, there is a less obvious choice of coordinate system (the so-called toroidal coordinates) that is of use in a particular moment formalism that is introduced in Chapter 3.

Firstly, the familiar left-handed cylindrical coordinate system (R,Z,ϕ) is introduced. The Z axis coincides with the major axis of the tokamak and the plane $Z = 0$ is the equatorial plane of the device.

Secondly, a left-handed coordinate system, the polar coordinate system (ρ,θ,ϕ), is introduced. It is in fact a simple plane polar coordinate system but with a third coordinate, ϕ, added. This coordinate system has a ring-shaped pole ($R = R_0$, $Z = 0$) that coincides with the minor axis of the tokamak (the 'minor axis' is a meaningful quantity with circular cross-section tokamaks only; in devices of other shape it is somewhat arbitrary). The relationship between the cylindrical coordinate system and the polar coordinates is:

$$R = R_0 + \rho \cos \theta \qquad (2.1a)$$

$$Z = \rho \sin \theta \qquad (2.1b)$$

The toroidal coordinate ϕ is identical to the cylindrical coordinate ϕ (Fig. 2.1).

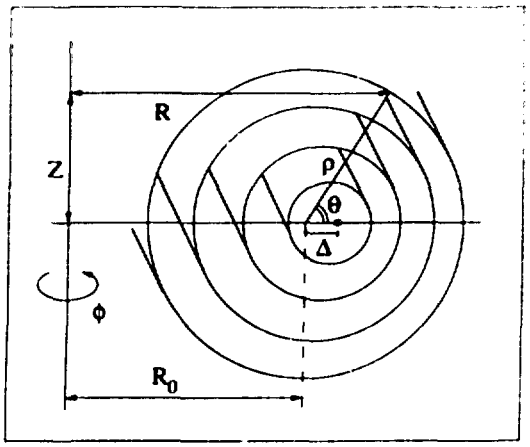

Fig. 2.1 A set of nested flux surfaces (not to scale). The magnetic axis is shifted outward by an amount Δ with respect to the plasma boundary. In this figure it is assumed for simplicity that the plasma boundary position R_{geo} is the same as the tokamak minor axis R_0, which is not generally true (see Appendix). The relationship between the cylindrical coordinate system (R,Z,φ) and the polar coordinate system (ρ,θ,φ) can also be seen. The polar coordinate surfaces generally do not coincide with flux surfaces.

2.3 Representation of the magnetic field

2.3.1 The flux function

The magnetic field is divergence free, or equivalently:

$$\nabla \cdot \mathbf{B} = 0 \tag{2.2}$$

(Gauss' Law). One may therefore introduce a magnetic potential **A** and an arbitrary gauge field G and write

$$\mathbf{B} = \nabla \times (\mathbf{A} + \nabla G) \tag{2.3a}$$

satisfying Eq. (2.2) for all choices of **A** and G. **A** (or, equivalently, **B**) is expressed in flux coordinates (ρ', θ', φ'). These coordinates are only known after solution of the Grad-Shafranov equation.

$$\mathbf{A} = A_{\rho'} \nabla\rho' + A_{\theta'} \nabla\theta' + A_{\phi'} \nabla\phi'. \tag{2.3b}$$

By choosing the arbitrary gauge field G such that $\nabla G = - A_\alpha \nabla\alpha$ (where $\alpha = \rho', \theta'$ or ϕ'), one can transform away any one of the three components of **A** in Eq. (2.3b). In other words, the magnetic vector field can *always* represented by means of only two scalar fields due to the restriction imposed by Eq. (2.2). Choose $\nabla G = - A_{\rho'} \nabla\rho'$, then Eqs. (2.3a and b) can be simplified by absorbing G:

$$\mathbf{B} = \nabla \times \mathbf{A} \tag{2.4a}$$

$$\mathbf{A} = A_{\theta'} \nabla\theta' + A_{\phi'} \nabla\phi'. \tag{2.4b}$$

Combining Eqs. (2.4a) and (2.4b) one obtains

$$\mathbf{B} = \nabla A_{\theta'} \times \nabla\theta' + \nabla A_{\phi'} \times \nabla\phi'. \tag{2.5a}$$

The two components of the vector potential $A_{\theta'}$ and $A_{\phi'}$ are renamed as ψ_t, the toroidal flux, and $-\psi_p$, the poloidal flux:

$$\mathbf{B} = \nabla\psi_t \times \nabla\theta' - \nabla\psi_p \times \nabla\phi', \tag{2.5b}$$

Eq. (2.5) allows a fully three-dimensional description of the magnetic field.

2.3.2 Toroidal symmetry

Of more immediate interest is the introduction of toroidal symmetry. Because tokamak devices are (to first order) symmetric with respect to rotation about the principal axis, one would expect the magnetic field structure to reflect this symmetry (to first order). This implies that neither ψ_t nor ψ_p depend on the coordinate ϕ and $\nabla\phi' = \nabla\phi$. Therefore $\nabla\psi_t$ has only components in the ρ- and θ-directions, so:

$$\nabla\psi_t \times \nabla\theta' = B_\phi \, \mathbf{e}_\phi, \tag{2.6}$$

where $B_\phi(\rho,\theta)$ is the toroidal magnetic field. Thus Eq. (2.5b) becomes

$$\mathbf{B} = B_\phi \, \mathbf{e}_\phi - \frac{1}{R} \nabla\psi_p \times \mathbf{e}_\phi, \tag{2.7}$$

where $\psi_p = \psi_p(\rho,\theta)$. Eq. (2.7) is the familiar tokamak physics representation of the magnetic field. In the following the subscript p is omitted unless confusion might otherwise arise.

2.4 The plasma model

2.4.1 The macroscopic description

The magnetic field equation (2.7) does not yet contain any plasma physics. One wishes to describe the plasma as a fluid using the macroscopic quantities v (velocity), p (pressure) and ρ (density) as state-identifying parameters. These quantities can be derived as velocity moments of a set of distribution functions $f_i(\mathbf{x},\mathbf{v},t)$ for each particle species i (having mass m_i), where **x** is the position vector and t the time [Bitt-86, Frei-87]:

$$n_i = \int f_i \, d^3\mathbf{v}, \qquad \mathbf{v}_i = \frac{1}{n_i}\int \mathbf{v} f_i \, d^3\mathbf{v}, \qquad T_i = \frac{1}{2}\frac{m_i}{n_i}\int (\mathbf{v}-\mathbf{v}_i)^2 f_i \, d^3\mathbf{v}$$

$$\rho = \sum_i m_i n_i \qquad \mathbf{v} = \frac{1}{\rho}\sum_i m_i n_i \mathbf{v}_i \qquad p = \sum_i n_i T_i \qquad \text{(2.8a - f)}$$

Thus, the macroscopic description (v, p, ρ) is based on a microscopic description f_i. A detailed analysis would require conservation equations (mass continuity equation, charge continuity equation, conservation of momentum and conservation of energy) for each species separately, as well as Maxwell's equations and Ohm's Law. It must be noted that due to anisotropy caused (mainly) by the strong magnetic field, the pressure is a tensor rather than a scalar quantity [Brag-65]. Viscosity, ν, appears in the equations through the effect of particle collisions, which are described in detail by collision operators. The situation becomes even more complex when it is realized that particle drifts are important. Neoclassical theory accounts for the latter [Hint-76].

As will be clear from the above, a thorough treatment of a magnetized plasma can easily become very cumbersome. In order to gain some insight into the global behaviour of the plasma, one would rather use a simplified model that is more easy to handle. Effects that are neglected by the simplification can then be added later. Such a gradual approach to a detailed model leads to greater insight into the plasma properties. Even if one would not agree to this, the available measurements do not allow a detailed determination of the velocity distribution functions and computers cannot handle the full equations in simulations, and therefore the details of the full model cannot be tested by experiment (as yet). Therefore, approximate models (suffering the same degree of crudeness as the available measurements) are more appropriate.

2.4.2 The one-fluid description

The following paragraphs discuss the 1-fluid MHD equations. This set of equations assumes that the motions of the various particle species can be summarized by a single vector field **v** as in Eq. (2.8). Further, the equations do not contain the effects of heat conduction, they assume

the pressure to be isotropic and they ignore the gravitational potential (which, however, can easily be included in the ∇p term). Finally, they assume that viscosity effects can be summarized by a $\nu\rho\nabla^2\mathbf{v}$ term. This is a very crude simplification of the tensorial form of the viscosity term $\nabla\cdot\Pi$ [Brag-65], which involves both **B** and **v** in order to account for pressure anisotropy, but since it will only be used in order of magnitude estimates it is sufficiently detailed.

The 1-fluid equations are:

$$\frac{\partial \mathbf{B}}{\partial t} = -\nabla \times \mathbf{E} \tag{2.9a}$$

$$\mathbf{j} = \nabla \times (\mathbf{B}/\mu) \tag{2.9b}$$

$$\nabla\cdot\mathbf{B} = 0 \tag{2.9c}$$

$$\nabla\cdot(\varepsilon\mathbf{E}) = \sigma \tag{2.9d}$$

$$\mathbf{E} + \mathbf{v} \times \mathbf{B} = \eta\mathbf{j} \tag{2.9e}$$

$$\frac{\partial \rho}{\partial t} + \nabla\cdot(\rho\mathbf{v}) = 0 \tag{2.9f}$$

$$\rho\frac{\partial \mathbf{v}}{\partial t} + \rho(\mathbf{v}\cdot\nabla)\mathbf{v} = -\nabla(p) + \mathbf{j} \times \mathbf{B} + \sigma\mathbf{E} + \nu\rho\nabla^2\mathbf{v} \tag{2.9g}$$

The equations (2.9a,b,c and d) are recognized as Maxwell's equations; Eq. (2.9e) is Ohm's Law; Eq. (2.9f) is the equation describing conservation of mass and Eq. (2.9g) is the equation of motion. There are 15 variables: **B**, **E** (the electric field), **j** (the current density), **v**, p, ρ (mass density) and σ (charge density) and 15 equations, so this set of equations is closed. Note that η (the resistivity) and ν (viscosity) are considered to be known parameters. Of course, like ν, η should really be treated as a tensor as well due to anisotropy. The magnetic permeability is assumed constant throughout the plasma: $\mu = \mu_0$, as is the permittivity: $\varepsilon = \varepsilon_0$.

In order to make estimates of the magnitude of the various terms, the positive scalars x^* are introduced, giving the typical magnitude of the various variables x in the plasma. By definition,

$$\mathbf{B} = B^*\hat{\mathbf{B}},\ \mathbf{E} = E^*\hat{\mathbf{E}},\ \mathbf{j} = j^*\hat{\mathbf{j}},\ \mathbf{v} = v^*\hat{\mathbf{v}},\ p = p^*\hat{p},\ \rho = \rho^*\hat{\rho},\ \sigma = \sigma^*\hat{\sigma} \tag{2.10a}$$

where the $\hat{x}$ are dimensionless scalars or vectors. Likewise, define

$$t = t^*\hat{t},\ \nabla = (L^*)^{-1}\hat{\nabla} \tag{2.10b}$$

This enables one to write the equations (2.9) in dimensionless form:

$$\alpha_1 \frac{\partial \hat{\mathbf{B}}}{\partial \hat{t}} = -\hat{\nabla} \times \hat{\mathbf{E}} \tag{2.11a}$$

$$\alpha_2 \hat{\mathbf{j}} = \hat{\nabla} \times \hat{\mathbf{B}} \tag{2.11b}$$

$$\hat{\nabla} \cdot \hat{\mathbf{B}} = 0 \tag{2.11c}$$

$$\alpha_3 \hat{\nabla} \cdot \hat{\mathbf{E}} = \hat{\sigma} \tag{2.11d}$$

$$\alpha_4 \hat{\mathbf{E}} + \alpha_1 \hat{\mathbf{v}} \times \hat{\mathbf{B}} = \alpha_\eta \alpha_1 \alpha_2 \hat{\mathbf{j}} \tag{2.11e}$$

$$\alpha_4 \frac{\partial \hat{\rho}}{\partial \hat{t}} + \hat{\nabla} \cdot (\hat{\rho} \hat{\mathbf{v}}) = 0 \tag{2.11f}$$

$$\alpha_\rho \alpha_4 \hat{\rho} \frac{\partial \hat{\mathbf{v}}}{\partial \hat{t}} + \alpha_\rho \hat{\rho} (\hat{\mathbf{v}} \cdot \hat{\nabla}) \hat{\mathbf{v}} = -\alpha_p \hat{\nabla} (\hat{p}) + \alpha_2 \hat{\mathbf{j}} \times \hat{\mathbf{B}} + \alpha_\sigma \hat{\sigma} \hat{\mathbf{E}} + \alpha_\nu \hat{\nabla}^2 \hat{\mathbf{v}} \tag{2.11g}$$

where

$$\alpha_1 = \frac{B^* L^*}{E^* t^*}, \quad \alpha_2 = \frac{\mu_0 j^* L^*}{B^*}, \quad \alpha_3 = \frac{\varepsilon_0 E^*}{\sigma^* L^*}, \quad \alpha_4 = \frac{L^*}{v^* t^*},$$

$$\alpha_\eta = \frac{\eta}{\mu_0 v^* L^*}, \quad \alpha_\rho = \frac{\mu_0 \rho^* v^{*2}}{B^{*2}}, \quad \alpha_p = \frac{\mu_0 p^*}{B^{*2}}, \quad \alpha_\sigma = \frac{\mu_0 \sigma^* E^* L^*}{B^{*2}}, \quad \alpha_\nu = \frac{\mu_0 \nu \rho^* v^*}{L^* B^{*2}}.$$

Note that $\alpha_\eta = 1/Re_m$, where Re_m is the magnetic Reynolds number; $\alpha_\rho = v^{*2}/v_A^2$, where v_A is the Alfvén velocity; $\alpha_p = \frac{1}{2}\beta$, where β is the local normalized pressure; and α_ν is related to the more commonly used fluid Reynolds number $Re = v^* L^*/\nu$ by the relation $\alpha_\nu = \alpha_\rho/Re$. There is no commonly used parameter equivalent to α_σ, because usually quasi-neutrality is assumed from the beginning (see section 2.4.3). Thus, the first result of this approach is that the important parameters β, Re, Re_m and others appear automatically when making the Eqs. (2.9) dimensionless.

In the Eqs. (2.11), which are equivalent to Eqs. (2.9), all variables are *dimensionless* and *of order unity* if the x^* are well-chosen (i.e. they are given realistic values). Strictly speaking, this can only be true in a limited region of the plasma: e.g. it is to be expected that some terms become vanishingly small or very large near the plasma boundary. Furthermore, the meaning of L^* and t^* is somewhat ambiguous, because typical length and time scales may

not be the same for all variables while typical length scales for one variable may not be the same in all directions (anisotropy).

The 9 α_i's represent *all* possible independent dimensionless combinations of the 9 parameters x* of Eq. (2.10), μ_0, ε_0, η and ν (13 parameters in all), because there are 4 independent physical dimensions involved (kg, m, s and C). The relative importance of the terms appearing in these equations can be estimated from the dimensionless factors α_i, provided the inner products and vector products do not make terms vanish. It is assumed that they vanish locally only. In that case the Eqs. (2.11a, b, d and f) demonstrate that $\alpha_i = O(1)$ (i=1,2,3,4). This is probably why simple dimensionality arguments so often prove to be successful in plasma physics. Thus, only three of the typical magnitudes B*, E*, j*, v*, σ*, L* and t* are independent.

The terms on the left-hand side of Eq. (2.11e) are both *O(1)*, which implies that the term on the right-hand side either cancels or is also *O(1)*. So clearly there are two distinct regimes: $\alpha_\eta << 1$ (the ideally conducting plasma) or $\alpha_\eta = O(1)$ (the resistive regime).

In the following, the conditions under which some terms can be neglected will be discussed and quantified. Initially it is assumed $\alpha_\eta = O(1)$, but the possibility of letting $\alpha_\eta \rightarrow 0$ is left open.

2.4.3 The assumption of quasi-neutrality

In the quasi-neutral model it is assumed that the deviation from space charge neutrality is negligible. This assumption is motivated by introducing the Debije shielding length λ_D that is a measure for the Coulomb interaction radius in a plasma consisting of two fluids of ions and electrons [Wess-87]:

$$\lambda_D = \sqrt{\frac{\varepsilon_0 T_e}{2 n_e e}},$$

where ε_0 is the vacuum permittivity, T_e the electron temperature in eV, n_e the electron density in m^{-3} and e the unit charge in C. Thus, for a plasma of T_e = 10 keV and $n_e = 10^{19}$ m^{-3}, $\lambda_D = 10^{-4}$ m. In tokamak plasmas the plasma dimensions are much larger than λ_D (by 4 orders of magnitude) and so the assumption of quasi-neutrality is reasonable. Under charge neutrality, the inequality

$$\boxed{\alpha_\sigma << 1} \qquad (2.12)$$

holds. Using $\alpha_i = O(1)$ (i=1,2,3,4) it follows that

$$\sigma^* << B^*/\eta \qquad E^* << cB^*, \qquad v^* << c, \qquad t^* >> L^*/c, \qquad L^* >> \frac{\eta}{\mu_0 c}$$

where c is the light speed. None of these restrictions is strong, confirming the weakness of the assumption. In particular, the restriction on σ^* becomes very weak for small η. The consequence of this assumption is that the α_σ term in Eq. (2.11g) may be dropped.

2.4.4 The assumption of quasi-static flow

A second assumption that is often made is the assumption of quasi-static flow, which means that the co-moving time derivative can be ignored in Eq. (2.11g), i.e. the first two terms are negligible. This is achieved when

$$\boxed{\alpha_\rho << 1} \tag{2.13}$$

The implications of this assumption are easily found to be, again using $\alpha_i = O(1)$ (i=1,2,3,4):

$$E^* << v_A B^*, \quad v^* << v_A, \qquad t^* >> L^*/v_A, \qquad L^* >> \frac{\eta}{\mu_0 v_A}$$

where v_A is the Alfvén velocity, $v_A = \dfrac{B^*}{\sqrt{\mu_0 \rho^*}}$

This defines the validity regime for the approximation (2.13). The constraints are a little stronger than with (2.12). Again, the restraint on L* vanishes as $\eta \to 0$, but the others remain. If one takes B* = 1 T, $\eta = 10^{-9}$ Ωm and $\rho^* = 10^{-8}$ kg m^{-3} as typical values for a tokamak plasma, $v_A = 10^7$ m/s, so that these conditions are easily met for most phenomena of interest.

This description, however, ignores an important effect: the gyration of electrons and ions around the magnetic field lines. The thermal velocity of 10 keV electrons is $6 \cdot 10^7$ m/s, violating the assumption. So the gyromotion is not described under this assumption, and the description refers to guiding centre (i.e. the average position of a particle during one gyration) motion only, and timescales longer than the inverse of the gyration frequency. In a plasma of 10 keV temperature and 1 T magnetic field, the gyration or Larmor radii of electrons (λ_e) and ions ($\lambda_i = \sqrt{m_i/m_e}\,\lambda_e$ if $T_i = T_e$) are $\lambda_e = 3 \cdot 10^{-4}$ m and $\lambda_i = 10^{-2}$ m, approximately. Thus, the smallest length scale that can be described is larger than λ_i.

2.4.5 The assumption of low collisionality

A third assumption is the assumption of low collisionality, which should be motivated from a study of the collision operator under given conditions. The assumption holds when

$$\boxed{\alpha_\nu << 1} \tag{2.14}$$

The implications of this assumption are found to be:

$$E^* << v_A B^* s_{\eta\nu}, \qquad v^* << v_A s_{\eta\nu}, \qquad t^* >> v_A L^*/s_{\eta\nu}, \qquad L^* >> \frac{\eta}{\mu_0 v_A}/s_{\eta\nu}$$

Thus, the severity of this assumption depends on the dimensionless ratio $s_{\eta\nu} = \eta/(\mu_0\nu) = Re/Re_m$. For the typical tokamak it can be shown that $s_{\eta\nu} << 1$ [Bate-80], so this assumption is a lot stronger than (2.13). Taking some typical values as before, one finds $s_{\eta\nu} = 10^{-13}$, yielding $L^* >> 10^3$ m. Now the electron mean free path can be estimated at 10^4 m, barely satisfying this requirement. But obviously other length scales cannot meet this demand, and it is clear that a realistic model should take account of the viscosity or collision term.

Summarizing the previous sections, it is found that 5 dimensionless parameters can be used to distinguish plasma regimes in the one-fluid MHD description (note that the matter of low- and high-beta regimes was not discussed). An effort was made to show explicitly what the assumptions that are made in the derivation of the Ideal MHD Model mean in terms of restrictions on typical parameters in order of increasing severity. Obviously, the estimates thus obtained are quite crude because no account is taken of effects such as anisotropy.

2.4.6 The ideal MHD model

The ideal MHD model is derived from Eqs. (2.9) under the assumptions of quasi-neutrality and quasi-static flow, i.e. Eqs. (2.12) and (2.13) and $\alpha_p << \alpha_p$ (negligible centrifugal forces). In the limits $\eta \to 0$ (negligible resistivity) and $\nu \to 0$ (collisionless regime, Eq. (2.14)) this set of assumptions yields the common ideal MHD equations. In this limit the equations form a consistent and closed set. The set of ideal MHD equations is

$$\nabla p = \mathbf{j} \times \mathbf{B} \tag{2.15a}$$

$$\mu_0 \mathbf{j} = \nabla \times \mathbf{B} \tag{2.15b}$$

$$\nabla \cdot \mathbf{B} = 0 \tag{2.15c}$$

In order to impose toroidal symmetry, rewrite Eq. (2.7) as

$$\mathbf{B} = RB_\phi \nabla\phi - \frac{1}{R}\nabla\psi \times \mathbf{e}_\phi, \tag{2.16}$$

and insert it in Eq. (2.15b):

$$\mu_0 \mathbf{j} = \nabla(RB_\phi) \times \nabla\phi - \mathbf{e}_\phi \frac{1}{R}\Delta^*\psi, \tag{2.17a}$$

where

$$\Delta^* = R\frac{\partial}{\partial R}\frac{1}{R}\frac{\partial}{\partial R} + \frac{\partial^2}{\partial Z^2}. \tag{2.17b}$$

Two important observations can be made at this stage: from $\mathbf{B}\cdot\nabla p = \mathbf{B}\cdot(\mathbf{j}\times\mathbf{B}) = 0$ it follows that the pressure is constant on a magnetic surface (assuming, of course, that there *are* magnetic surfaces; a magnetic surface is a two-dimensional subspace to which a particular field line is tangent everywhere). In the toroidally symmetric case under study here magnetic surfaces can be identified with the surfaces ψ = const. Thus the observation above implies $p = p(\psi)$.

Combining (2.15a) and (2.17a) one finds

$$\mu_0 \frac{\partial p}{\partial \psi}\nabla\psi = -\frac{1}{R^2}\Delta^*\psi\,\nabla\psi - \frac{B_\phi}{R}\nabla(RB_\phi) \tag{2.18}$$

implying that $\nabla(RB_\phi) = \alpha\nabla\psi$, or $F = RB_\phi$ is a surface quantity $F = F(\psi)$. From Eq. (2.17a) it is clear that F is proportional to the poloidal current flowing on the flux surface. It must be stressed that $p = p(\psi)$ and $F = F(\psi)$ are local relations that may not hold everywhere, e.g. on surfaces with topologically disjunct parts such as occur with separatrices.

The familiar Grad-Shafranov equation [Grad-58, Shaf-58] now follows from Eq. (2.18):

$$\Delta^*\psi = -\mu_0 R^2 p' - FF' \tag{2.19}$$

where ' denotes $\partial/\partial\psi$. The Grad-Shafranov equation is an elliptic differential equation with two source functions, p and F.

2.5 Solving the ideal MHD equations

2.5.1 General considerations

The MHD equilibrium problem is to solve Eq. (2.19) with externally imposed boundary conditions (i.e. measurements). Internal conditions such as continuity of $\mathbf{B}\cdot\mathbf{n}$ and of $\mathbf{H}\times\mathbf{n}$ (if surface currents are absent) on all internal surfaces where $\mathbf{n}$ is the normal on the surface must be satisfied in the solution region. Additional constraint equations are necessary to fix a unique solution (geometrical constraints such as limiters must be taken into account, but, more importantly, a restriction upon the class of profiles $p(\psi)$ and $F(\psi)$ must be imposed).

Much has been written on the subject [Shaf-58, Mukh-71, Zakh-73, Goed-84, Lao-85, Frei-87, Blum-90] and this will not be reviewed here. However, it is attempted to shed some light on the problem in general terms.

The MHD equilibrium problem is an inverse problem for Eq. (2.19): the solution should provide a mapping of the discrete set of measurements represented by the vector $\mathbf{q}$, which can be expressed as functionals of the toroidal current density (or the two source functions p and F), to the flux function ψ and characteristic parameters of the equilibrium, or equivalently the current density.

Consider the simplified problem of finding a plasma equilibrium with fixed boundary and total current. The free-boundary problem is not principally different but it would complicate the discussion needlessly. Then, the problem can be visualized as finding the inverse mapping of a projection; namely the projection of the current density in terms of an infinite class of functions J in a Hilbert space R (defined on the interval $0 < \psi < 1$, where ψ is a normalized flux label that is 0 on the magnetic axis and 1 at the plasma-vacuum interface; see Fig. 2.1 for a typical flux surface geometry) onto the finite set of measurements. Obviously, the inverse mapping can only yield the projection of J onto a finite-dimensional subspace S of R whose dimension is dictated by the number and accuracy of the measurements. The 'true' current density also contains a component orthogonal to the subspace S that maps to zero (or rather to components of the measurement vector $\mathbf{q}$ small compared to the measurement error $\varepsilon(\mathbf{q})$) in the measurement space, and which cannot be determined from the measurements.

It is clear, therefore, that one must restrict the solution *a priori* to a certain subspace S in order to obtain a well-posed problem; if such a restriction is not made, the solution will be unstable to small variations in the measurements. This may seem unsatisfying because it means in practice that the solution of the equilibrium problem is dictated beforehand except for a few

free parameters. Consider, however, the formulation of the determination of such free parameters, which is expressed as a least squares problem minimizing R [cf. Luxo-82, Brus-84, Fene-84, Blum-90] where

$$R = \sum_{i=1}^{N_q} w_i \, (q_i - q_i')^2$$

where N_q is the number of measurements, $\mathbf{q}$ is an actual set of measurements, $\mathbf{q}'$ is a simulated set of measurements and w_i are weights. It is obvious that R will reach its deepest minimum for that choice of subspace *S* that contains *at least* the total set of functions that does not map to zero (or insignificance) on the space of measurements. Therefore, if more measurements are added to an existing set, it may be necessary to extend the representation of the current density to a larger class of functions. Nevertheless some arbitrariness in the representation of the current density will always be present (namely part of it may lie in the subspace orthogonal to *S*). It is interesting to note that the equilibrium problem bears some similarity to the problem of finding a distribution (of e.g. current) from a set of (current) moments.

2.5.2 A conventional equilibrium solver method

The principal method of equilibrium determination is straightforward in principle, even though it is complex in practice. Below, a global description of the typical procedure is given. More comprehensive reviews are found in Refs. [Lack-76, Blum-90].

In general, the plasma state is represented by a finite set of parameters. The MHD model provides a mapping of these parameters onto the measurements. The choice of parametric representation of the plasma state is somewhat arbitrary, but it is attempted to give a systematic treatment of this subject here, as it will return in Chapter 4.

Some functional representation is chosen for the source functions $p(\psi)$ and $F(\psi)$ in Eq. (2.19):

$$p(\psi) = p(0)f(\mathbf{a},\psi), \qquad F(\psi) = F(0)g(\mathbf{b},\psi),$$

where $\mathbf{a}$ and $\mathbf{b}$ are the free parameters that are to be determined from the measurements, and f and g are functionals giving the shape of p and F only. Generally, the functionals used are sums of polynomials, preferably though not necessarily built from elements of a complete set. In theory, $\mathbf{a}$ and $\mathbf{b}$ are infinite-dimensional vectors, but they are truncated at a suitable point. There must be two additional parameters to give the amplitudes of both functions (i.e. p(0) and F(0)). These are generally given implicitly by means of the parameters I_p (the total plasma

current) and β (the normalized plasma pressure). For some purposes it is more convenient to use δ (the Shafranov shift) instead of β, which is equivalent.

The plasma boundary geometry must also be specified by a set of parameters. The way in which this is done depends on the basic shape, which is dictated by the machine for which computations are made. The location of the geometric centre of the plasma boundary (R_{geo}, Z_{geo}) along with the average minor radius a_{min} (or equivalently the plasma volume) are the basic geometry parameters. An infinite set of parameters describing deviations from a basic shape (circular, D-shape or otherwise) is then e.g. given in terms of a Fourier expansion of this deviation in the poloidal angle. Such a set of boundary shape parameters is denoted by the vector **c**.

The free parameters $\mathbf{p} = \{\mathbf{a}, \mathbf{b}, \mathbf{c}, R_{geo}, Z_{geo}, a_{min}, I_p, \delta\}$ are given some initial values, and Eq. (2.19) is solved to find $\psi(R,Z)$. The cost function R introduced above is evaluated, the parameters **p** are adjusted and the computation is iterated until a suitable minimum of R has been found. Note that this procedure is restricted to the computation of equilibria with nested magnetic surfaces and a single magnetic axis.

2.6 Analogy with fluid dynamics

So far this chapter has only considered ideal MHD equilibrium. The plasma, however, is pervaded by waves and oscillations of many different types and by turbulence [Bate-80]. In this section the analogy between the MHD equations and fluid equations is explored, and it is shown why the study of fluid turbulence is relevant to the study of turbulence in plasmas.

2.6.1 Analogy between Ideal MHD and Fluid Dynamics

A perfect analogy exists between non-resistive ideal MHD theory and fluid dynamics. Compare the vorticity equations for an ideal incompressible fluid with the ideal MHD equations (2.15):

Ideal MHD		*Ideal fluid*	
$\nabla p = \mathbf{j} \times \mathbf{B}$	(2.20a)	$-\nabla(p/\rho + u^2/2) = \omega \times \mathbf{u}$	(2.21a)
$\mathbf{j} = \nabla \times (\mathbf{B}/\mu_0)$	(2.20b)	$\omega = \nabla \times \mathbf{u}$	(2.21b)
$\nabla \cdot \mathbf{B} = 0$	(2.20c)	$\nabla \cdot \mathbf{u} = 0$	(2.21c)

The formal identity of these two sets of equations is obvious: replacing ω (the vorticity) by $\mathbf{j}$, $\mathbf{u}$ by $\mathbf{B}/\mu_0$ and $-(p/\rho + u^2/2)$ by p/μ_0, Eqs. (2.21) transform into (2.20). Shafranov has successfully exploited this analogy to obtain some important results [Shaf-58].

2.6.2 Analogy between Resistive MHD and Viscous Fluid Dynamics

Often, however, one cannot neglect resistivity in the MHD description (as in the study of turbulence) and one is forced to use the full MHD equations. Unfortunately, the perfect analogy breaks down when additional terms such as resistivity and viscosity enter the equations.

To demonstrate this, the Maxwell Eqs. (2.9a,b) and Ohms Law (2.9e) are combined to yield Eq. (2.22) (where ρ is assumed to be uniform and quasi-static such that $\nabla \cdot \mathbf{v} = 0$):

Resistive MHD		*Viscous fluid*	
$\frac{D\mathbf{B}}{Dt} = (\mathbf{B}\cdot\nabla)\mathbf{v} + \frac{\eta}{\mu_0}\nabla^2\mathbf{B}$	(2.22)	$\frac{D\mathbf{u}}{Dt} = \mathbf{F} - \nabla\left(\frac{p}{\rho}\right) + \nu\nabla^2\mathbf{u}$	(2.23)

Here $\frac{D}{Dt}$ is the convective derivative $\frac{D}{Dt} = \frac{\partial}{\partial t} + (\mathbf{v}\cdot\nabla)$ (or the same with $\mathbf{u}$ instead of $\mathbf{v}$ in the fluid equation). Eq. (2.23) is the Navier-Stokes equation for an incompressible fluid with uniform density and viscosity, shown here for comparison [Batc-67]. $\mathbf{F}$ is an external force and ν the fluid viscosity.

Both models display nonlinearities which are quadratic (as a consequence of the convective derivatives and in Eq. (2.22) also the $(\mathbf{B}\cdot\nabla)\mathbf{v}$ term) and essentially convective in nature. Further, both models contain diffusive dissipation that acts primarily on small-scale turbulence (since the ∇^2 operator is large for small scale phenomena). From these considerations, one may expect turbulence to show globally similar behaviour in both models.

First it is assumed that the force appearing in Eq. (2.23) is conservative, i.e. it can be written $\mathbf{F} = \nabla\phi$. Then, by taking the rotation of Eq. (2.23) one obtains:

Resistive MHD *Viscous fluid*

$$\frac{\partial \mathbf{B}}{\partial t} = \nabla \times (\mathbf{v} \times \mathbf{B}) + \frac{\eta}{\mu_0}\nabla^2\mathbf{B} \quad (2.24) \qquad \frac{\partial \omega}{\partial t} = \nabla \times (\mathbf{u} \times \omega) + \nu\,\nabla^2\omega \quad (2.25)$$

Eq. (2.25) is know as the vorticity equation. The similarity of these equations is even more striking. Note that the equation of motion was not used in the derivation of Eq. (2.24) and therefore this relation is valid even in collisional plasmas. However, appealing though the similarity may be there is a fundamental difference in the sense that no relation similar to $\omega = \nabla \times \mathbf{u}$ (valid in fluid dynamics) exists in MHD between **B** and v. Thus, Eq. (2.24) describes an essentially more complex system than Eq. (2.25).

In order to restore the fluid-MHD analogy, a non-conservative force **F** is introduced in the Navier-Stokes equation (2.23). Thus

Resistive MHD *Viscous fluid*

$$\frac{\partial \mathbf{B}}{\partial t} = \nabla \times (\mathbf{v} \times \mathbf{B}) + \frac{\eta}{\mu_0}\nabla^2\mathbf{B} \quad (2.26) \qquad \frac{\partial \omega}{\partial t} = \nabla \times (\mathbf{u} \times \omega + \mathbf{F}) + \nu\,\nabla^2\omega \quad (2.27)$$

The external force **F** can be interpreted as being due to some external stirring of the fluid. The equations, although still not identical, are now of comparable complexity. Thus one has the interesting situation that the study of turbulence in externally stirred viscous fluids bears relevance to MHD turbulence, and it may be possible to devise fluid turbulence experiments that enhance our knowledge of MHD turbulence, provided that it is possible to obtain fluid Reynolds numbers $\mathrm{Re} = u^*L^*/\nu$ of the same order of magnitude as the magnetic Reynolds number $\mathrm{Re}_m = \mu_0 v^* L^*/\eta$.

The model described above can be simplified in a tokamak situation, where the magnetic field **B** has a dominant unvarying but inhomogeneous component $\mathbf{B}_0$; in fluid flow, this would correspond to a dominant vorticity Ω_0. Thus the analog of resistive turbulent flow in a section of tokamak plasma is externally imposed turbulence in a rotating viscous fluid.

2.7 MHD modes and stability

2.7.1 The safety factor

The magnetic tokamak equilibrium is characterized by nested toroidal flux surfaces. The helical magnetic fieldlines lie on flux surfaces. A useful quantity is the safety factor, $q(\psi)$, which is equal to the number of toroidal transits a magnetic fieldline makes for each poloidal transit. Therefore the safety factor is [Wess-87, Frei-87]:

$$q = \frac{1}{2\pi}\int \frac{1}{R}\frac{B_\phi}{B_\theta}\,ds = \frac{F(\psi)}{2\pi}\int \frac{1}{R^2 B_\theta}\,ds \qquad (2.28)$$

where the integration is carried out over a single poloidal circuit along the flux surface. Higher values of q provide greater stability against tearing modes.

2.7.2 Tearing modes

In general, the safety factor in tokamaks is a roughly parabolic function of the radius ρ, increasing towards the plasma boundary. Typically, it is approximately 1 in the centre and around 4 at the boundary. Thus, there are always flux surfaces where q is rational, i.e. $q = m/n$ (m and n integer). A rational value of q means that after m toroidal and n poloidal turns a magnetic fieldline on the flux surface connects with itself. On rational (or resonant) surfaces, a small displacement of a fieldline is not smeared out over the whole flux surface, and can under certain circumstances be enhanced: this is called a magnetic instability. In general, smaller values of m and n imply stronger instability: e.g. (m,n) = (1,1) is associated with the violent sawtooth instability (see Fig. 2.2 for a plot of fieldlines with (m,n) = (1,1) symmetry).

Due to finite resistivity the displaced field lines can reconnect (tearing mode), changing the topology of the magnetic flux function, which now no longer consists of simple nested flux surfaces (Fig. 2.3) [Bate-80, Wess-78, Wess-87]. The magnetic islands that are thus created are helical structures with nested flux surfaces and a magnetic axis. Fig. 2.4 shows the result of a resistive field line computation (Poincaré map) [Bick-87], showing the island structure in a poloidal cross-section and the toroidal effect which results in a different island size on the inside and outside of the cross-section. The helical island structures rotate mainly in the toroidal direction because poloidal rotation requires energy to compress and expand them. These structures can sometimes cause a disruption, especially if they lock to external magnetic stray fields.

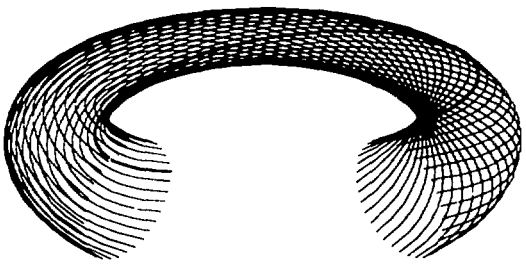

Fig. 2.2 Field lines on a q = 1 surface. One field line is highlighted for clarity.

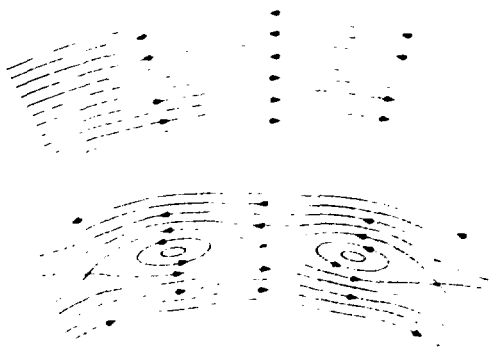

Fig. 2.3 Section of a few flux surfaces around a rational surface (dashed line). The field at the rational surface has been subtracted from the total field, and thus the field lines reverse direction from one side of the rational surface to the other. The upper figure shows the situation before reconnection, the lower after reconnection [Wess-87]. Note the change in topology: the lower figure shows several sets of nested flux surfaces (islands) within the pre-existing set of nested flux surfaces. This process may repeat itself to quite small scale (secondary and tertiary islands), thus creating a chaotic field structure.

The existence of islands is of importance for confinement and heat transport. The high mobility of particles along the field lines leads to homogeneous temperatures along the nested surfaces within the islands, such that the temperature profile is 'short-circuited' over the radial extent of the island. Further, the existence of a stochastic layer around the island separatrix is expected to increase radial transport through the 'X-points' of the islands. Finally, island chains on separate rational surfaces may overlap, creating a stochastic area between these surfaces with strong radial diffusion [Rebu-86b].

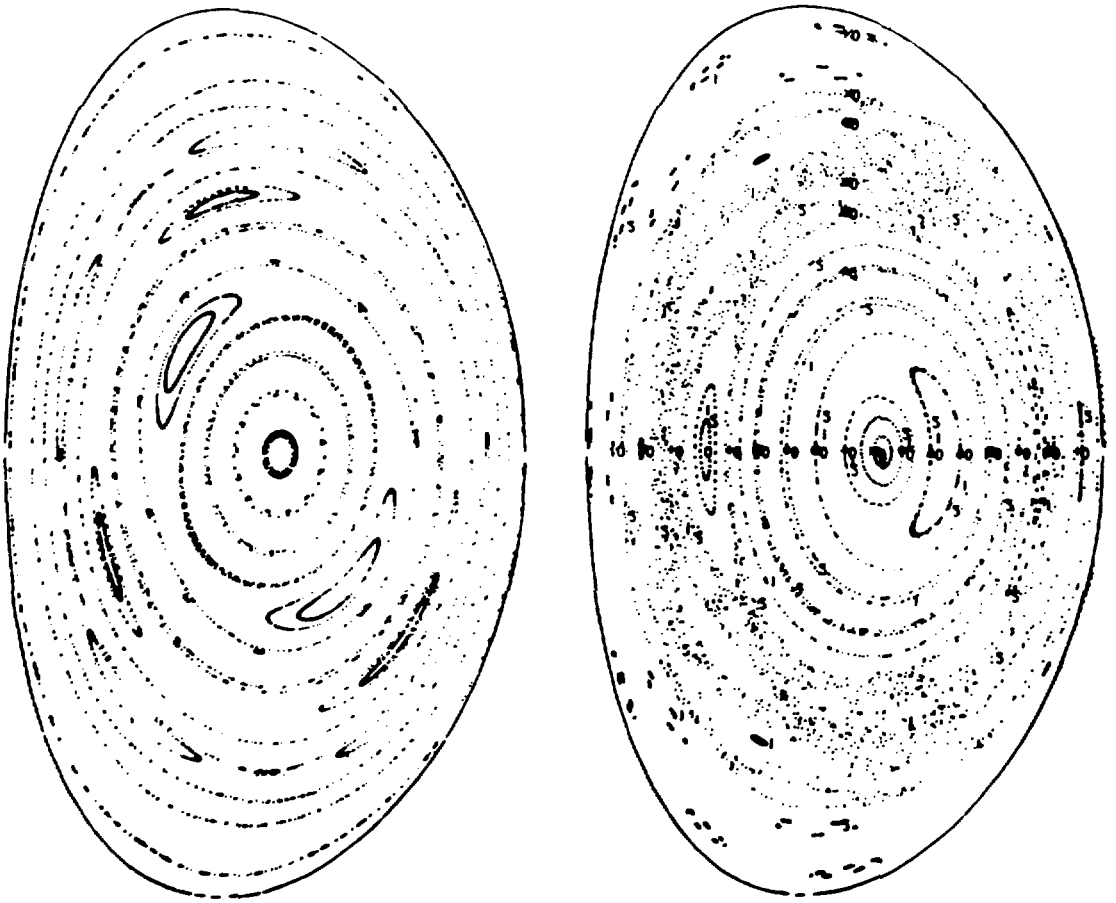

Fig. 2.4 Field line mapping or Poincaré plot of magnetic field lines in a poloidal cross-section [Bick-87]. Starting from an ideal equilibrium with nested flux surfaces, the field lines are perturbed and islands appear (left-hand figure). If the perturbation amplitude is increased, the islands grow and when the islands on neighbouring flux surfaces begin to overlap, ergodic or random patters emerge (right-hand figure).

3. Multipole and current moments

3.1 Introduction

The basic MHD equilibrium problem has been defined in the previous chapter: the determination of the magnetic equilibrium inside the plasma, using magnetic probes that are located outside the plasma. The problem can be divided into two parts: 1) solving the homogeneous Grad-Shafranov (GS) or Laplace equation in the vacuum region surrounding the plasma and determining the plasma boundary such that the solution matches the measurements, and 2) solving the complete GS equation in the plasma region, such that the solution matches the solution to 1) at the plasma boundary [Brus-84]. Already the first and easiest part of the problem is ill-posed in the sense that small variations in the boundary data may cause large changes in the solution some distance away. The reason for this is that poloidal variations of the plasma current that behave as $\cos(m\theta)$, where θ is the poloidal angle, give rise to magnetic fields that fall off as $\rho^{-(m+1)}$ towards the outside, where ρ is the radial coordinate. Thus details of the current distribution with high poloidal mode numbers m can be drowned in the signal generated by the lower m's. Conversely, high m details that are measured need to be extrapolated inwards if they are to be translated in a current distribution, and thus blow up strongly: clearly an unstable procedure and very sensitive to measuring errors. A systematic way of treating the ill-posedness is expanding the flux function in a set of harmonic functions, and taking only a finite number of terms into account: such an approach is called a moments method [Zakh-73, Woot-79, Lao-81, Lee-81, Lao-84, Hakk-87].

Section 3.2 is a reprint of the letter *Exact relations between multipole moments of the flux and moments of the toroidal current density in tokamaks* [Mill-90a]. In it, two sets of moments are introduced: current moments and multipole moments. Section 3.3 shows how the current moments can be used to reconstruct the current profile, and a suggestion for definitions of characteristic current distribution parameters is made. Section 3.4 discusses how the multipole moments are applied at RTP in order to reconstruct the vacuum field, and the accuracy of the determination of the multipole and current moments at RTP is studied. In section 3.5 the relative merits of the two sets of moments are discussed.

3.2 Exact relations between multipole moments of the flux and moments of the toroidal current density in tokamaks

B.Ph. VAN MILLIGEN

3.2.1 Abstract

In tokamak fusion research, expansions of the flux in solutions to the homogeneous Grad-Shafranov equation (multipole moments method) have been shown to provide a good description of the flux outside the plasma. In practice, moments of the toroidal current distribution are more often used, because they relate directly to meaningful global plasma parameters. The letter presents a method by which exact relationships between the multipole and the current moments can be obtained. Results for some important special cases are presented.

3.2.2 Introduction

An important topic in tokamak fusion research is the determination of the magnetic equilibrium inside the plasma, using magnetic probes that are located outside the plasma. The problem can be divided into two parts: (1) solving the homogeneous Grad-Shafranov (GS) or Laplace equation in the vacuum region surrounding the plasma and determining the plasma boundary, and (2) solving the complete GS equation in the plasma region such that the solution matches the solution to (1) at the plasma boundary [Brus-84]. These problems are ill posed: small variations in the boundary data may cause large changes in the solution some distance away. The ill-posedness can be overcome by expanding the flux function in a set of solutions to the homogeneous GS equation and taking only a finite number of terms into account. To solve problem (2), the current distribution must generally be restricted to some physically relevant class.

If, in the vacuum region outside the plasma, the flux function is expanded in a complete set of solutions to the homogeneous GS equation, obtained by separation in toroidal coordinates, the expansion coefficients are called multipole moments. Such moments have been shown to provide a good description of the flux outside the plasma [Alla-86]. The moments method can also be applied to the problem of computing the measured fields and fluxes from a specified equilibrium. A drawback of the method is the absence of simple relationships between these moments and physically more meaningful global plasma parameters.

Current moments, on the other hand, are widely used to obtain such global plasma parameters as the total current and the position of the current centre [Zakh-73]. Since these moments can be easily computed from the magnetic signals, they are often used as plasma control parameters.

This letter presents the relationships between these current moments, i.e. moments of the current density with respect to polynomials in Cartesian coordinates, and the multipole moments, i.e. moments of the flux function with respect to eigenfunctions of the GS equation in toroidal coordinates.

In section 3.2.3 the notation used in this letter is introduced and a definition of the multipole moments is given. In section 3.2.4 exact relationships between current moments and multipole moments are derived.

3.2.3 Toroidal coordinates and multipole moments

The poloidal flux function ψ obeys the GS equation:

$$\begin{aligned} \Delta^*\psi &= -2\pi\mu_0 R j_\phi && \text{inside the plasma} \\ \Delta^*\psi &= 0 && \text{outside the plasma} \end{aligned} \tag{3.1}$$

where $\Delta^*\psi = R^2\nabla(R^{-2}\nabla\psi)$ and j_ϕ is the toroidal current density.

Toroidal coordinates are defined by means of the following relationships with the usual cylindrical coordinates (R, Z, ϕ) [Alla-86; Mors-53]:

$$R = \frac{R_p \sinh\zeta}{\cosh\zeta - \cos\eta}$$

$$Z = \frac{R_p \sin\eta}{\cosh\zeta - \cos\eta} \tag{3.2}$$

where R_p is the pole of the coordinate system. Surfaces of constant ζ are tori with major radii $R_\zeta = R_p/\tanh\zeta$ and minor radii $a_\zeta = R_p/\sinh\zeta$. At $R = R_p$, $\zeta = \infty$, while at infinity and at $R = 0$, $\zeta = 0$. The coordinate η is a poloidal angle and runs from 0 to 2π. These coordinates are particularly suited to toroidal systems.

A complete set of solutions to the homogeneous GS equation $\Delta^*\psi = 0$ is provided through the half integer Legendre functions [Fock-32; Mors-53; Abra-65]:

$$\psi_m^{i,c} = \frac{\sinh\zeta\, P^1_{m-1/2}(\cosh\zeta)\cos(m\eta)}{\sqrt{\cosh\zeta - \cos\eta}}, \tag{3.3a}$$

$$\psi_m^{e,c} = -\frac{\sinh\zeta\, Q^1_{m-1/2}(\cosh\zeta)\cos(m\eta)}{\sqrt{\cosh\zeta - \cos\eta}}, \tag{3.3b}$$

$$\psi_m^{i,s} = \frac{\sinh\zeta\, P^1_{m-1/2}(\cosh\zeta)\sin(m\eta)}{\sqrt{\cosh\zeta - \cos\eta}}, \tag{3.3c}$$

$$\psi_m^{e,s} = -\frac{\sinh\zeta\, Q^1_{m-1/2}(\cosh\zeta)\sin(m\eta)}{\sqrt{\cosh\zeta - \cos\eta}}. \tag{3.3d}$$

The normalization of the Legendre functions is the one adopted by [Abra-65]. It is possible to expand the flux function ψ at any position in space in the toroidal harmonics (3.3):

$$\psi(\theta,\eta) = \sum_{m\neq 0}^{\infty} \left\{ M_m^{i,c}\psi_m^{i,c} + M_m^{e,c}\psi_m^{e,c} + M_m^{i,s}\psi_m^{i,s} + M_m^{e,s}\psi_m^{e,s} \right\}. \qquad (3.4)$$

The expansion coefficients $M_m^{i,c/s}$ and $M_m^{e,c/s}$ are called the internal and external multipole moments, respectively. It has been shown that the expansion coefficients can be obtained from the magnetic measurements by a Fourier analysis of signals with respect to the angle η [Alla-86].

3.2.4 Expression of current moments in terms of multipole moments

The multipole moments are useful as a means to represent the flux function outside the plasma, but are hard to interpret physically. Polynomial current moments, on the other hand, are more open to meaningful interpretation [Zakh-73]. In this section, the relationship between the multipole moments and the current moments is established.

Green's second identity in toroidal geometry states that for two scalar functions $\chi(R,Z)$ and $\psi(R,Z)$, the following equality holds:

$$\int_{\Omega} \frac{1}{\mu_0 R}\left(\psi\Delta^*\chi - \chi\Delta^*\psi \right) dS = \int_{\partial\Omega} \frac{1}{\mu_0 R}\left(\psi\frac{\partial\chi}{\partial n} - \chi\frac{\partial\psi}{\partial n} \right) ds \ . \qquad (3.5)$$

Using $\Delta^*\psi = -2\pi\mu_0 R j_\phi$ (2.1) and taking χ to be a solution to the homogeneous GS equation, $\Delta^*\chi = 0$, one finds

$$\int_{\Omega} \chi j_\phi \, dS = \frac{1}{2\pi\mu_0} \int_{\partial\Omega} \frac{1}{R}\left(\psi\frac{\partial\chi}{\partial n} - \chi\frac{\partial\psi}{\partial n} \right) ds \ . \qquad (3.6)$$

This can be rewritten in toroidal coordinates:

$$q_\chi \equiv \int_{\Omega} \chi j_\phi \, dS = \frac{-1}{2\pi\mu_0 R_p} \int_0^{2\pi} \frac{(\cosh\zeta - \cos\eta)}{\sinh\zeta}\left(\psi\frac{\partial\chi}{\partial\zeta} - \chi\frac{\partial\psi}{\partial\zeta} \right) d\eta \ . \qquad (3.7)$$

With Eq. (3.7) any moment q_χ (subject to $\Delta^*\chi = 0$) of the current distribution j_ϕ can be computed in terms of a line integral of the flux and poloidal field over a ζ-surface enclosing the plasma column. Equations (3.3) and (3.4) can be used to obtain expressions for the expansion in toroidal multipole moments of both ψ and $\partial\psi/\partial\zeta$, and these expressions can be substituted

into Eq. (3.7). The resulting expression can be simplified by observing that $\Delta^*\chi = 0$, so that χ can be expanded in the complete set of toroidal harmonics (3.3). Writing

$$\chi = \sum_{m=0}^{\infty} \left\{ a_m^c \psi_m^{e,c} + a_m^s \psi_m^{e,s} \right\}, \tag{3.8}$$

the integration over η in (3.7) yields an expression for the current moment in terms of a_m, M_m, $P^0_{m-1/2}$, $Q^0_{m-1/2}$, $P^1_{m-1/2}$ and $Q^1_{m-1/2}$. This expression can be simplified further by noting that

$$P^1_{m-1/2}(\cosh\zeta)\, Q^0_{m-1/2}(\cosh\zeta) - P^0_{m-1/2}(\cosh\zeta)\, Q^1_{m-1/2}(\cosh\zeta) = (\sinh\zeta)^{-1}, \tag{3.9}$$

such that the Legendre functions drop out. This yields

$$q_\chi \equiv \int_\Omega \left(\chi j_\phi \right) dS = \frac{1}{\mu_0 R_p} \sum_{m=0}^{\infty} (2-\delta_{m0})^{-1} (m^2 - \tfrac{1}{4}) \left\{ a_m^c M_m^{i,c} + a_m^s M_m^{i,s} \right\}, \tag{3.10}$$

where δ_{ij} is the Kronecker delta, and the $a_m^{c/s}$ are constants which *only* depend on the choice of χ and are determined through Eq. (3.8).

Equations (3.8) and (3.10) are prescriptions by which expressions for the current moments q_χ in terms of the multipole moments can be obtained. Note that the only restriction on χ is that it is a solution to the homogeneous GS equation. Thus it is possible to choose χ such that the resulting current moments correspond to the usual polynomial current moments introduced in [Zakh-73] and often used in tokamak research. Some other families of solutions χ to the homogeneous GS equation are given in [Braa-86a]. Every χ in such a family may be expressed in toroidal coordinates by Eq. (3.2), and subsequently expanded in the manner of Eq. (3.8).

The summation rule

$$\sqrt{\cosh\zeta - \cos\eta} = \frac{\sinh\zeta}{\sqrt{2\pi}} \sum_{m=0}^{\infty} (2-\delta_{m0})\, (m^2 - \tfrac{1}{4})^{-1}\, Q^1_{m-1/2}(\cosh\zeta) \cos(m\eta) \tag{3.11}$$

provides the basis for derivation of many other summation rules that serve to find the expansion of functions χ in toroidal harmonics. Interesting expressions in this respect are of the form $\sum A_m \sinh\zeta\, Q^1_{m-1/2}(\cosh\zeta)\cos(m\eta)$ or $\sum A_m \sinh\zeta\, Q^1_{m-1/2}(\cosh\zeta)\sin(m\eta)$. Defining two differential operators:

$$D_\eta \equiv \frac{\partial}{\partial\eta}, \qquad D_\zeta \equiv \sinh\zeta \frac{\partial}{\partial\zeta} \frac{1}{\sinh\zeta} \frac{\partial}{\partial\zeta}, \tag{3.12}$$

and using (3.9), it is very easy to prove that

$$D_\zeta [\sinh\zeta\, Q^1_{m-1/2}(\cosh\zeta)] = (m^2 - \tfrac{1}{4}) [\sinh\zeta\, Q^1_{m-1/2}(\cosh\zeta)]. \tag{3.13}$$

Obviously, D_ω and D_θ commute. These two operators can be applied a number of times in succession to Eq. (3.11). This results in right-hand sides of the form required, i.e. a summation related to an expansion in the complete set of solutions to the homogeneous GS equation (3.3). Likewise, the left-hand sides are related to the expression in toroidal coordinates of the polynomials defining the current moments (Table 3.1 and Eq. 3.2). Thus one has a straightforward, though tedious, method of obtaining the expansions of Eq. (3.8).

A particularly useful set of polynomials χ_n generating current moments is given by

$$\chi_0 = 1,$$

$$\chi_1 = Z,$$

$$\chi_n = R^n \sum_{k=0}^{\lfloor \frac{n}{2} \rfloor - 1} (-4)^{-k} \frac{(n-2)!}{k!(k+1)!(n-2k-2)!} \left[\frac{Z}{R}\right]^{n-2k-2}, \qquad (n \geq 2) \tag{3.14}$$

where $\lfloor . \rfloor$ denotes rounding to the nearest smaller integer. These polynomials satisfy $\Delta^* \chi_n = 0$.

Expressions of current moments q_χ generated by the polynomials χ_n of eq. (3.14) in terms of the multipole moments were derived for the first few values of n (see Table 3.1). The result for $\chi = 1$ is in accordance with that given in [Desh-83]. The results for other choices of χ have not been published before.

Table 3.1: Expression of current moments in terms of the multipole moments

$\chi = \chi_0 = 1$: (total current)

$$q_\chi^0 = I_p \equiv \int_\Omega (j_\phi) \, dS = -\frac{\sqrt{2}}{2\pi\mu_0 R_p} \sum_{m=0}^{\infty} M_m^{i,c}$$

$\chi = \chi_1 = Z$: (upward displacement of current centre)

$$q_\chi^1 = Z_{cur} I_p \equiv \int_\Omega (Z \, j_\phi) \, dS = \frac{\sqrt{2}}{\pi\mu_0} \sum_{m=0}^{\infty} m \, M_m^{i,s}$$

$\chi = \chi_2 = R^2$: (outward displacement of current centre)

$$q_\chi^2 = R_{cur}^2 I_p \equiv \int_\Omega (R^2 \, j_\phi) \, dS = \frac{2\sqrt{2}R_p}{\pi\mu_0} \sum_{m=0}^{\infty} (m^2 - \tfrac{1}{4}) \, M_m^{i,c}$$

$\chi = \chi_3 = R^2 Z$: (skew ellipticity of current distribution)

$$q_\chi^3 = \int_\Omega (R^2 Z \, j_\phi) \, dS = \frac{4\sqrt{2}R_p^2}{3\pi\mu_0} \sum_{m=0}^{\infty} m \, (m^2 - \tfrac{1}{4}) \, M_m^{i,s}$$

$\chi = \chi_4 = R^2 Z^2 - \frac{1}{4} R^4$: (vertical ellipticity of current distribution)

$$q_\chi^4 = \int_\Omega ((R^2 Z^2 - \tfrac{1}{4} R^4) \, j_\phi) \, dS = -\frac{2\sqrt{2}R_p^3}{3\pi\mu_0} \sum_{m=0}^{\infty} (m^2 + \tfrac{3}{4}) \, (m^2 - \tfrac{1}{4}) \, M_m^{i,c}$$

$\chi = \chi_5 = R^2 Z^3 - \frac{3}{4} R^4 Z$: (upward triangularity of current distribution)

$$q_\chi^5 = \int_\Omega ((R^2 Z^3 - \tfrac{3}{4} R^4 Z) \, j_\phi) \, dS = -\frac{4\sqrt{2}R_p^4}{15\pi\mu_0} \sum_{m=0}^{\infty} m \, (m^2 + \tfrac{11}{4}) \, (m^2 - \tfrac{1}{4}) \, M_m^{i,s}$$

$\chi = \chi_6 = R^2 Z^4 - \frac{3}{2} R^4 Z^2 + \frac{1}{8} R^6$: (outward triangularity of current distribution)

$$q_\chi^6 = \int_\Omega ((R^2 Z^4 - \tfrac{3}{2} R^4 Z^2 + \tfrac{1}{8} R^6) \, j_\phi) \, dS = \frac{4\sqrt{2}R_p^5}{45\pi\mu_0} \sum_{m=0}^{\infty} (m^4 + \tfrac{13}{2} m^2 + \tfrac{45}{16}) \, (m^2 - \tfrac{1}{4}) \, M_m^{i,c}$$

3.2.5 Acknowledgements

The author would like to express his gratitude to Dr. N.J. Lopes Cardozo for many inspiring discussions and careful reading of the early versions of this letter. In preparation for this final version, the criticism by Dr. B.J. Braams has been invaluable.

This work was performed under the Euratom-FOM Association agreement with financial support from NWO and Euratom.

3.3 Interpretation of the current moments

3.3.1 Approximation of the current density profile from the current moments

Having obtained the current moments, the information present in these moments can be used to reconstruct the current profile, provided a choice for the radial distribution of the current profile is made, since the moments only contain information on the total current flowing and its poloidal distribution. This section presents a way to perform such a reconstruction.

The inner product $(\chi_i,\chi_j)_w$ is defined by $(\chi_i,\chi_j)_w \equiv \int w\chi_i\chi_j \, dS$ where $w = w(R,Z)$ is a weight function, and the χ_i are the generating functions for the current moments that have been introduced in the previous section. The integration is over the R-Z plane. The corresponding norm is given by $\|\chi_i\|_w \equiv (\chi_i,\chi_i)_w^{1/2}$.

By means of the Gram-Schmidt procedure [Mors-53] the functions χ_i are orthonormalized with respect to the inner product $(\chi_i,\chi_j)_w$. This yields a set of functions ξ_i satisfying $\Delta^*\xi_i = 0$ and $(\xi_i,\xi_j)_w = \delta_{ij}$.

By analogy with (3.10), current moments $q_\xi^i = \int \xi_i \, j_\phi \, dS = (\xi_i, w^{-1} j_\phi)_w$ are defined. Then

$$j'_\phi = \sum_{i=0}^{\infty} q_\xi^i \, \xi_i \, w \tag{3.15}$$

is the best approximation to j_ϕ in the space spanned by $\{\xi_i w\}$. Note that this expansion is not necessarily a solution to the GS equation because it is not of the form $j_\phi = R^{-1}f_1(\psi) + Rf_2(\psi)$.

The expansion (3.15) should converge quickly, so the zeroth-order approximation to j_ϕ, j_ϕ^0, should in some sense be close to a realistic current profile. Note that from (3.15) follows $j_\phi^0 = q_\xi^0 w$, so that this demand is in fact a restriction on the shape of w. Also, w must be such that it produces a well-behaved inner product, or, in other words, w must be a function of rapid decay (i.e. fall off more rapidly than the inverse of any polynomial in R and Z), such that $(\chi_i,\chi_j)_w$ is integrable for all $\{\chi_i,\chi_j\}$. These two considerations lead to the choice of a Gaussian for w:

$$w = \frac{1}{2\pi\sigma_R\sigma_Z} \exp\left[-\frac{(R-R_w)^2}{2\sigma_R^2} - \frac{(Z-Z_w)^2}{2\sigma_Z^2}\right]. \tag{3.16}$$

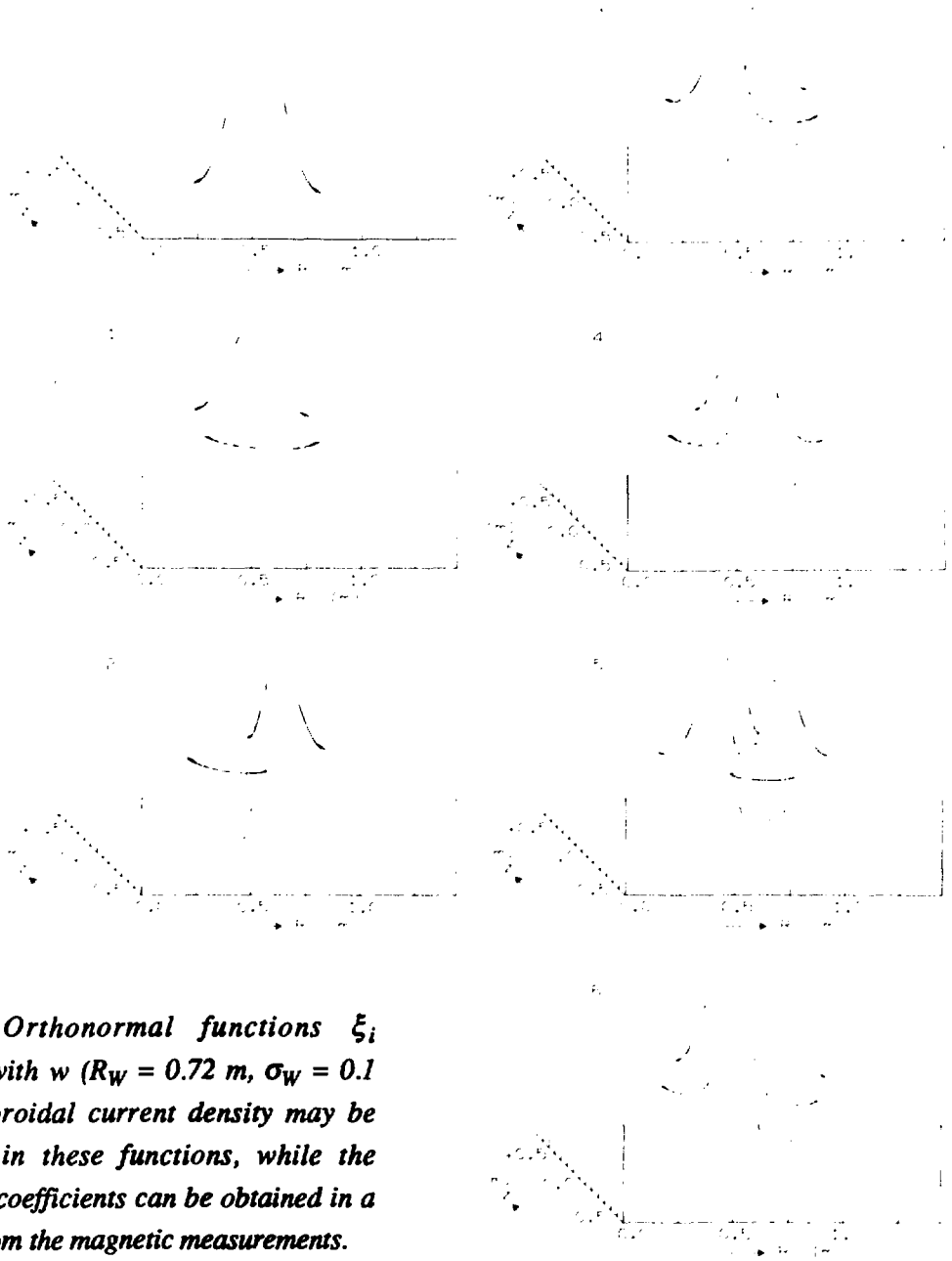

Fig. 3.1 Orthonormal functions ξ_i weighted with w (R_W = 0.72 m, σ_W = 0.1 m). The toroidal current density may be expanded in these functions, while the expansion coefficients can be obtained in a fast way from the magnetic measurements.

The normalization of w is such that $\|1\|_w = 1$. R_w, Z_w, σ_R and σ_Z can still be chosen. R_w, Z_w will typically correspond to the centre of a current distribution, while σ_R and σ_Z correspond to its width.

The orthonormalization of the set χ_i in Eq. (3.14) with respect to the inner product defined above yields a set of ξ_i. The functions $\xi_i w$ (i = 0,...,6) are displayed in Fig. 3.1 (for simplicity, Z_w=0, $\sigma_R = \sigma_Z = \sigma_w$ was taken).

In general, the expansion (3.15) is truncated at some low mode number. It is important to observe that the χ_i do not form a complete set. Nevertheless the total current, current weight centre, etc. can still be produced accurately.

When applying this method in practice, the approximation (3.15) can be optimized by choosing an optimal R_w to fit a particular measurement. This is achieved by setting $R_w = [q_\chi^2/q_\chi^0]^{1/2}$ (see Table 3.1).

3.3.2 Definition of characteristic parameters from the current moments

The relation between the current moments and the spatial distribution of current has been elucidated in the previous section. It is clear that it must also be possible to obtain values for the position of the current weight centre, the current distribution ellipticity etc. from the current moments. Below, a way of defining these quantities is suggested.

Moment	Definition	Interpretation (unit)
0	$I_p = q_0$	Total current (A)
1	$Z_{cur} = q_1/q_0$	Vertical displacement of current centre (m)
2	$R_{cur} = \sqrt{q_2/q_0}$	Horizontal displacement of curr. centre (m)
3	$\varepsilon_s = \frac{1}{q_0}\left(q_3 - \frac{q_1 q_2}{q_0}\right)$	Skew ellipticity of current distribution (m^3)
4	$\varepsilon_v = \frac{1}{q_0}\left(q_4 - \frac{q_1^2 q_2}{q_0^2} + \frac{1}{4}\frac{q_2^2}{q_0}\right)$	Vertical ellipticity of current distr. (m^4)
5	$\Theta_u = \frac{1}{q_0}\left(q_5 - \frac{q_1^3 q_2}{q_0^3} + \frac{3}{4}\frac{q_1 q_2^2}{q_0^2}\right)$	Upward triangularity of current distr. (m^5)
6	$\Theta_o = \frac{1}{q_0}\left(q_6 - \frac{q_1^4 q_2}{q_0^4} + \frac{3}{2}\frac{q_1^2 q_2^2}{q_0^3} - \frac{1}{8}\frac{q_2^3}{q_0^2}\right)$	Outward triangularity of current distr. (m^6)

The definitions of the moments 0, 1 and 2 are trivially obtained from Table 3.1. The definitions of the higher-order moments are such that they do not depend the total current or on the location of the current centre.

3.4 Application to RTP

3.4.1 Determination of multipole moments from the measurements

The multipole moments can be computed from volume integrals over the current distribution inside (internal moments) and outside (external moments) some control surface $\zeta = \zeta_0$ [Alla-86]. If this control surface intersects a region with non-zero current, then the moments are dependent on ζ_0. However, if this control surface is chosen such that it lies completely within a currentless region and the only current flowing inside the control surface is the plasma current, then the moments are independent of the control surface and the internal moments correspond to the plasma current and the external moments correspond to external coil currents. Of course the expansion of ψ is only valid in the currentless region, or, more precisely, in the section of space between two ζ = constant surfaces (a toroidally annular region) where the current density is identically zero [Brus-84].

If the control surface $\zeta = \zeta_0$ can be chosen to coincide with a set of magnetic pick-up coils, then the determination of the moments (internal and external) from such measurements becomes particularly straightforward. It has been shown that the expansion coefficients can be obtained from the magnetic measurements by a Fourier analysis of signals with respect to the angle η [Alla-86].

However, at RTP the radial and poloidal components of the magnetic field are not measured at the same minor radius (ρ = const.) surface. Therefore the moments are determined by making a fit of the radial and poloidal magnetic field measurements to the relevant expressions in terms of the moments with the moments as regression variables:

$$B_\eta = \sum_{m=0}^{M_{max}} M_m^{i,c} f_m^{i,c}(\eta,\zeta) + M_m^{i,s} f_m^{i,s}(\eta,\zeta) + M_m^{e,c} f_m^{e,c}(\eta,\zeta) + M_m^{e,s} f_m^{e,s}(\eta,\zeta)$$

$$B_\zeta = \sum_{m=0}^{M_{max}} M_m^{i,c} g_m^{i,c}(\eta,\zeta) + M_m^{i,s} g_m^{i,s}(\eta,\zeta) + M_m^{e,c} g_m^{e,c}(\eta,\zeta) + M_m^{e,s} g_m^{e,s}(\eta,\zeta)$$

where the f and g are known functions that can be found from Eq. (3.4) by taking the appropriate derivatives. The value of M_{max} is found from the requirement that the regression must be overdetermined. If N_η is the number of poloidal field measurements and N_ζ the number of radial field measurements, then

$$M_{max} = \min (M_{max}^{err}, \text{ int } (\frac{N_\eta + N_\zeta + 2}{4})),$$

where M_{max}^{err} is some preset maximum. A sensible choice for M_{max}^{err} can be made by studying the effect of measurement errors on the determination of the moments. This is discussed in the next section.

3.4.2 Sensitivity to measurement errors of multipole and current moments

The multipole expansion provides an accurate description of the flux outside the plasma, but the convergence of the expansion of the internal flux near the pole of the coordinate system (i.e. near the centre of the torus) depends strongly on the location of this pole. Therefore the reconstruction of the internal flux near the pole generally requires a high number of moments, and if the expansion is truncated at a low mode number the reconstruction will be bad, even though it is good further away from the pole. Note, however, that the pole generally lies within the plasma, such that the reconstruction is not valid in that region anyway. The reconstruction of the external fields is less sensitive to the location of the pole.

The current moments are computed from the internal multipole moments and describe the amplitude, location and shape of the current distribution (section 3.3). Their value likewise does not depend on the choice of pole and provides a reliable source of information on the total current and the poloidal distribution of the current density.

In this section, an error analysis is carried out for the determination of these moments in the specific geometry of the Rijnhuizen Tokamak Petula (RTP). RTP has a circular cross-section, around which measuring coils and flux loops are positioned (Fig 3.2).

Once a choice for the coordinate system is made, three sources of errors can be distinguished: (1) systematic errors due to e.g. misalignments of coils or calibration errors, (2) measurement noise and (3) computational inaccuracies in determining the moments using either a Fourier analysis or a regression method as described in the previous section.

It has been shown [Alla-86] that for an aspect ratio of 3.16 (which is close to the RTP aspect ratio R/a = 3.38) and measurement errors of 1%, it is very difficult if not impossible to determine any but the first four multipole moments.

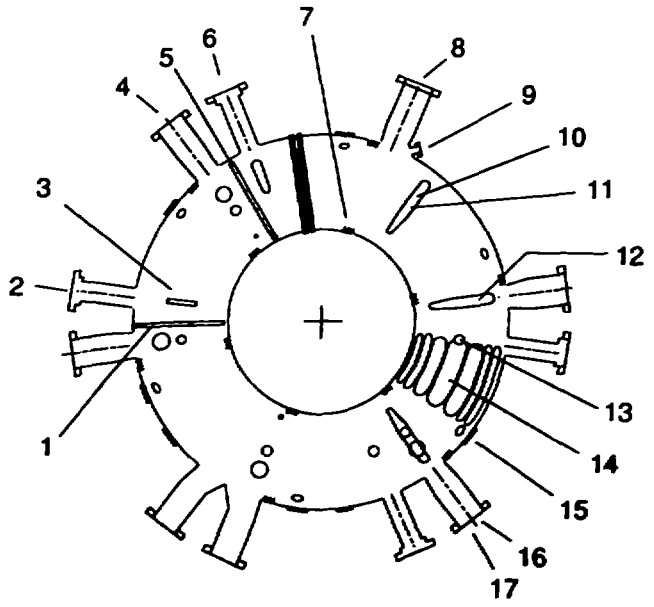

1 circular limiter
2 ECE polychromator
3 top-bottom limiter
4 heterodyne ECE
5 magnetic pick-up coils
6 neutral particle analyzer
7 transmitted power measurement
8 ECRH
9 soft X-ray pulse height analyses
10 X-ray tomography
11 visible light tomography
12 multi-channel interferometer/polarimeter
13 2 mm interferometer
14 flux loops
15 hard X-ray monitor
16 Thomson scattering
17 visible light spectroscopy

Fig. 3.2 Schematic of RTP (top view) displaying the toroidal location of the main diagnostics.

The combined effects of the errors (2) and (3) on the determination of the moments have been investigated for the case of RTP. Wire model simulations of the plasma and full equilibrium simulations were used. Below the results of both computational analyses are presented.

In the wire model, the plasma current distribution is simulated by means of a finite set of current-carrying toroidal wires. Four wires were positioned in the centre of the tokamak to simulate the plasma, and four wires at the locations of the external coil groups of RTP to simulate the external currents. The currents through these wires and also the positions of the plasma-simulating wires were varied, and the corresponding magnetic fields and fluxes in measuring coils and flux loops around the torus were computed. The generated current moments had, for the low orders that were studied, a greater range of variation than are expected in reality. Subsequently, the multipole moments were determined both directly from the known current distribution (cf. [Alla-86]) and by the method described in this article from the measured fluxes and poloidal magnetic fields.

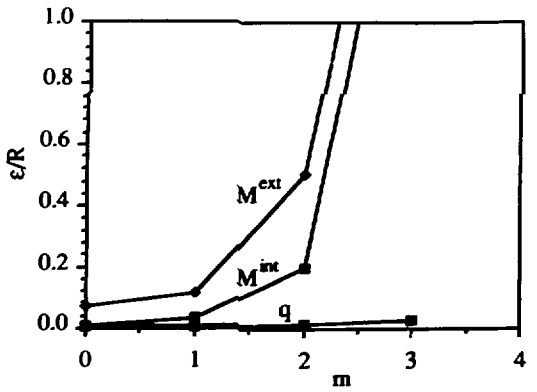

Fig. 3.3 Reproduction error of moments as determined using a wire model. The vertical axis is the spread, ε, of the moments, recalculated from simulated magnetic measurements, divided by their range of variation over the simulations, R (see text). The horizontal axis is the moment index.

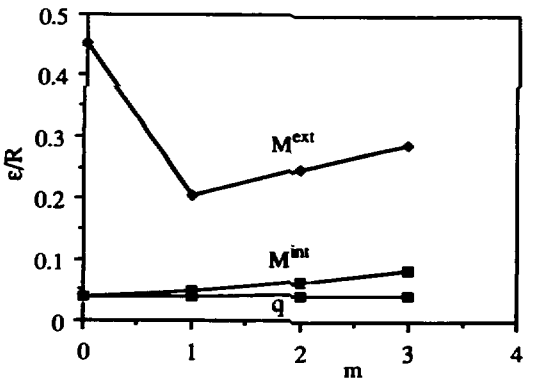

Fig. 3.4 Reproduction error of moments as determined using a full equilibrium model and function parametrization. This figure should be compared to Fig. 3.3.

Fig. 3.3 shows the quantity ε/R for internal and external multipole moments and current moments. The reconstruction error, ε, is the standard deviation of the difference between the known moment and the moment as computed from measurements perturbed with 3 % random noise, as found from a large number of calculations using different wire positions and currents. The range, R, is the range of variation of each moment. The current moments labeled as 0,1,2,3 are to be identified with the moments 0,2,4,6 defined in the previous section; since an up-down symmetric case is studied the odd current moments are all 0. The graph indicates that (1) the accuracy of the moment determination decreases strongly with increasing m; (2) the determination of the external moments is less accurate than that of the internal moments, and both types of multipole moments are determined less accurately than the current moments.

It should be noted, however, that the range of variation of the moments may not reflect a range as occurring in a real experiment. Therefore a similar study was done using Function

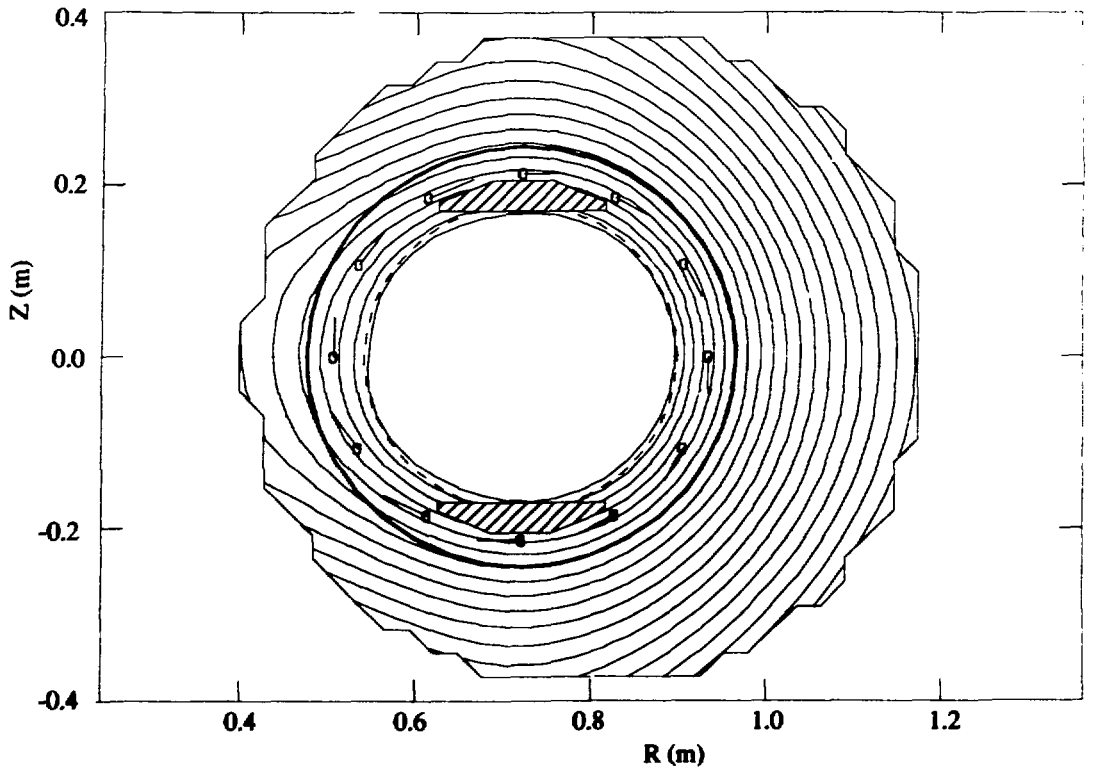

Fig. 3.5a Figure displaying the RTP vacuum vessel (solid line), circular limiter (dashed line), top- and bottom limiters (shaded polygons), and pick-up coils (small circles) in a poloidal cross-section. From the magnetic measurements (indicated by the flags departing from the pick-up coils, flux loop measurements not shown), the internal and external moments are determined as explained in the text, and the total poloidal flux outside the plasma is reconstructed. The last flux surface touching any of the limiters is determined, and this is taken to be the plasma boundary.

Parametrization (see next chapter) using a realistic plasma equilibrium code. The results are presented in Fig. 3.4. RTP plasmas were simulated and the corresponding measurements computed. The measurements were perturbed with 3% random noise and the moments were recomputed. The graph shows ε/σ, where ε is defined as above while σ is the standard

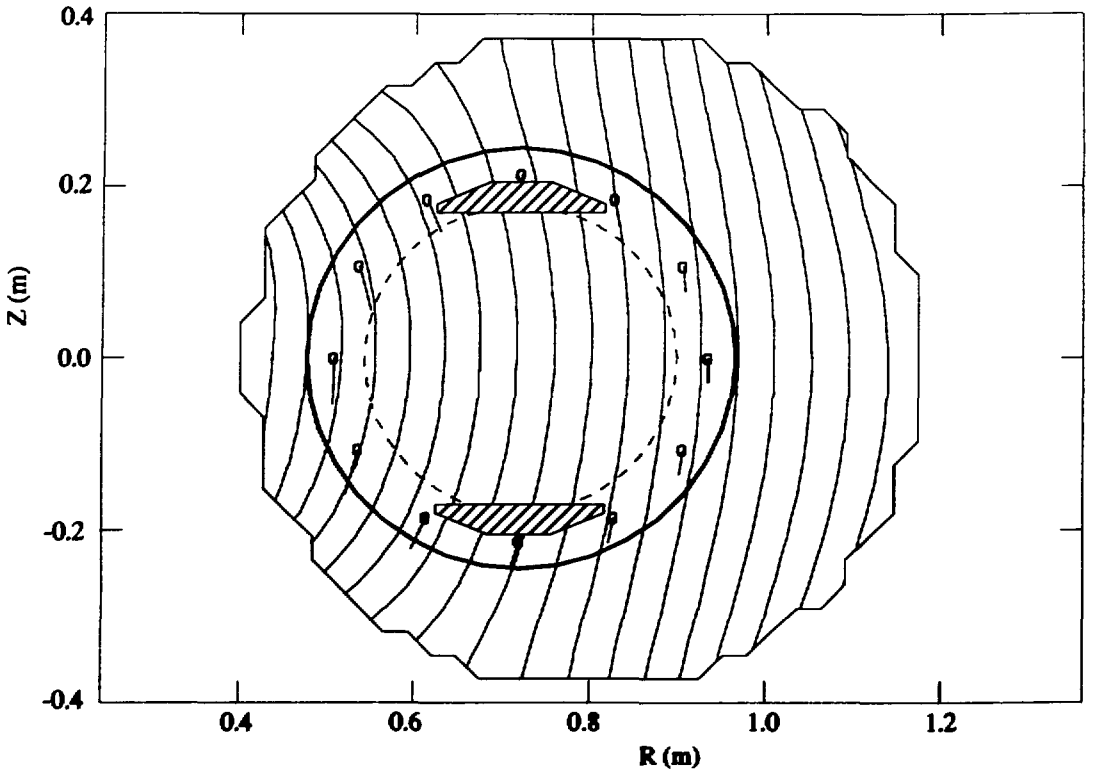

Fig. 3.5b Figure displaying the contribution of the external field to the total poloidal flux. The moments expansion makes it possible to distinguish between internal (plasma) and external (field coils) contributions. The flags on the pick-up coils show the strength and direction of this external field contribution, however not on the same scale as in Fig. 3.5a.

deviation of the moments, versus m. Due to the fact that a realistic plasma model is used, the distribution of poloidal harmonics in the flux function is different, and the reconstruction does not deteriorate so dramatically with m as in Fig. 3.3. Remarkably, the current moments are determined with an accuracy better than 5% for $m \leq 3$. The fact that both here and in the previous figure the external moments are more inaccurate than the other moments is due to the fact that the external expansion contributes less to the total flux at the measurement coil positions than the internal expansion.

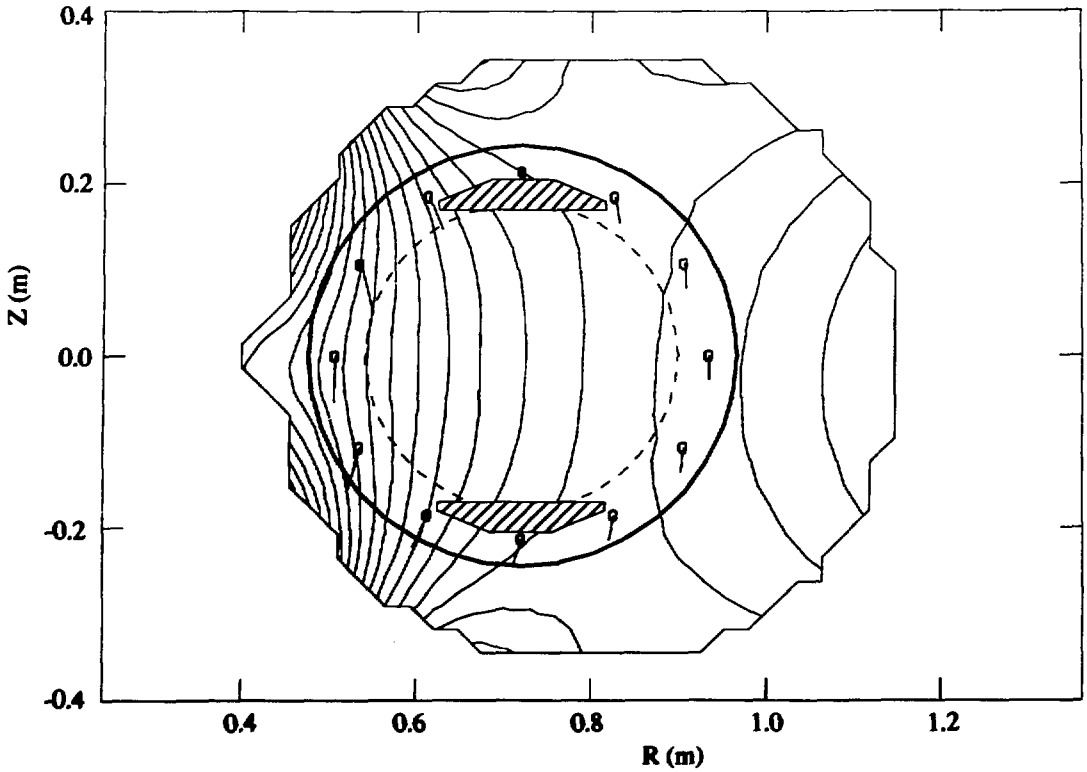

Fig. 3.5c Contours of the strength of the external magnetic field displayed in Fig. 3.5b. The field flags are the same as in Fig. 3.5b.

3.4.3 Reconstruction of the magnetic field at RTP

A program has been written to determine the multipole moments at RTP using the method described in section 3.4.1. These moments were subsequently used to reconstruct the flux and the magnetic field outside the plasma, and the external part of the flux and the field in the whole region within a toroidal coordinate surface ζ = const within the external field coils. The position and shape of the last flux surface touching the limiter was also computed. Strictly speaking, the expansion is only valid outside the largest coordinate surface ζ = const that touches the plasma, but since the plasma is nearly circular the expansion was continued inward to the plasma surface. Due to a sensible choice of the pole R_p, the error made in the flux determination near the plasma boundary is small.

Fig. 3.5a shows flux contours outside the plasma for a typical RTP discharge, and the plasma boundary. Fig. 3.5b shows the contribution of the external flux to the total field at the same moment. Fig. 3.5c shows contours of the absolute value of the external poloidal magnetic field.

3.5 Discussion

In the previous sections the multipole and current moments were studied. In the following the relative merits of these two systems of expansion are discussed.

The current moments contain less information than the multipole moments (internal and external). Firstly, because they can be computed from poloidal field measurements only; and secondly because the current moments can be expressed as infinite sums of the internal moments, as was demonstrated. It follows that the current moments are independent of external currents. A great advantage is the independence of the current moments of the choice of coordinate system. The internal multipole moment expansion, on the other hand, may require many harmonics for an accurate description of the flux function if the pole is badly chosen, even if the information contained in them is identical to that contained in the current moments.

Both systems of moments provide information on the poloidal distribution of current, but not on the radial distribution. Note that this is typical of the MHD plasma equilibrium problem: in the absence of radial information from other diagnostics than magnetic measurements, all equilibrium solvers have to restrict the class of possible solutions in the plasma by assuming some radial profile shapes. Due to the toroidal effect and ellipticity of the plasma it is sometimes possible to extract some information on the radial distribution of current, but RTP, being circular, is a typical case where this is extremely difficult.

The multipole moments, unlike the current moments, provide information on the total flux and field outside the plasma and inside the external conductors. Thus it is possible to make a link with a Grad-Shafranov solver at the plasma boundary, providing a way to solve the basic MHD equilibrium problem mentioned at the beginning of this chapter.

4. Function parametrization

4.1 Introduction

This chapter is devoted to the method of Function Parametrization (FP) and its applications to several tokamaks. Section 4.2 is a reproduction of the paper *Function Parametrization: a fast inverse mapping method* [Mill-91b] in which a mathematical description of the method is given and the application of the method to the Rijnhuizen tokamak RTP is discussed. Section 4.3 is a reproduction of the paper *Application of Function Parametrization to the analysis of polarimetry and interferometry data at TEXTOR* [Mill-91a].

4.2 Function Parametrization: a fast inverse mapping method

B.Ph. VAN MILLIGEN, N.J. LOPES CARDOZO

4.2.1 Abstract

Function Parametrization (FP) is a method to invert computer models that map physical parameters describing the state of a physical system onto measurements. It finds a mapping of the measurements onto the physical parameters that requires little computing time to evaluate. The major advantages of FP over other analysis methods are: it is quite general; it is fast, allowing real-time control of experiments; it allows a thorough error analysis; it can provide insight into the structure of the computer program used to model the experiment; it can be used to analyze sets of dissimilar measurements; it can be used to study the adequacy of certain new measurements for determination of specific physical parameters.

FP is tested on the reconstruction of plasma equilibria from magnetic measurements. As a result, some important parameters describing the plasma state are shown to be recoverable in a fast and reliable manner.

4.2.2 Introduction

In many experimental situations, the physicist is faced with the problem of interpreting a set of measurements which are implicitly related to the physical parameters of the system under study. In many cases, a model is available that allows explicit simulation of measurements given the physical state of the experiment: the model is a mapping of physical parameters onto measurements. The problem of data interpretation is to find the inverse of the mapping.

However, if the model is complex, this inverse mapping may be hard or impossible to find, or it may not even exist. If a computer model of the experiment is available, the experimenter involved in the interpretation of a set of measurements is then forced to run the model many times, each time adjusting the physical parameters until suitable agreement with his measurements is obtained. If the number of experiments to be done is large, then this iterative solution may become very time-consuming to the point of hindering further advances of the research.

Function Parametrization (FP) is the name for a collection of techniques that tackle the problem of finding an inverse mapping of a computer model systematically. An important ingredient is the reduction of dimensionality of the measuring space such that redundant information is rejected. This procedure must be carried out with great care in order not to discard significant data. The inverse mapping is determined by analyzing a database of simulated experiments. The result of the effort is a simple mapping of a set of measurements onto the physical parameters of the system.

FP is quite generally applicable to many problems of interpretation in modern-day physics. It allows a fast interpretation of measurements, up to the point of real-time control of the experiment. In addition, it can supply insight into the structure of the computer model describing the experiment by displaying relationships and dependencies between parameters. FP can be used to predict the relevance of a new type of measurement to the determination of a specific (set of) parameter(s) even before the measurement device is built. Finally, FP allows a thorough error analysis to be set up, making a clear distinction between systematic and statistical errors, which may not be straightforward with the iterative solution methods mentioned above.

The method of Function Parametrization was first formulated by H. Wind at CERN [Wind-72; Wind-84], where it was applied to the problem of track finding. The method was then applied to equilibrium determination at ASDEX by Braams, Jilge and Lackner [Braa-86b]. Their work was continued by McCarthy [McCa-86].

FP relies primarily on well-known statistical methods and the basic principle has been elucidated briefly in a previous publication [Braa-86b]. This paper attempts to provide a comprehensive description of the method. New additions presented are: (1) an explanation of the behaviour (exponential decay) of the eigenvalues in principal component analysis; (2) a demonstration of the so-called Latent Root Regression; (3) the rationalization of cutoff criteria determining the dimensionality of the regression; (4) a detailed error analysis method. FP is demonstrated with an application to tokamak plasma physics.

4.2.3 Theory of Function Parametrization

4.2.3.1 Introduction

We consider the situation where a physical model of an experiment is available that allows computation of measurements if the state of the system is known, but where the model is complex enough such that inversion is difficult or impossible.

The state of the physical system, *p*, is modelled in terms of a finite set of N_p parameters $(p_1,\ldots,p_{Np}) = \vec{p}$ (Appendix 4.2.6.3 provides a table of notation). Often physical quantities describing the system are functions of e.g. space, and these quantities need to be represented in a parametric form in this formalism (hence the name 'Function Parametrization'). This necessarily involves a reduction in the number of states representable within the context of the parametric form of the model with respect to the full model. But because we are only occupied with those physical states and measurements that are described by a computer model it is always possible to cover all relevant system states by parametric representations.

The N_q measurements that are made on the physical system in the state *p* are written as a vector $(q_1,\ldots,q_{Nq}) = \vec{q}$. The computer model $\vec{M}$ that allows computation of $\vec{q}$ from $\vec{p}$ can be understood to be a mapping $\vec{q} = \vec{M}(\vec{p})$, which can be non-linear. Within the context of the model this mapping is exact. If the model is to make any physical sense, the computation of $\vec{q}$ should be stable against small variations in $\vec{p}$. On the other hand, it is obvious that most models should be considered to be essentially projections (the information content of the measurements is less than that of the physical parameters), i.e. two physical states $\vec{p}$ and $\vec{p}'$, $\vec{p} \neq \vec{p}'$, may map to the same measurement: $\vec{q} = \vec{q}'$. Due to finite measurement accuracy this can be formulated even stronger: two different physical states $\vec{p}$ and $\vec{p}'$ may map to two measurement vectors that are indistinguishable given a certain limited measuring accuracy, $\|\vec{q}-\vec{q}'\| < \delta$ for some norm. Therefore the inverse mapping of $\vec{M}$ is not single-valued. This situation reflects either a fundamental problem in the modelling procedure or a lack in number or accuracy of the

measurement data. The problem can be circumvented by restricting the parametrization of p by means of the choice of $\vec{p}$, such that the inverse mapping, if found, would be single-valued. Even if this is not possible FP can find an inverse mapping, albeit that some components of $\vec{p}$ will be ill-determined, reflecting the non-single-valuedness of the inverse mapping. It will also be shown in the following how the ill-determinedness of some parameters can be detected. Thus, apart from its practical use as an analysis tool, the method can also be used to obtain rudimentary insight into the structure of the model $\vec{M}$ or even the adequacy of the measurements for the purpose of determining the physical parameters $\vec{p}$.

The method of Function Parametrization (FP) consists of three steps: (1) a database is constructed containing a large number (N) of simulations $\vec{p} = \vec{p}^{\alpha}$ (α = 1,...,N), where $\vec{p}^{\alpha}$ is chosen to lie in the subspace of $\mathbf{R}^{Np}$ covering (at least) all actual physical states expected to occur in the real experiment. The model $\vec{M}$ is used to compute the corresponding measurements $\vec{q} = \vec{q}^{\alpha} = \vec{M}(\vec{p}^{\alpha})$. (2) the data base is subjected to a statistical analysis, which yields a mapping $\vec{p} = \vec{F}(\vec{q}) + \vec{\varepsilon}$,where $\vec{\varepsilon}$ is a small error term. The statistical analysis can be subdivided into two parts: (a) a dimension reduction step yielding $\tilde{q} = \vec{g}(\vec{q})$ and (b) a regression yielding $\vec{p} = \vec{f}(\tilde{q})$. Thus $\vec{F}(\vec{q}) = \vec{f}(\vec{g}(\vec{q}))$. (3) the mapping $\vec{F}$ is used in data analysis to interpret real measurements $\vec{q}$.

We make a distinction between a reduced set of parameters $\{p_j, j \le N_{id}\}$, $N_{id} \le N_p$, that are *sufficient* to identify the state p uniquely, and the remaining parameters $\{p_j, N_{id} < j \le N_p\}$ that are therefore dependent on $\{p_j, j \le N_{id}\}$ in the context of the model $\vec{M}$. Note that we do not exclude the possibility that there may be some hidden dependencies (e.g. through some external constraint) between the $\{p_j, j \le N_{id}\}$. Generation of the data base involves selecting values for the parameters $\{p_j, j \le N_{id}\}$, and feeding them to the model $\vec{M}$ which will then yield both $\{p_j, N_{id} < j \le N_p\}$ and $\vec{q}$. Appendix 4.2.6.1 gives some suggestions for parameter selection.

4.2.3.2 Dimension reduction

There are two reasons for performing the dimension reduction $\vec{g}(\vec{q})$. Firstly, an attempt to fit the components of $\vec{p}$ with linear, quadratic etc. functions of the raw measurement vector $\vec{q}$ in order to determine the mapping $\vec{p} = \vec{F}(\vec{q}) + \vec{\varepsilon}$ is bound to fail if N_q is large. If we take $\vec{F}$ to be a polynomial model of degree k, it needs of the order of $N_q^k/(k!)$ fit coefficients for each physical parameter. The number of model simulations needed to determine these coefficients is considerably larger. Therefore a method by which the dimensionality of the measuring space can be reduced without discarding essential information is required.

Secondly, the measurements are likely to exhibit mutual (linear) dependencies that would make the regression $\vec{f}(\vec{q})$ unstable. Dimension reduction provides a means to stabilize the regression by removing collinearities.

The well-known method of Principal Component Analysis (PCA) achieves dimension reduction by discarding linear combinations ('principal components') of the measurements that show little variation over the database, assuming that they have little relevance in the prediction of parameter behaviour.

This may in some cases not be the best method, because it may be that important information is concealed in principal components that show little variance (e.g. a physical parameter is proportional to a linear combination of the measurements that is almost, but not quite, constant in the database). Conversely, it may be that little information is contained in components that show a large variance (but are largely uncorrelated to the physical parameters of the problem). If either of these are the case, then Latent Root (LR) analysis may be of use.

Principal Component Analysis

The physical parameters $\vec{p}$ and the measurements $\vec{q}$ are normalized. The normalized vectors are called $\bar{p}$ and $\bar{q}$:

$$\langle x\rangle_j = \frac{1}{N}\sum_{\alpha} x_j^{\alpha}, \qquad \sigma_j^2(x) = \frac{1}{N-1}\sum_{\alpha}(x^{\alpha}-\langle x\rangle)_j^2 \tag{4.1a}$$

$$\bar{x}_j^{\alpha} = (x_j^{\alpha}-\langle x\rangle_j)/\sigma_j \qquad (j = 1, ..., N_x;\ \alpha = 1, ...,N;\ x = p,q) \tag{4.1b}$$

Here $\langle x\rangle_j$ is the average value of x_j in the data base, and σ_j its spread (i.e. standard deviation).

The dispersion matrices of p and q are computed from :

$$D_{ij}^{x} = \frac{1}{N-1}\sum_{\alpha}\bar{x}_i^{\alpha}\bar{x}_j^{\alpha} \qquad (i,j = 1, ..., N_x;\ \alpha = 1, ...,N;\ x = p,q) \tag{4.2}$$

The diagonal of D^x contains the squared standard deviations of the $\bar{x}_j^{\alpha}$, which were normalized to 1. The off-diagonal elements of D^x are the correlations between the components of $\bar{x}_j^{\alpha}$. D^x is a real, symmetric, positive definite matrix. The eigenvalues of D^x are sorted such that $\lambda_1^x \geq \lambda_2^x \geq ... \geq \lambda_{N_x}^x \geq 0$. The corresponding orthogonal eigenvectors $D^x\cdot\vec{e}_j = \lambda_j^x\vec{e}_j$ are normalized, $|\vec{e}_j| = 1$.

We define new 'transformed' variables

$$\tilde{x}_j^{\alpha} = \vec{e}_j \cdot \bar{x}^{\alpha}. \qquad (j = 1, ..., N_x;\ \alpha = 1, ..., N;\ x = p,q) \tag{4.3}$$

Thus, the components $\tilde{x}_j^{\alpha}$ of $\tilde{x}^{\alpha}$ are linear combinations of the $\bar{x}_j^{\alpha}$. They have a standard deviation of $\sqrt{\lambda_j}$, and are uncorrelated within the data base. In the following, we shall omit the index α.

By inspection of the eigenvalues, some important remarks can be made about the model $\vec{M}$. If $\vec{M}$ is a purely linear model, then for x = p,q all λ_j^x for $j > N_{id}$ are equal to 0. In any model, if a component of $\vec{x}$ is linearly dependent on one or more of the independent components of $\vec{x}$, then the variance of the dependent component is accordingly reduced and the linearly dependent part of its variance is added to the variance of the independent components.

This is an important observation and we shall now illustrate it with a simple example. Suppose we have two measurements $\bar{q}_1$ and $\bar{q}_2$, both normalized in the sense of Eq. (4.1), i.e. $\sigma(\bar{q}_1) = \sigma(\bar{q}_2) = 1$. Suppose that $\bar{q}_2$ is of the form

$$\bar{q}_2 = \bar{q}_2^{i} + \beta \bar{q}_1, \tag{4.4}$$

where $\bar{q}_2^{i}$ is linearly independent of $\bar{q}_1$ and β is the covariance between $\bar{q}_1$ and $\bar{q}_2$. Then $\sigma^2(\bar{q}_2^{i}) = 1 - \beta^2$. Computing the dispersion matrix yields:

$$D^q = \begin{pmatrix} 1 & \beta \\ \beta & 1 \end{pmatrix} \tag{4.5}$$

Eigenanalysis yields eigenvalues $\lambda_1 = 1 + \beta$ and $\lambda_2 = 1 - \beta$, and eigenvectors

$$\vec{e}_1 = \frac{1}{\sqrt{2}}\begin{pmatrix} 1 \\ 1 \end{pmatrix} \qquad \vec{e}_2 = \frac{1}{\sqrt{2}}\begin{pmatrix} 1 \\ -1 \end{pmatrix}, \tag{4.6}$$

such that, according to Eq. (4.3), $\tilde{q}_1 = (\bar{q}_1 + \bar{q}_2)/\sqrt{2}$ and $\tilde{q}_2 = (\bar{q}_1 - \bar{q}_2)/\sqrt{2}$. Using these expressions to compute the variance of $\tilde{q}_1$ and $\tilde{q}_2$ we find $\sigma^2(\tilde{q}_1) = 1 + \beta = \lambda_1$ and $\sigma^2(\tilde{q}_2) = 1 - \beta = \lambda_2$. The covariance becomes $\mathrm{cov}(\tilde{q}_1,\tilde{q}_2) = (N-1)^{-1} \sum \tilde{q}_1 \tilde{q}_2 = 0$, as required. This example clearly demonstrates how the variance $\sigma^2(\tilde{q}_1)$ is incremented by β and the variance $\sigma^2(\tilde{q}_2)$ decremented by the same amount (with respect to $\sigma^2(\bar{q}_1)$ and $\sigma^2(\bar{q}_2)$, respectively) due to the dependency of $\bar{q}_2$ on $\bar{q}_1$ given by $\mathrm{cov}(\bar{q}_1,\bar{q}_2) = \beta$.

Now suppose we have not two, but N_q measurements. Suppose the measurements have mutual linear dependencies given by:

$$\bar{q}_1 = \bar{q}_1^i, \qquad \bar{q}_2 = \bar{q}_2^i + \beta\bar{q}_1^i, \qquad \bar{q}_3 = \bar{q}_3^i + \beta\bar{q}_2^i + \beta\bar{q}_1^i, \text{ etc.} \tag{4.7}$$

Assume $\beta \ll 1$. Thus $\text{cov}(\bar{q}_i, \bar{q}_j) \approx \beta$ $(i \neq j)$. This is a fictional set of measurements in which all measurements are equivalent; they all contain an amount of linearly independent information ($\bar{q}_j^i$) *and* and they all suffer the same amount of collinearity (β) with all other measurements. By analogy with the preceding example, the $\tilde{q}_i$ have standard deviations given by

$$\sigma^2(\tilde{q}_i) = 1 + (N_q - i)\beta - (i-1)\beta = 1 + \beta(N_q - 2i + 1) \tag{4.8}$$

This implies, for β small,

$$\frac{\sigma^2(\tilde{q}_i)}{\sigma^2(\tilde{q}_{i-1})} = \frac{\lambda_i}{\lambda_{i-1}} = 1 - 2\beta, \qquad \text{or } \lambda_i = (1-2\beta)^{i-1}\,\lambda_1 \tag{4.9}$$

It follows that $\lambda_i/\lambda_1 = e^{(i-1)\ln(1-2\beta)}$ (exponential decay of the eigenvalues).

From the fact that the dispersion matrix is computed from the normalized vectors $\bar{x}$ it follows that if $\vec{x}$ shows any linear dependencies between its components at all, $\lambda_1^x > 1$. In an almost purely linear model, where $N_{ld} \approx N_x - N_{id}$ is the number of components of $\vec{x}$ linearly dependent on the minimum set of N_{id} state parameters, the λ_j^x will exponentially decrease in amplitude until $j = N_x - N_{ld}$, when they fall to zero sharply. In a model with complicated as well as linear dependencies (as in the second example above), the λ_j^x fall to zero with j approximately exponentially. The steepness of decay depends on the amount of collinearity between the components of $\bar{x}$ (in the example above: small collinearity means β small, so the decay is slow). We introduce a collinearity parameter β_{coll}, given by

$$\ln(1 - 2\beta_{coll}) = \frac{\partial \ln \lambda_i}{\partial\, i}. \tag{4.10}$$

The more non-linear the model, the slower the decay and the closer β_{coll} comes to 0. Note however that the parameter ranges also influence the decay: if the parameters p_j, $j=1,\ldots,N_{id}$ only vary within narrow ranges a linearized model can give a fairly accurate approximation of a more complex model and the decay of eigenvalues will not be slow.

The $\tilde{x}_j$ are called the 'principal components' of the vector $\vec{x}$. If real measurements are expected to suffer a relative measuring error of ε, it is assumed that those principal components which show a variance over the database of $\lambda_j^x < (3\varepsilon)^2$ are both unimportant in the regression

and difficult to obtain from real measurements, and we discard them. This is equivalent to the statement that the 'signal' of a principal component should be 'significantly above' (i.e. 3ε) the noise level ε. The remaining $\tilde{x}_j$, $j = 1,...,N_s$ are called 'significant variables'.

Latent Root Analysis

The objective of the Latent Root (LR) analysis [Webs-74] is to find those linear combinations of the normalized measurement vector components $\bar{q}_j$, $j=1,...,N_q$ that show least correlation with a physical parameter p_k within the data base, and eliminate this linear combination from the regression analysis. We introduce an 'observation vector' $\bar{s}^k$:

$$\bar{s}^k = (\bar{q}_1,...,\bar{q}_{Nq}, \bar{p}_k) = \{\bar{q}, \bar{p}_k\} \qquad (k = 1,...,N_p). \tag{4.11}$$

Note that we have again omitted the superscript α for convenience. For each simulation in the data base, N_p such 'observation vectors' exist, and they contain the value of all simulated measurements and the k^{th} physical parameter. By analogy with Eq. (4.2), we compute the dispersion matrix:

$$E^k_{ij} = \frac{1}{N-1} \sum_{\alpha} \bar{s}^k_i \bar{s}^k_j \qquad (i,j = 1,...,N_q+1) \tag{4.12}$$

The diagonal of E^k again contains the squared standard deviations of the components of $\bar{s}^k$, which were normalized to 1. The off-diagonal elements are the cross-correlations. Of special interest are the $E^k_{i(Nq+1)}$ elements, the correlations between $\bar{p}_k$ and the measurements.

Analogous to the procedure described above the eigenvalues and corresponding eigenvectors of E^k are computed. The eigenvalues λ^k_j are called latent roots and the normalized eigenvectors $\bar{r}^k_j$ are called latent vectors. They satisfy

$$E^k \bar{r}^k_j = \lambda^k_j \bar{r}^k_j, \qquad |\bar{r}^k_j| = 1 \tag{4.13}$$

The latent roots and vectors have some interesting properties. For instance, if, for some j, $\lambda^k_j = 0$ while $(\bar{r}^k_j)_{Nq+1} \neq 0$ (where $(\bar{r}^k_j)_{Nq+1}$ is the last component of $\bar{r}^k_j$) then Eq. (4.13) demonstrates that there exists an exact linear relationship between $\bar{p}_k$ and $\bar{q}$:

$$\bar{p}_k = -\frac{1}{(\bar{r}^k_j)_{Nq+1}} \sum_{i=1}^{N_q} (\bar{r}^k_j)_i \bar{q}_i \tag{4.14}$$

No regression is necessary as Eq. (4.14) gives a direct relation between measurements and the physical parameter $\bar{p}_k$. But exact linear relationships are hard to find in reality, of course, and this situation will seldomly occur.

If, for some j, both $\lambda_j = 0$ and $(\vec{r}_j^{\,k})_{Nq+1} = 0$, there exists an exact linear dependence among the measurements. This non-predictive singularity can be removed by discarding the corresponding $\tilde{q}_j$, where

$$\tilde{q}_j = \sum_{i=1}^{N_q} (\vec{r}_j^{\,k})_i \, \bar{q}_i \tag{4.15}$$

Again this ideal singularity with exact linear relationships between the measurements will hardly ever occur in reality, but there may very well be near-singularities with $\lambda_j < \gamma$ and $(\vec{r}_j^{\,k})_{Nq+1} < \delta$, where γ and δ are small numbers. The same discarding procedure can be applied once the discriminatory levels γ and δ are set.

The improvement upon the simple PCA procedure is obvious: linear combinations of the measurements that show large variance in the database but have little or no correlation to the physical parameters would have been included in the regression following PCA, but can now be detected and discarded. A disadvantage is that the computing time required both for determining the mapping $\vec{F}$ and its evaluation for real measurements takes considerably more time than the PCA procedure.

4.2.3.3 Regression

In order to obtain the mapping $\vec{F}$, we perform a regression of p_j in terms of functions of $\tilde{q}_k$ for each j. We remark that it is also possible to regress $\tilde{p}_j$, rather than p_j, but the reduction in dimensionality of the fitting problem thus obtained generally does not compensate for the increase in complexity of the results. We demonstrate the procedure with a simple polynomial fit, which takes the form

$$\begin{aligned} p_j = \quad & c_{j0}\phi_0 + \sum_{k=0}^{N_1} c_{j1}^{k}\, \phi_1\left[\frac{\tilde{q}_k}{\sigma_k}\right] + \\ & \sum_{k=0}^{N_2} \sum_{l=k+1}^{N_2} c_{j2}^{kl}\, \phi_1\left[\frac{\tilde{q}_k}{\sigma_k}\right] \phi_1\left[\frac{\tilde{q}_l}{\sigma_l}\right] + \sum_{k=0}^{N_2} c_{j2}^{kk}\, \phi_2\left[\frac{\tilde{q}_k}{\sigma_k}\right] + \ldots + \varepsilon_j, \end{aligned} \tag{4.16}$$

where $N_n \leq N_s$, the ϕ_n are suitable polynomials of the n^{th} degree, $\sigma_j = \sqrt{\lambda_j}$ and the c's are the regression coefficients. The multi-dimensional polynomial functions are referred to as 'basis functions'. N_1 is the number of $\tilde{q}_i$ used in constructing linear basis functions, N_2 the number used in constructing quadratic basis functions, etc. The N_n's can be chosen equal to N_s for all n, but generally results are more stable with respect to measurement noise if only $N_1 \approx N_s$, and the higher-order N_n's are taken smaller. It is actually possible to use stability with respect to measurement noise as a selection criterion for N_n. We shall demonstrate this in section 4.2.4.4. It is now possible to write Eq. (4.16) as a simple sum over fit coefficients multiplied by basis functions, which demonstrates that even for non-linear models the regression problem is linear. We have normalized the significant components to their standard deviations $\sigma_j = \sqrt{\lambda_j}$ (where we have omitted the superscript q) such that the arguments of the polynomials ϕ_n are normalized. This normalization is not strictly necessary. The $\tilde{q}_i/\sigma_i$ are linearly independent: $\text{cov}(\tilde{q}_i/\sigma_i, \tilde{q}_j/\sigma_j) = \delta_{ij}$, where δ_{ij} is the Kronecker symbol. However, the $\phi_n(\tilde{q}_i/\sigma_i)$ should also be linearly independent for all n and i in order for the regression to be well-determined. The Hermite polynomials H_n satisfy this requirement because, if $\phi_n = H_n$, $\text{cov}(\phi_n(y), \phi_m(y)) = \delta_{nm}$ if y is a random variable with a normal probability distribution, which makes them well-suited to our purpose.

From Eq. (4.16) one may deduce that the total number of basis functions, N_{bf}, is given by:

$$N_{bf} = \sum_{n=0}^{N_{or}} \frac{(N_n + n - 1)!}{n!\,(N_n - 1)!}, \tag{4.17}$$

where $N_0 \equiv 1$ and N_{or} is the order of the fitting polynomial (4.16). The N_n's must be chosen such that $N_{bf} < N$ to prevent the regression from being underdetermined, and preferably $N_{bf} \ll N$.

The regression is performed, and the fitting coefficients c in Eq. (4.16) are found. The regression is an ordinary linear least-squares regression. Some caution in carrying out this regression is necessary, because although the principal components are linearly independent, the basis functions that are constructed from them may show small collinearity. But if small collinearity is present, the fitting coefficients c may take on huge meaningless values that do not show up when checking the result of the regression on the unperturbed measurements in the database (see section 4.2.3.4), but can seriously influence the interpretation of real

measurements. Therefore, the significant variables should be perturbed with small random variations ε_{pre} prior to the regression so as to destroy this remaining collinearity completely, while leaving all significant information intact. The amplitude of ε_{pre} is not critical as long as it is small: $\varepsilon_{pre} \approx \varepsilon/3$ is a safe choice (where ε is the typical relative measurement error). Other methods of regularization of the regression might also be used.

Thus, we finally have obtained the mapping $\vec{F}$, which is given in terms of the averages and standard deviations of $\vec{q}$ in the database, the eigenvectors and eigenvalues of D^q, the choice and number of basis functions, and the fitting coefficients c.

4.2.3.4 Error Analysis

The systematic error in the reconstruction of physical parameters by means of the method described above is due to several distinct sources: (1a) the (analytical) model itself is only an approximation of the physical system and the simulated measurements do not contain as much information as the physical quantities in the model, (1b) the parametrization of the model (i.e. the computer model) is a further limitation in the description that may lead to errors, (1c) the dimension reduction as described in section 4.2.3.2 reduces information content of the measurements, and (1d) the regression, being a least-squares fit, reduces the information content even further. The statistical error in the reconstruction is due to (2a) measurement errors, (2b) digitizing noise in the measurements, and (2c) computational inaccuracy in the evaluation of $\vec{F}$. In the following, we indicate how the combined effect of these systematic (except for (1a)) and statistical errors can be estimated. Note that random measurement noise having a normal (Gaussian) distribution may lead to skew statistical errors in the physical parameters. We do not investigate this here, but it is easy to evaluate this skewness numerically using the mapping $\vec{F}$.

Definition of error measures

We study the reliability and sensitivity to measurement noise of the mapping $\vec{F}$ found in section 4.2.3.3. The systematical error introduced by the mapping can be estimated by computing the physical parameters from the simulated data in the database using the mapping $\vec{F}$ and comparing them to the stored values p_j. The systematic reconstruction error is defined as

$$(\varepsilon_j^{sys})^2 = \frac{1}{N-1} \sum_{\alpha} (F_j(\vec{q}_\alpha) - p_{j\alpha})^2, \qquad (4.18)$$

where α runs over all N simulations. ε_j^{sys} is the average systematical error over the data base of the j^{th} parameter.

The statistical error in the computation of p_j can be estimated for any observation $\vec{q}$ individually by

$$(\varepsilon_j^{stat})^2 = \frac{1}{N_{stat}-1} \sum_{\beta} (F_j(\vec{q}+\vec{\varepsilon}_\beta) - F_j(\vec{q}))^2, \tag{4.19}$$

where β runs from 1 to N_{stat} (chosen arbitrarily but not too small) and $\vec{\varepsilon}_\beta$ is a vector of random variables. The standard deviation of the i^{th} component of $\vec{\varepsilon}_\beta$, $\sigma(\varepsilon_{\beta i})$, is equal to the measurement error in the i^{th} measurement. ε_j^{stat} is a function of $\vec{q}$ and therefore variable over the data base. We compute ε_j^{stat} at the centre of the data base parameter space. Nevertheless the statistical error can also be evaluated for real measurement data, giving a precise measure for the noise contribution in the reconstruction error.

The combined effect of the statistical and systematic error, the total reconstruction error, containing the effects of both the systematical and the statistical error can be estimated from

$$(\varepsilon_j^{rec})^2 = \frac{1}{N-1} \sum_{\alpha} (F_j(\vec{q}_\alpha+\vec{\varepsilon}_\alpha) - p_{j\alpha})^2, \tag{4.20}$$

where α runs from 1 to N. Approximately, $(\varepsilon_j^{rec})^2 \approx (\varepsilon_j^{sys})^2 + (\varepsilon_j^{stat})^2$.

If the spread of a parameter within the database is small, the error ε_j may also be small without predicting variations in the parameter correctly. Therefore the quantity ε_j/σ_j is considered a better indicator for the quality of parameter reconstruction than ε_j itself.

The error estimates (4.18) and (4.20) allow us to search for an optimal combination of basis functions that gives maximum reconstruction accuracy while being not too sensitive to measurement noise.

Reconstruction qualifier

The results obtained by FP are only valid for physical states within, or close to, the subspace of the total physical state space covered by the data base. If a physical state lies within this subspace, we know that the quality of the reconstruction can be estimated by means of the error measures defined in the previous section. A measure for the reliability of the results is therefore:

$$Q = \frac{1}{N_q} \sum_{i=1}^{N_q} \frac{\tilde{q}^2(i)}{\lambda_i + (\tilde{\varepsilon}_i^{meas})^2}, \tag{4.21}$$

where $\tilde{\varepsilon}_i^{meas}$ is the relative error that the transformed measurement i suffers due to the measurement errors $\{\tilde{\varepsilon}_i^{meas}, i=1,...,N_q\}$. Thus, Q is an indicator for "closeness" of a

measurement to the "centre" of the subspace (of the total parameter space) that is covered by the simulations. If $Q \approx 1$, the measurement is well represented within the database and the accuracy estimates made above apply. If $Q \gg 1$ ($Q > 4$) for a particular measurement, the results obtained by FP are extrapolations beyond the boundaries of the simulated subspace and no indication of the accuracy can be given. Such an observation can be ignored, or, if it is known that the measurements are not at fault, the data base can be extended to include the experimental situations not covered in the existing database, or, if it is known that one or more specific measurement signals are failing, these can be reconstructed by minimizing (4.21) while keeping the correct signals fixed.

4.2.4 Application to the RTP tokamak

4.2.4.1 Introduction

Tokamak physics

We shall illustrate the procedure of FP with an example from tokamak plasma physics. A tokamak plasma is a toroidally shaped ionized gas through which a large current flows in the toroidal (ϕ) direction, along the externally imposed toroidal magnetic field (the geometry is clarified in Fig. 4.1). The current produces a magnetic field in the poloidal (transverse) direction which balances the outward $-\nabla p$ pressure gradient force by an inward $\vec{j} \times \vec{B}$ force ($\vec{j}$ is the current density). When these forces are equal and opposite, the plasma is in equilibrium. Treating the plasma as a single-species ideally conducting fluid and assuming toroidal rotational invariance, the equations governing the equilibrium (the pressure balance supplemented with the Maxwell equations), can be written down in terms of the poloidal flux function ψ. The poloidal magnetic field is given by

$$\vec{B}_p = -\frac{1}{R}\nabla\psi \times \vec{e}_\phi, \tag{4.22}$$

where we have adopted the usual cylindrical coordinate system (R,Z,ϕ). The equilibrium equation can be written

$$\Delta^*\psi = \left[R\frac{\partial}{\partial R}\frac{1}{R}\frac{\partial}{\partial R} + \frac{\partial^2}{\partial Z^2}\right]\psi = -\mu_0 R j_\phi = -\mu_0 R^2 p' - FF', \tag{4.23}$$

where j_ϕ is the toroidal current density, $p(\psi)$ is the pressure, $F(\psi) = RB_\phi$ which is related to the poloidal current density and $'$ denotes $\partial/\partial\psi$. This is known as the Grad-Shafranov (GS) equation [Shaf-58]. It is a second-order differential equation with 2 source functions (p and F).

If the source functions and suitable boundary conditions are given, a single solution $\psi(R,Z)$ can be found by solving the equation. In an experimental situation, however, the source functions are not known *a priori*.

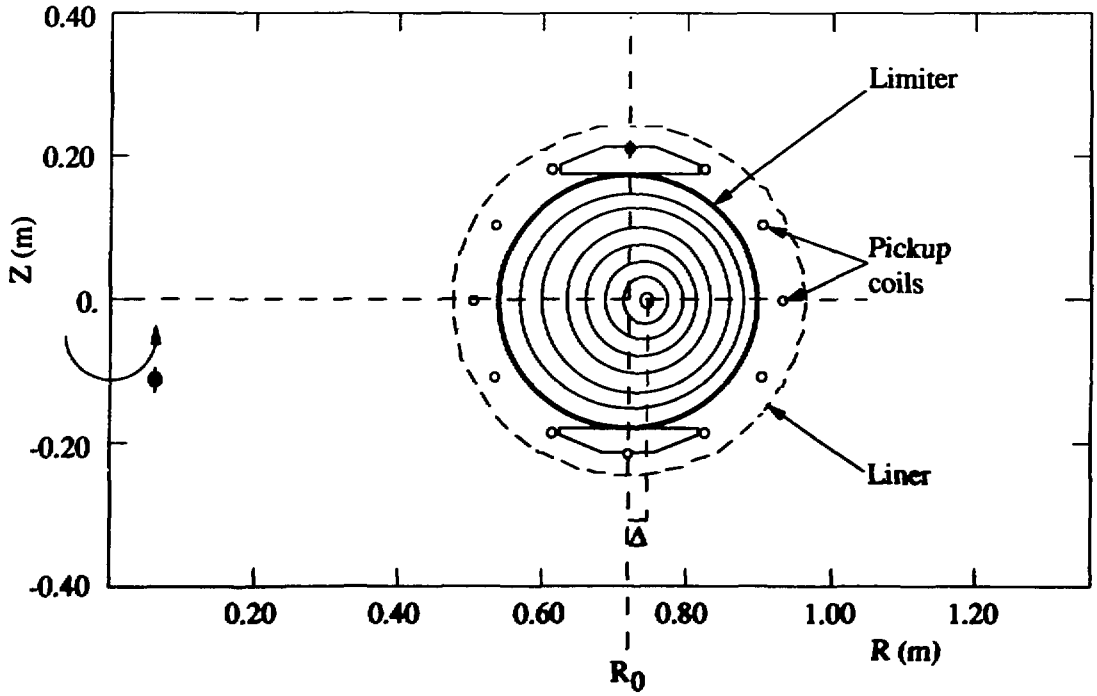

Fig. 4.1 Poloidal cross-section of the RTP tokamak.

RTP

The Rijnhuizen Tokamak Project (RTP) Tokamak is schematically shown in Fig. 4.1. The experimental data consist of 12 poloidal field measurements (made at the locations indicated by 'pick-up coils' in Fig. 4.1), 12 radial field measurements (made using wire loops attached to the liner) and a measurement of the toroidal field B_0, so $N_q = 25$. The physical parameters of interest are, e.g., the location of the plasma boundary or the current density at the plasma centre.

Given the kind of measurements available, solution of the GS equation is only possible by making restrictive assumptions with regard to the source functions in Eq. (4.23) (generally referred to as 'profiles'). Even then the solution procedure is time-consuming: it consists of

selecting the two profiles, solving the equilibrium, computing the corresponding magnetic data and iteratively adjusting the profiles and other parameters until a satisfactory reproduction of the real measurements is found. This procedure has to be carried out $O(100)$ times for a single experiment lasting 100 ms in order to get an indication of the time-development of the plasma, and several tens of experiments can be carried out each day. This leads to an intolerable burden on the computer system with traditional equilibrium solver programs. FP provides the means to make such analysis feasible.

4.2.4.2 Parametrization

In our example the reduced set of parameters $\{p_j, j \leq N_{id}\}$ used in identifying the equilibrium are the following. (1) I_p is the total current flowing through the plasma. (2) B_0 is the value of the toroidal field on the torus axis. (3,4) (R_{geo}, Z_{geo}) is the location of the geometrical centre of the plasma boundary in cylindrical coordinates. (5) a_{min} is the minor radius of the plasma. We have assumed the plasma to have a circular shape in a poloidal cross-section, and the flux surfaces are taken to be circular as well. The plasma column is assumed to have up-down symmetry with regard to the $Z = Z_{geo}$ plane. (6) δ is the 'Shafranov shift', i.e. the outward displacement of the magnetic axis with respect to R_{geo} ($\delta = \Delta/a_{min}$, where Δ is the Shafranov shift in m, see Fig. 4.1). δ is closely related to the central pressure. (7,8,9,10) The remaining quantities are profile parameters ($a_\Gamma, e_\Gamma, a_\Pi, e_\Pi$, explained below). Thus, $N_{id} = 10$.

The profiles are written down in a dimensionless form (unit profiles). The amplitude of the profiles is then given by the other parameters, and the unit profiles themselves only contain shape information. The unit profiles are chosen to be:

$$\Gamma(\psi) = (1 + a_\Gamma\psi + b_\Gamma\psi^2)^{e_\Gamma} \qquad (a_\Gamma + b_\Gamma = -1) \qquad (4.24a)$$

$$\Pi(\psi) = (1 + a_\Pi\psi + b_\Pi\psi^2)^{e_\Pi} \qquad (a_\Pi + b_\Pi = -1) \qquad (4.24b)$$

Here ψ is a normalized flux coordinate: $\psi = 0$ on axis and $\psi = 1$ at the plasma boundary. This choice of profile parametrization is motivated by the observation that measurements made on typical RTP discharges can be well reproduced by equilibria generated using this parametrization. The unit profiles Γ and Π, appearing in the HBT equilibrium solver [Goed-84], are related to the pressure derivative (p') and poloidal current (FF') profiles mentioned above through:

$$p'(\psi) = -\frac{AB\varepsilon B_0^2}{2\alpha^2}\Pi(\psi) \tag{4.25a}$$

$$FF'(\psi) = \frac{a_{min}^2 AB_0^2}{\alpha^2}\left[\Gamma(\psi) - \frac{B}{2\varepsilon}\Pi(\psi)\right] \tag{4.25b}$$

where A and B are eigenvalues of the GS equation and α is a dimensionless parameter measuring the total poloidal flux: $\alpha = a_{min}^2 B_0/\Phi_1$ (here Φ_1 is the unnormalized flux at the plasma boundary). A,B α and Φ_1 are determined by the MHD equilibrium code HBT .

Appendix 4.2.6.1 lists the values of the parameter ranges used for the creation of a database covering the RTP experiment (N = 1000 simulations). The central value was found by analyzing a typical discharge (R19900321.017) at t=50 ms. (in the so-called flat-top or steady-state phase). We defined a χ^2:

$$\chi^2 = \sum_{N_q} \frac{(q_i - q^{meas}_i)^2}{(\varepsilon^{meas}_i)^2} \tag{4.26}$$

Where ε^{meas}_i is the measurement error in the i^{th} measurement q^{meas}_i. We then computed an equilibrium with arbitrary choice of the parameter values and computed χ^2 from the simulated measurements q_i. We chose slightly different values of the parameters and iterated, thus minimizing χ^2 until it reached a value close to N_q, indicating good reproduction of the measurements. This equilibrium was taken as central value for the database. Note that the profiles used are fairly broad, reflecting the current type of plasmas produced in the experiment. In the near future, more peaked profiles might become more common. Should the need for such a change in parametrization occur, the reconstruction qualifier Q discussed in section 4.2.3.4 will automatically signal this and a new database using e.g. narrower profiles can be constructed.

4.2.4.3 Principal Component Analysis

We performed PCA exactly along the lines of section 4.2.3.2. First we determined the eigenvalues of the dispersion matrix of $\vec{q}$. Fig. 4.2 displays the eigenvalues vs. their index number graphically. As expected, they decay exponentially (cf. Eq. (4.9)). If we determine β_{coll} (Eq. (4.10)) from the exponential decay, ignoring the non-exponential tail for i > 20 that is due to finite computational accuracy, it follows: $\beta_{coll}(RTP) = 0.29$.

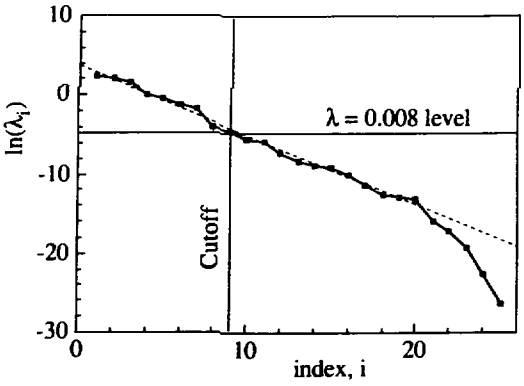

Fig. 4.2 Eigenvalues of the dispersion matrix of q versus the eigenvalue index number for the RTP database. The dashed line is the line $ln(\lambda) = 3.68 - 0.878\ i$.

The second step in PCA is the discarding of principal components. The relative measurement error in the magnetic measurements at RTP is approximately 3%. This suggests (cf. section 4.2.3.2) a cutoff at $\lambda = (3 \cdot 0.03)^2$ which we have marked in Fig. 4.2. Thus, keeping only 9 of the 25 principal components might already be sufficient to reproduce the plasma parameters within measuring accuracy. We will investigate this further in the next section.

4.2.4.4 Regression and error analysis

Regression based on PCA

Table 4.1 lists the error estimates defined in section 4.2.3.4 for the RTP database. We have performed the regression along the lines of section 4.2.3.3, using the polynomial regression model with Hermite polynomials.

Table 4.1: Plasma parameter reconstruction error analysis for RTP database $N_1 = 8$, $N_2 = 3$. (σ's and ε's normalized to the central value)

Parameter	I_p	R_{geo}	a_{min}	δ
Central value	100000.	0.721	0.133	0.0617
Spread, σ_j	0.22	0.048	0.13	0.13
ε_j^{sys}	0.0022	0.0039	0.062	0.12
ε_j^{stat}	0.0093	0.0019	0.014	0.011
ε_j^{rec}	0.0093	0.0043	0.064	0.12
$\varepsilon_j^{sys}/\sigma_j$ (%)	0.96	8.0	47.	93.
$\varepsilon_j^{stat}/\sigma_j$ (%)	4.2	4.0	11.	8.5
$\varepsilon_j^{rec}/\sigma_j$ (%)	4.2	8.9	48.	94.

Table 4.1 clearly demonstrates how some parameters are easily recovered from the magnetic data while others are hard to determine at all. The reconstruction of I_p (which can analytically be expressed as a simple sum over the poloidal field measurements) is dominated by the statistical error. The other parameters listed here have reconstruction errors that are dominated by the systematical error.

Of course, many more parameters than the ones listed in table 4.1 are available to describe the plasma state *p*. Tables like 4.1 can also be used to determine which plasma parameters can be determined most accurately from the available measurements and are therefore best suited for the purpose of giving a description of the plasma. In this manner we have found that of the two most common sets of moments used in describing the magnetic field outside the plasma, i.e. current and multipole moments [Mill-90], current moments are best by far.

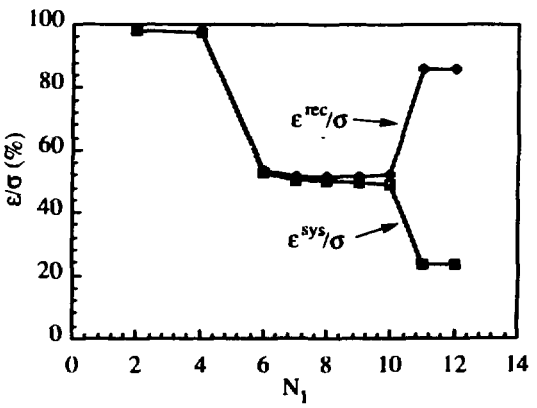

Fig. 4.3 Reconstruction error in a_{min} as a function of N_1.

The error estimates (4.18) and (4.20) allow us to search for an optimal combination of basis functions giving maximum reconstruction accuracy while being not too sensitive to measurement noise. The data in table 4.1 were compiled from a reconstruction that was already optimized. We shall now demonstrate how we came to this choice of basis functions.

While ε_j^{sys} decreases monotonically with the number of basis functions, ε_j^{stat} increases, leading to an optimum (i.e. minimum) in ε_j^{rec}. Taking too many basis functions deteriorates the regression results, because the higher-order basis functions are more sensitive to noise.

Figures 4.3, 4.4 and 4.5 illustrate the behaviour of ε_j^{sys} and ε_j^{rec} as a function of the amount of linear and quadratic basis functions (N_1 and N_2, respectively, see Eq. (4.8)). We have selected a_{min} and R_{geo} as illustrations of the procedure. From Fig. 4.2 we expect the reconstruction to be optimal at $N_1 = 9$ in Fig. 4.3. In fact, what we see is that the first 5 principal components already contain the essential information necessary for reconstruction

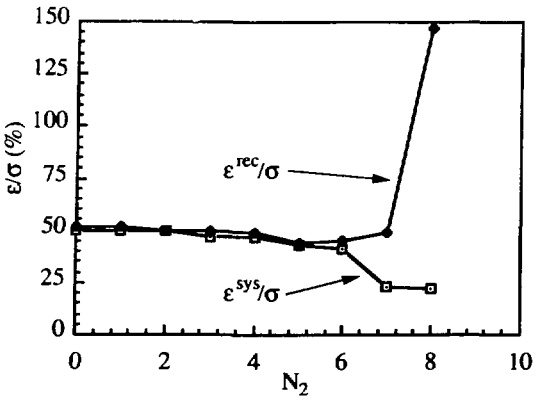

Fig. 4.4 Reconstruction error in a_{min} as a function of N_2, N_1 = 8.

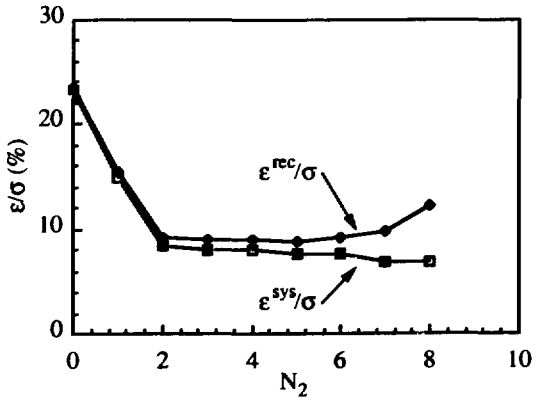

Fig. 4.5 Reconstruction error in R_{geo} as a function of N_2, N_1 = 8.

of a_{min}. The predicted minimum in ε_j^{rec} is fairly broad (from N_1 = 5 to 10), and taking N_1 anywhere in this range will not influence the reconstruction significantly. Note that taking N_1 = 11 (= N_{id}+1 !) or more leads to a significant reduction of ε_j^{sys} but unacceptable instability with respect to measurement noise. We selected N_1 = 8 on the basis of graphs like Fig. 4.3 for other parameters, keeping in mind that N_1 should be equal to N_{id}, approximately. Having selected N_1, we proceeded along similar lines for the selection on N_2 (Fig. 4.4). N_2 does not have a significant influence on the reconstruction of a_{min} as long as $N_2 \leq 6$, but it does on the reconstruction of R_{geo} (Fig. 4.5). Also, the computing time is a strong function of the N_n's (see Eq. (4.5)). This motivated us to select N_2 = 3.

Regression based on LR

We have analyzed the same RTP database with the Latent Root analysis method. We found that in order to keep between 6 and 8 principal components, the discriminatory levels γ and δ should be chosen $\gamma = \delta = 0.3$. The actual number of principal components kept is different for each plasma parameter, of course: e.g. accurate reconstruction of the plasma current I_p requires less principal components than any other plasma parameter. This is demonstrated by the listed number of principal components in table 4.2.

Also listed in table 4.2 is the reconstruction accuracy for each parameter. The numbers listed should be compared to those of table 4.1. The Latent Root method in the case studied here reduces the systematical error, while increasing the statistical error slightly. The total

reconstruction error ε_j^{rec} using LR is slightly better than the one using PCA. For most plasma parameters the difference is only slight, however, except for δ. LR has detected and removed a non-predictive principal component for this parameter.

Table 4.2: Plasma parameter reconstruction error analysis for RTP database using LR. N_1 is equal to the number of principal components kept: N_{prin}, and $N_2 = 6$. (σ's and ε's normalized to the central value)

Parameter	I_p	R_{geo}	a_{min}	δ
N_{prin}	6	7	7	7
Central value	100000.	0.721	0.133	0.0617
Spread, σ_j	0.22	0.048	0.13	0.13
ε_j^{sys}	0.0011	0.0036	0.052	0.085
ε_j^{stat}	0.0090	0.0022	0.031	0.035
ε_j^{rec}	0.0097	0.0043	0.064	0.098
$\varepsilon_j^{sys}/\sigma_j$ (%)	0.47	7.6	39.	66.
$\varepsilon_j^{stat}/\sigma_j$ (%)	4.0	4.6	23.	27.
$\varepsilon_j^{rec}/\sigma_j$ (%)	4.3	8.9	48.	76.

4.2.4.5 Results

Figures 4.6 through 4.9 show the time traces of some plasma parameters that were obtained from real measurements using FP, for RTP discharge R19900321.017.

Figure 4.6 shows the time trace of the plasma current. After initiation of the experiment, it rises quickly to 100 kA, to remain in the 'flat-top' phase for approximately 100 ms.

Figure 4.7a shows the time trace of

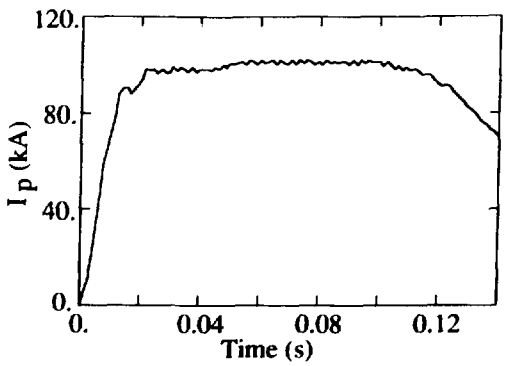

Fig. 4.6 Plasma current for discharge R19900321.017.

R_{geo}. Initially, there is a large oscillatory movement that is due to an imperfection in the plasma position control. The FP signal can be compared to the Δ_{hor} signal, which is simply the position of the weighted current centre with respect to the R = 0.72 (or central) position. This signal is displayed in Fig. 4.7b, and compares well to 4.7a.

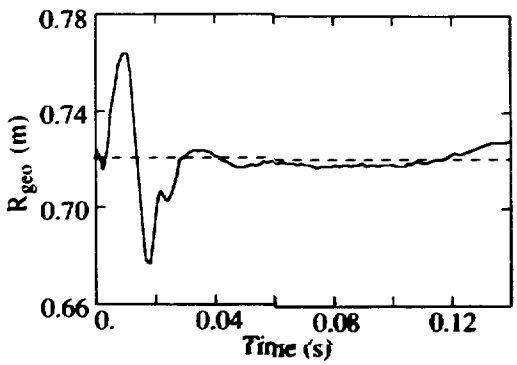

Fig. 4.7a Plasma position for discharge R19900321.017.

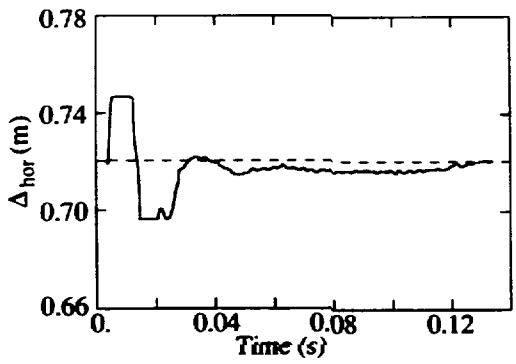

Fig. 4.7b Horizontal plasma position (traditional method) for discharge R19900321.017. Note that for t < 0.03 s the ADC signal exhibits saturation.

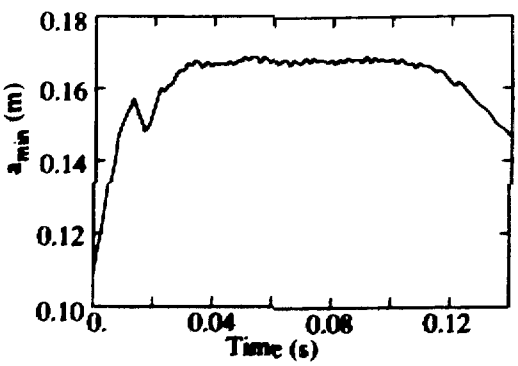

Fig. 4.8 Minor radius of plasma for discharge R19900321.017.

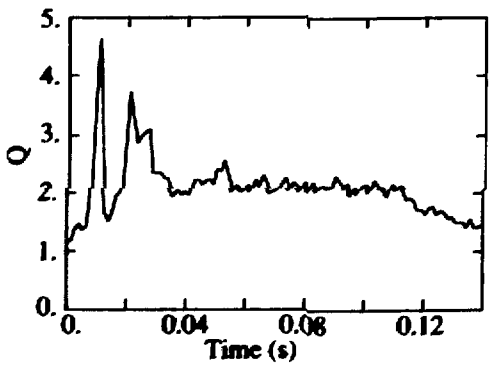

Fig. 4.9 Reconstruction qualifier for discharge R19900321.017.

Fig. 4.8 displays the time trace of the a_{min} signal. During the flat-top phase, it attains the maximum value (0.178 m) dictated by the circular limiter (Fig. 4.1) within measuring accuracy.

Fig. 4.9 displays the reconstruction qualifier Q. Apart from spikes at the beginning, it stays low (≈2) during the entire shot, indicating reliable reconstruction.

4.2.5 Summary and Conclusions

4.2.5.1 Principle and Advantages of Function Parametrization

Function Parametrization is a method to invert computer models that map physical parameters that describe the state of a physical system onto measurements. The method involves generating and storing a large number of well-chosen simulations and statistically analyzing these. The result is a mapping of the measurements onto the physical parameters that requires little computing time to evaluate. The major advantages of FP over other analysis methods are: it is quite general; it is fast, allowing real-time control of experiments; it allows a thorough error analysis (as was demonstrated in this paper); it can provide insight into the structure of the computer program used to model the experiment; it can be used to analyze sets of dissimilar measurements; it can be used to study the adequacy of certain new measurements for determination of specific physical parameters (even before the measuring equipment is built).

4.2.5.2 Power and Limitations of Function Parametrization

Generally, the computer model mapping the physical parameters onto the measurements reduces information content, i.e. the measurements do not represent full knowledge of the physical system, or, in other words, the mapping is essentially a projection. This necessarily means the inverse mapping cannot determine all physical parameters exactly. This problem can be circumvented by restricting the physical parameter space, i.e. by choosing a certain parametrization of the physical system that limits the solutions of the inverse problem to a certain class, provided knowledge is available to confidently make this restriction without excluding essential parts of the physical state space. Alternatively, one may decide to accept such ill-determinedness of some physical parameters as being inherent to the analysis of inadequate measurements.

On the other hand, the measurements generally also contain redundant information. As the inverse mapping method relies on regression analysis, large dimensionality of the measurement space and mutual (linear) dependencies between the measurements are undesirable. Two methods are suggested to reduce the dimensionality of the measuring space

without rejecting essential information: Principal Component Analysis (PCA) and Latent Root Analysis (LR).

PCA selects those linear combinations of the measurements that have maximum variance within the database. Generally, these will also have the highest predictive relevance. However, if the computer model is not very stable there may be combinations of the measurements that show a large variance over the data base but have little relevance to the physical parameters. Also, a specific parameter may be related to a subset of the measurements that show only small variance (rather than all measurements). In these cases Latent Root analysis may improve the solution of the model inversion problem, as it selects those combinations of the measurements that have highest correlation with specific physical parameters.

4.2.5.3 Application to Tokamak Physics: RTP

The practical example of Tokamak equilibrium reconstruction presented in this paper demonstrates that FP is capable of making a fast, accurate and reliable computation of plasma parameters from the magnetic measurements presently available at the RTP experiment. As soon as other relevant measurements become available (e.g. polarimetry or SXR measurements), these can also be incorporated in the analysis to help determine the equilibrium more accurately, and in more detail. FP has already been successfully applied to polarimetric data at the TEXTOR tokamak [Mill-91a], and this is anticipated for RTP as well (in combination with magnetic data). Also, FP is fast enough to make it a likely candidate for real-time plasma control and feedback.

4.2.5.4 Conclusions

The method of Function Parametrization provides a means to carry out fast data analysis of measurements done on physical systems modelled with large and complex computer codes. The analysis can be carried out using only minimal computing time. This is achieved by concentrating the main computational effort before the beginning of the physical experiment.

The method may be of use in other contexts as well: it may relieve any repetitive running of large computer programs, or at least give a first approximation of the solutions that such programs attempt to find, thus reducing the searching effort. Its use is also indicated with expert systems.

4.2.6 Appendix

4.2.6.1 Database generation: Method of parameter selection

Database generation is carried out by selecting the N_{id} independent parameters p_j, j=1,...,N_{id} randomly from a range R_j: $p_j^{min} \le p_j \le p_j^{max}$, computing the remaining plasma parameters and the measurements, and repeating this N times. The random selection is made using a truncated normal (i.e. Gaussian) probability distribution function $f_j(p_j)$ with its maximum at p_j^{prim} (where $p_j^{min} \le p_j^{prim} \le p_j^{max}$) and width σ_j (Fig. 4.10). The choice of a Gaussian-type probability distribution function is not essential to the method. The upper and lower boundaries only serve to prevent extremely unlikely states of the plasma to be included in the database. The value of p_j^{prim} is inspired by expectations about the most likely experimental situation as indicated above, and likewise the choice of σ_j is inspired by the expected spread. This procedure will cause the regression (see below) to be most accurate near the most likely experimental situation.

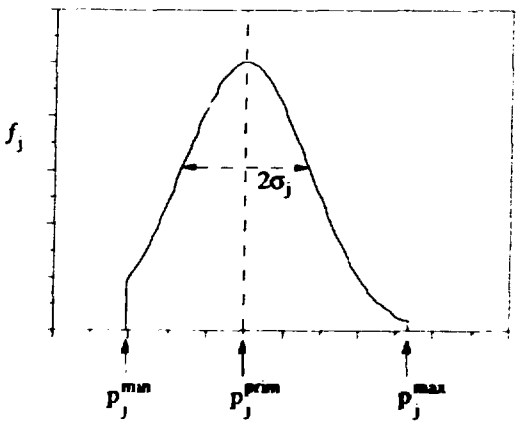

Fig. 4.10 Truncated Gaussian probability distribution function.

4.2.6.2 Database generation (RTP)

Table 4.3: Plasma state parameter distribution settings for database generation

Parameter	Lower bound	Central value	Upper bound	Spread, σ
I_p	10000.	100000.	150000.	30000.
B_0	1.0	2.03	2.3	0.2
R_{geo}	0.65	0.72	0.80	0.04
Z_{geo}	–0.05	0.	0.05	0.02
a_{min}	0.09	0.173	0.178	0.04
δ	0.04	0.0555	0.1	0.01
a_Γ	–1.2	–1.0	–0.8	0.1
e_Γ	0.2	0.7	1.2	0.2
a_Π	–1.2	–1.0	–0.8	0.1
e_Π	0.1	0.3	0.8	0.15

4.2.6.3 Table of notation

p	state of a physical system
$\vec{p}$	physical parameter vector $(p_1,...,p_{Np})$
$\vec{q}$	measurement vector $(q_1,...,q_{Nq})$
$\vec{M}$	computer model $\vec{q} = \vec{M}(\vec{p})$
$\vec{F}$	inverse mapping $\vec{p} = \vec{F}(\vec{q}) + \vec{\epsilon}$
N	number of simulations = size of database ($\alpha = 1,...,N$)
N_p	number of physical parameters ($j = 1,...,N_p$)
N_q	number of measurements ($i = 1,...,N_q$)
N_{id}	number of physical parameters sufficient to identify a physical state
$\langle x \rangle_j$	average of x_j
$\sigma_j(x)$	standard deviation of x_j
$\bar{x}$	normalized vector $\vec{x}$ (i.e. having zero mean and unit standard deviation)
$\tilde{x}$	'transformed' vector $\vec{x}$ (having linearly independent components in the database)
N_s	number of significant variables
$\phi_n(x)$	basis function of n^{th} order in x
c_{ij}	regression coefficient
N_n	number of 'transformed' vector components used in constructing basis functions of n^{th} order

4.2.7 Acknowledgements

The authors would like to express their gratitude to Bas Braams and Chris Schüller for fruitful discussions on the subject of Function Parametrization. A short collaboration with Patrick McCarthy and Karl Lackner at ASDEX has been inspiring and we are endebted to them for providing much insight into the matter. The idea of Latent Root Analysis and some of the algorithms used in the present work are due to Patrick McCarthy. This work was performed under the Euratom-FOM Association agreement with financial support from NWO and Euratom.

4.3 Application of Function Parametrization to the Analysis of Polarimetry and Interferometry data at TEXTOR

B.Ph. VAN MILLIGEN, H. SOLTWISCH[1], N.J. LOPES CARDOZO

FOM Instituut voor Plasma Fysica "Rijnhuizen"
PO Box 1207, 3430 BE Nieuwegein, The Netherlands

[1] Institut für Plasmaphysik, Forschungszentrum Jülich,
D-W 5170 Jülich, Germany

4.3.1 Abstract

Function Parametrization provides a way to do complex data analysis in a fast and reliable manner that allows inter-shot analysis. The method has been used to analyze polarimetry and interferometry data at TEXTOR with the purpose of obtaining spatial distributions of the electron density and toroidal plasma current. A standard TEXTOR discharge is investigated, allowing comparison of the results with results obtained by conventional methods of data analysis. Agreement between the two is generally good. For the central safety factor we determine a value of $q_0 = 0.8 \pm 0.1$ in accordance with previous calculations. The new method allows easy incorporation of additional data.

4.3.2 Introduction

In a tokamak, the total toroidal plasma current can be programmed, but it is not possible to control the distribution of the current over the plasma column. In fact, it is not even possible as yet to make direct, accurate measurements of the current density profile. The experimental data available are rather indirect, such as the magnetic fields outside the plasma (which give very little information on the current density in the plasma centre, especially for near-circular plasma cross-sections) or the Faraday rotation a polarised laser beam experiences when passing through the plasma. To construct the current distribution from those measurements, it is in general necessary to parametrize the plasma state (i.e. the profiles of density and current, or the MHD equilibrium) and to simulate the measurements corresponding to that plasma state. Thus the task is to find a set of parameters for which the simulated measurements match the experimental values within the measuring accuracy.

This type of problem is very well suited to be tackled with a technique known as Function Parametrization (FP). In general terms, this method provides a direct mapping of the observables onto the state parameters of a physical system. For the problem at hand, this means that the current density profile is parametrized, and the profile parameters are expressed in terms of the magnetic fields or Faraday rotation measurements. To achieve this, a database is generated containing a large number of MHD equilibria. The equilibria are chosen in such a way that all normal plasma conditions are covered by the variation in the database. Along with each equilibrium, a set of simulated measurements is computed and stored. The database is subjected to a statistical analysis procedure that results in a direct mapping of the measurements onto the physical parameters. This mapping is a set of simple functions which express the plasma parameters in terms of the observables. These functions can be evaluated for experimental data using a minimum of CPU time. Thus, the advantages of FP are twofold:

- once set up, the analysis is very fast,
- the analysis is internally consistent, i.e. one always finds results within the class of parametrized MHD equilibria.

In this paper we describe the application of FP to the analysis of polarimeter data at TEXTOR. As has been shown previously, the combination of polarimetric and interferometric measurements can be used to reconstruct the current density profile. For this purpose an interpretation method has been developed that assumes a flux surface geometry of shifted circles and iteratively adjusts the current density profile until the simulated measurements match the experimental values [Solt-86b]. We shall refer to this method as Method I. Other iterative

techniques for the interpretation of polarimetry and interferometry data are described in [ORou-88; Hoff-88]. In this paper we compare the results obtained with Method I and Function Parametrization. Particular attention is paid to the value of the safety-factor in the centre of the discharge.

4.3.3 Interferometry and polarimetry at TEXTOR

At TEXTOR, the plasma is intersected by nine linearly polarized Far Infrared laser beams, vertically aligned in a poloidal cross-section (Fig. 4.11; details on the experimental setup may be found in Refs. [Solt-86a, Solt-86b]).

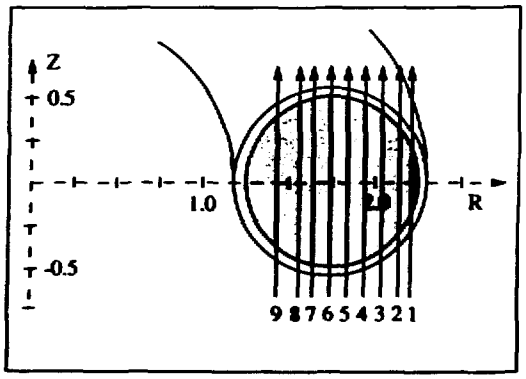

Fig. 4.11 Schematic layout of the TEXTOR polarimetry / interferometry setup.

To good approximation, the laser light experiences a phase shift $\Delta\phi$ and a polarization rotation angle α upon passage through the plasma given by [Solt-86b]:

Interferometry:

$$\Delta\phi = c_1 \lambda \int_{-Z}^{Z} n_e \, dZ \qquad (c_1 = 2.818 \cdot 10^{-15} \text{ m}) \qquad (4.27a)$$

Polarimetry:

$$\alpha = c_2 \lambda^2 \int_{-Z}^{Z} n_e \, B_{p//} \, dZ \qquad (c_2 = 2.615 \cdot 10^{-13} \text{ T}^{-1}) \qquad (4.27b)$$

Here the usual cylindrical coordinate system (R,Z,ϕ) is adopted; n_e is the electron density and $B_{p//}$ is the component of the poloidal magnetic field parallel to the probing beam; all quantities are expressed in S.I. units with $\Delta\phi$ and α in radians. The probing beam wavelength is $\lambda = 337 \cdot 10^{-6}$ m. The validity of the assumptions underlying these approximate formulas has been discussed in Ref. [Solt-80].

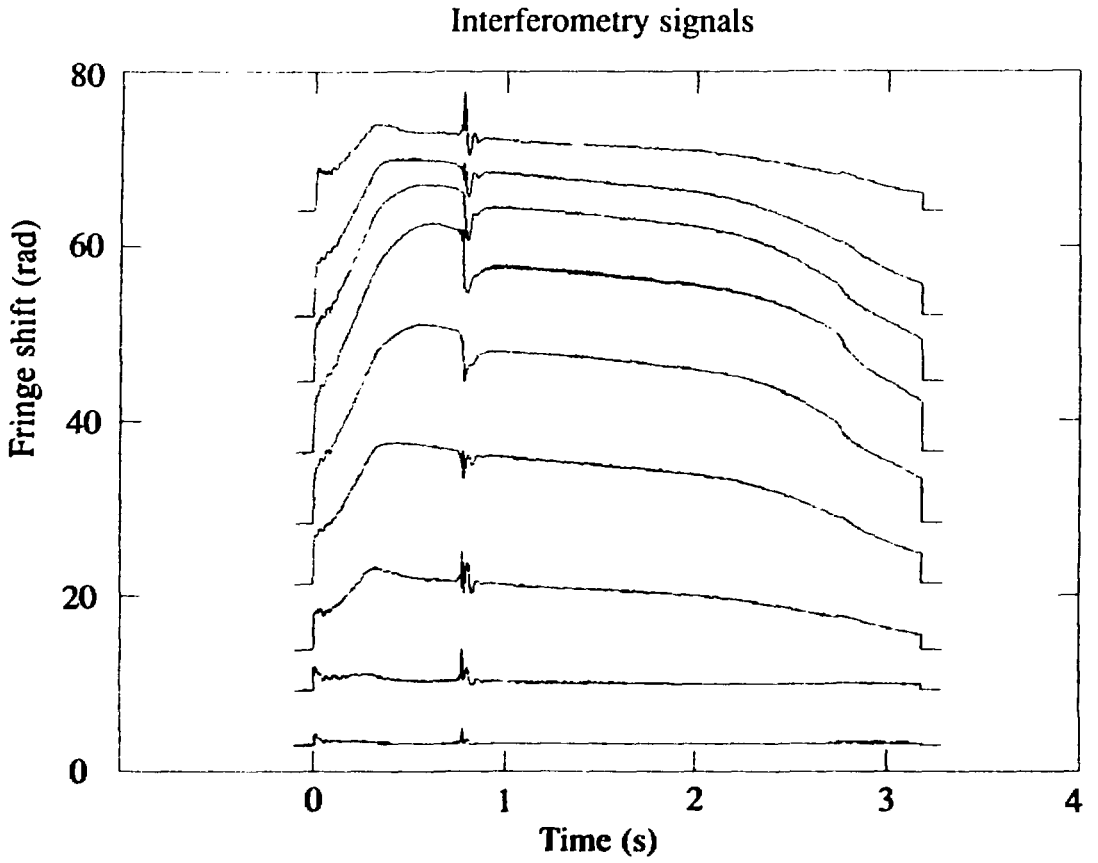

Fig. 4.12a The interferometry signals for TEXTOR discharge #14214, with arbitrary offset.

The interferometry and polarimetry error levels quoted are: $\varepsilon_{int} = 0.126$ rad and $\varepsilon_{pol} = 0.0026$ rad (these absolute error levels correspond to approximately 0.25% and 1.5% relative error levels, respectively, for typical signal values) [Solt-86a]. Typical data are shown in Fig. 4.12.

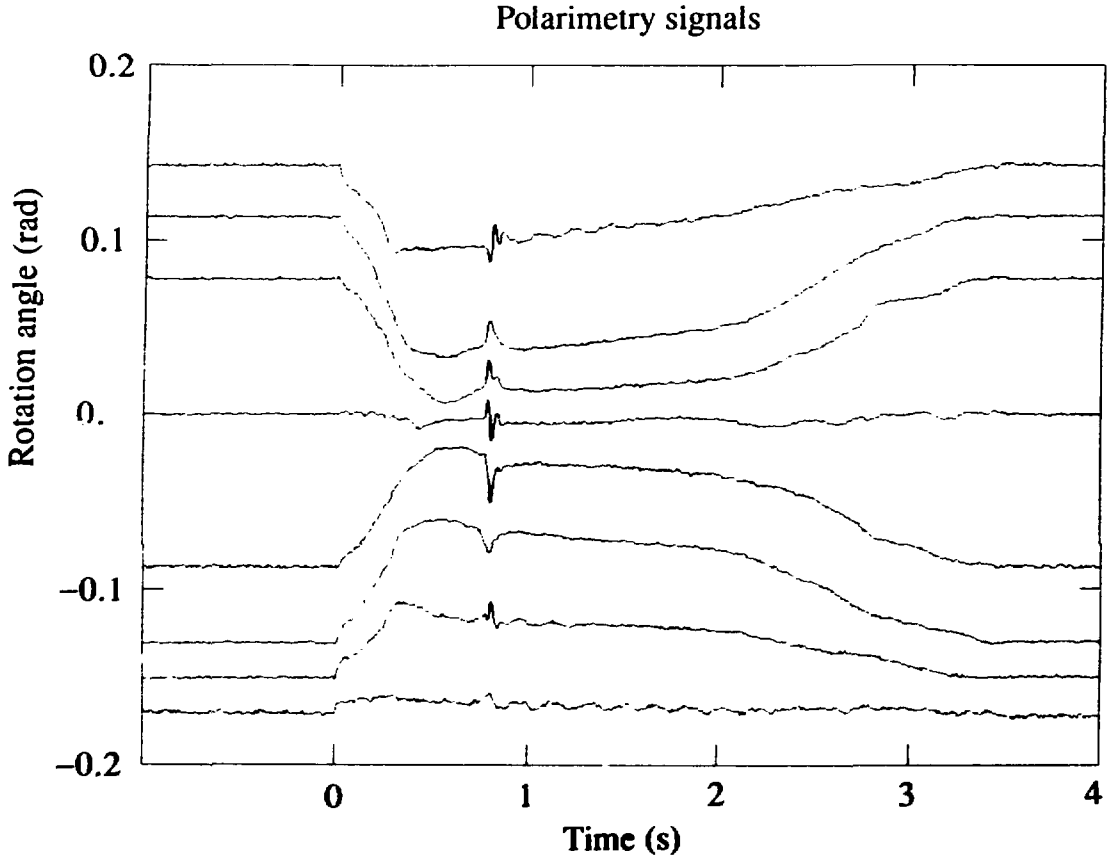

Fig. 4.12b The polarimetry signals for TEXTOR discharge #14214, with arbitrary offset.

4.3.4 Data analysis

4.3.4.1 Conventional method

The analysis procedure presently in use at TEXTOR (Method I) has been described in detail in Refs. [Solt-86a, Solt-86b]. The main steps may be summarized as follows: (i) expand the experimental data $\Delta\phi(R_i)$ and $\alpha(R_i)$ (with $i = 1,...,9$ representing the installed probing beams) by suitable spline-interpolations into full phase shift and Faraday rotation profiles along the major radius; (ii) divide the plasma cross-section into a large number of ring zones ($N \gtrsim 100$)

corresponding to a set of horizontally shifted circular flux surfaces in rough agreement with numerical equilibrium calculations; (iii) assume both the electron density n_e and the flux change $d\Psi/d\rho$ to be constant in a given ring zone and approximate the integrals in equations (4.27a) and (4.27b) by finite sums with the number of terms equal to the number of ring zones intersected by a virtual probing chord; (iv) invert the resulting systems of linear equations to obtain a first approximation for $n_e(\rho)$ and $d\Psi/d\rho$; (v) impose certain constraints (such as the flux change on the plasma surface being in accordance with the total current) and calculate 'theoretical' phase shift and Faraday rotation data for the probing beam positions R_i; (vi) vary the flux surface geometry and iterate the procedure until the 'theoretical' signals match all experimental ones as closely as possible.

Owing to the fact that both $\Delta\phi$ and α vanish at chords near the plasma boundary, no accurate information can be obtained from the edge region.

Besides being a time-consuming process, this method of data analysis derives the shift of the flux surfaces only from measured asymmetries in the $\Delta\phi(R)$- and $\alpha(R)$- profiles and not from detailed equilibrium calculations. It should be noted, however, that occasional cross-checks with an extensive MHD equilibrium code have confirmed both the underlying assumption of circular flux surfaces as well as the resulting eccentricity.

4.3.4.2 Function Parametrization

The method of Function Parametrization takes quite a different approach. The state *p* of the plasma is modelled in terms of a finite set of parameters $\{p_j, j=1,...,N_p\}$, where N_p is the number of physical parameters involved in the model. Below we shall investigate the actual parametrization with which standard TEXTOR discharges are represented.

Once the parametrization is fixed, the parameters p_j are varied randomly within certain ranges. These parameter ranges are chosen large enough to cover most plasma states occurring in real experiments. For every parameter set an MHD equilibrium is computed along with simulated measurements $\{q_i, i=1,...,N_q\}$. For every simulated equilibrium the $\{q_i, p_j\}$ are stored in a database. At this point we remark that $\{p_j\}$ includes both the minimal set of plasma state parameters that are sufficient to identify an equilibrium, as well as a number of derived parameters that are of physical interest but are dependent on the state parameters.

The database is subjected to a statistical analysis procedure that results in a direct mapping of the measurements onto the physical parameters, $\vec{p} = \vec{F}(\vec{q}) + \vec{\varepsilon}$, where $|\vec{\varepsilon}|$ is small. In the following we very briefly summarize the method. A more detailed account is given in [Solt-80].

The measurement vector $\vec{q}$ is normalized: $\bar{q}_i = (q_i - \langle q_i \rangle)/\sigma_i$, where $\langle q_i \rangle$ is the average value of q_i in the database and σ_i its spread. Then , the dispersion matrix D is computed according to

$$D_{ij} = \frac{1}{N-1} \sum_{N} \bar{q}_i \bar{q}_j,$$

where N is the number of simulations made. The eigenvalues and eigenvectors of D are computed: $D \cdot \vec{e}_j = \lambda_j \vec{e}_j$, where $\lambda_1 \geq \lambda_2 \geq ... \geq \lambda_{Nq} \geq 0$ and $|\vec{e}_j| = 1$. We define 'transformed' variables

$$\tilde{q}_i = \vec{e}_i \cdot \bar{q} \qquad (i=1,...,N_q)$$

The variables $\tilde{q}_i$ are linear combinations of the measurements with standard deviation $\sqrt{\lambda_i}$. They are uncorrelated within the database. The $\tilde{q}_i$ are used in a regression: $p_j = f_j(\tilde{q}_1, \tilde{q}_2, ..., \tilde{q}_{Nq}) + \varepsilon_j$. We take f_j to be a Hermite polynomial of order 2. In order to reduce the dimensionality of the fitting problem we discard those $\tilde{q}_i$ that have $\lambda_i < (3\varepsilon)^2$, where ε is the relative measurement error. The latter procedure is known as principal component analysis. The result of the regression is a mapping of measurements onto physical parameters, $\vec{p} = \vec{F}(\vec{q})$.

MHD equilibrium model

MHD equilibrium is described by the Grad-Shafranov (GS) equation:

$$\Delta^* \Psi = -\mu_0 R j_\phi = -\mu_0 R^2 p' - FF' \qquad (4.28)$$

where Ψ is the poloidal flux and the prime denotes $\partial/\partial\Psi$; $j_\phi(R,Z)$ is the toroidal current distribution (j_ϕ=0 outside the plasma boundary $\partial\Omega$). $p(\Psi)$ is the pressure profile (not to be confused with the physical parameter vector $\vec{p}$) and $F(\Psi)$ the poloidal current profile: $F(\Psi) = RB_\phi$.

The plasma equilibrium is computed by means of a fixed boundary ideal MHD equilibrium code: HBT [Goed-84]. The code has been extended to perform polarimetry

simulations. In this computer model, a state of the plasma p is identified by the following set of quantities:

1) Main plasma parameters:
   I_p (plasma current) and B_0 (toroidal magnetic field on torus axis)
2) Flux surface geometry parameters specifying the location of the magnetic axis and parameters specifying the shape of the plasma boundary
3) Profile parameters specifying the equilibrium profiles $p'(\Psi)$, $FF'(\Psi)$
4) Electron density parameters specifying the electron density n_e

The first objective of this investigation is a comparison of the results of FP with those of Method I. Therefore we choose the parametrization of the various quantities to match the assumptions underlying Method I as closely as possible. Thus, with regard to 2) we use circular flux surfaces that exhibit horizontal but no vertical displacement. With regard to 4) we set $n_e = n_e(\Psi)$. Note that n_e does not appear in the Grad-Shafranov equation, so that, strictly speaking, it can be any function of (R,Z). However, in ohmically heated discharges the assumption that n_e is a flux quantity is closely satisfied and it conforms with Method I.

With regard to the profiles (3,4) we make the following choice which allows for a wide variety of (non-hollow) profiles:

$$\Gamma(\psi) = (1 + a_\Gamma\psi + b_\Gamma\psi^2)^{e_\Gamma} \qquad (a_\Gamma + b_\Gamma = -1) \tag{4.29a}$$

$$\Pi(\psi) = (1 + a_\Pi\psi + b_\Pi\psi^2)^{e_\Pi} \qquad (a_\Pi + b_\Pi = -1) \tag{4.29b}$$

$$n_e(\psi) = n_{e0} \qquad (1 + a_n\psi + b_n\psi^2)^{e_n} \qquad (a_n + b_n = -1) \tag{4.29c}$$

Here ψ is a normalized flux coordinate: $\psi = 0$ on axis and $\psi = 1$ at the plasma boundary. The unit profiles Γ and Π that appear in the HBT code are related to the more familiar pressure derivative (p') and poloidal current (FF') profiles through:

$$\Gamma(\psi) = -\frac{\alpha^2}{A\varepsilon^2 B_0^2}\left[p'(\psi) + \frac{\varepsilon^2}{a_{min}^2} FF'(\psi)\right], \tag{4.30a}$$

$$\Pi(\psi) = -\frac{2\alpha^2}{AB\varepsilon B_0^2} p'(\psi) \tag{4.30b}$$

where A and B are eigenvalues of the GS equation and α is a dimensionless parameter measuring the total poloidal flux: $\alpha = a_{min}^2 B_0/\Phi_1$ (here Φ_1 is the unnormalized flux at the plasma boundary). A,B and α are determined by the MHD equilibrium code HBT [Goed-84].

The electron density profile (4.29c) is such that it has a continuous first derivative at the magnetic axis.

Summarizing, the plasma state *p* is modelled with 9 parameters using these parametrizations of the profiles :

2 parameters for global plasma definition: I_p, B_0

3 parameters for the plasma geometry definition:

R_{geo} (the geometrical centre of the plasma boundary),

a_{min} (the minor radius of the plasma boundary) and

$\delta = (R_{mag}-R_{geo})/a_{min}$ (the dimensionless Shafranov shift of the magnetic axis)

4 parameters for equilibrium profile definition: a_Γ, e_Γ, a_Π, e_Π

In addition, the electron density profile is modelled with 3 parameters: n_{e0}, a_n and e_n.

Data base generation

To get an indication whether the parametrization chosen in the previous section is sufficient to describe real data, interferometry and polarimetry signals of a prototypical TEXTOR shot (# 14214) were compared to data simulated by the equilibrium program HBT. The signals were taken at time t = 1.33 s, when the plasma was in steady-state. The plasma state parameters were adjusted until satisfactory agreement with the measurements was obtained. We found that the Γ– and Π–profiles need the freedom of a_Γ, a_Π, e_Γ and e_Π in order to reproduce the data within the measuring accuracy.

Having found a satisfactory reproduction of the measurements for a prototypical discharge, a database of equilibria was created by varying the plasma state parameters around this typical state. Table 4.4 lists the central values and the bounds chosen for each parameter.

Table 4.4: Plasma state parameter range settings for database generation

Parameter	Lower bound	Central value	Upper bound	Spread, σ
I_p	100000.	300000.	500000.	100000.
B_0	1.7	2.02	2.3	0.1
R_{geo}	1.67	1.72	1.80	0.04
a_{min}	0.35	0.48	0.53	0.03
δ	0.05	0.08	0.15	0.02
a_Γ	−1.4	−1.0	−0.7	0.2
e_Γ	1.5	2.2	2.5	0.2
a_Π	−1.4	−1.0	−0.7	0.2
e_Π	1.5	2.2	2.5	0.2
$n_{e0}/(10^{19})$	0.5	4.0	8.0	3.0
a_n	−0.9	−0.1	0.	0.2
e_n	0.5	1.4	2.5	0.5

The MHD equilibrium code HBT was run for 600 randomly chosen plasma state parameter values which were selected from Gaussian probability distributions centred around the 'central value' with a spread σ. The probability distribution functions were truncated at the 'lower bound' and 'upper bound' values to prevent extremely unlikely equilibria from being generated.

Actually, the interferometry and polarimetry measurement simulations are not directly computed by HBT because the electron density profile does not appear in the MHD equilibrium equation. Rather, the database contains enough information to be able to reconstruct the flux and magnetic fields along the polarimetry chords. The statistical analysis program (FP) then randomly selects electron density profile parameters and computes the polarimetry and interferometry data. The measurements simulated are: I_p, B_0, 9 polarimetry channels and 9 interferometry channels. These observable quantities are mapped onto several interesting plasma parameters by means of the statistical analysis procedure outlined before.

Error and reliability analysis

The reliability and sensitivity to measurement noise of the mapping mentioned above was studied. The systematical error introduced by the mapping can be estimated by computing the plasma parameters from the simulated data in the database using the mapping ($\vec{F}$) and comparing them to the stored values p_j. The systematic reconstruction error is defined as

$$(\varepsilon_j^{sys})^2 = \frac{1}{N-1} \sum_{\alpha} (F_j(\vec{q}_\alpha) - p_{j\alpha})^2, \tag{4.31}$$

where α runs over all N simulations. ε_j^{sys} is the average systematical error over the data base of the j^{th} parameter.

The statistical error in the computation of p_j can be estimated for each equilibrium separately by

$$(\varepsilon_j^{stat})^2 = \frac{1}{N_{stat}-1} \sum_{\beta} (F_j(\vec{q}+\vec{\varepsilon}_\beta) - F_j(\vec{q}))^2, \tag{4.32}$$

where β runs from 1 to N_{stat} (chosen arbitrarily but not too small) and $\vec{\varepsilon}_\beta$ is a vector of random variables. The standard deviation of the i^{th} component of $\vec{\varepsilon}_\beta$, $\sigma(\varepsilon_{i\beta})$, is equal to the measurement error in the i^{th} measurement (see section 4.3.3). ε_j^{stat} is a function of $\vec{q}$ and therefore variable over the data base. In table 4.5, ε_j^{stat} is computed at the centre of the data base parameter space.

The combined effect of the statistical and systematic error, the total reconstruction error, containing the effects of both the systematical and the statistical error can be estimated from

$$(\varepsilon_j^{rec})^2 = \frac{1}{N-1} \sum_{\alpha} (F_j(\vec{q}_\alpha+\vec{\varepsilon}_\alpha) - p_{j\alpha})^2, \tag{4.33}$$

where α runs from 1 to N. Approximately, $(\varepsilon_j^{rec})^2 \approx (\varepsilon_j^{sys})^2 + (\varepsilon_j^{stat})^2$.

If the spread of a parameter within the database is small, the error ε_j may also be small without predicting variations in the parameter correctly. Therefore the quantity ε_j/σ is considered a better indicator for the quality of parameter reconstruction than ε_j itself.

Table 4.5: Perturbation analysis; reliability test of inverse mapping

	I_p (A)	R_{mag} (m)	a_{min} (m)	δ	$n_{e0}/(10^{19})$	q_0
Central value	309000.	1.73	0.472	0.0909	4.01	0.837
Spread, σ_j	76400.	0.031	0.0275	0.0142	1.92	0.25
ε_j^{sys}		0.00718	0.0160	0.00971	0.124	0.0766
ε_j^{stat}		0.00221	0.0205	0.0133	0.218	0.0439
ε_j^{rec}		0.00784	0.0271	0.0171	0.263	0.0960
$\varepsilon_j^{sys}/\sigma_j$ (%)		22.8	58.0	68.4	6.28	29.6
$\varepsilon_j^{stat}/\sigma_j$ (%)		7.12	74.5	93.7	11.4	17.6
$\varepsilon_j^{rec}/\sigma_j$ (%)		24.9	98.4	120.	13.4	37.0

In table 4.5, the result of this error analysis is presented for some important plasma parameters. The plasma current is measured directly. It is observed that the approximate relationship $(\varepsilon_j^{rec})^2 \approx (\varepsilon_j^{sys})^2 + (\varepsilon_j^{stat})^2$ holds for the parameters not measured directly. Quantities related to the outer plasma regions such as a_{min} are indeterminate ($\varepsilon_j^{rec}/\sigma_j \approx 100\%$), as can be expected from this type of measurement (see section 4.3.4.1). Use of magnetic diagnostics should improve the latter. Likewise, due to the fact that $\delta = (R_{mag} - R_{geo})/a_{min}$, δ is less accurate than a_{min}. However, the location of the magnetic axis, R_{mag}, can be determined with an accuracy of 0.8 cm; n_{e0} with $2.6 \cdot 10^{18}$ m^{-3}; and q_0 with 0.1.

The error analysis presented above is based on the measurement error levels mentioned in section 4.3.3. These error levels are maximum estimates. Actual measurement error levels can be slightly smaller and can be estimated from the zero level signals of the interferometry and polarimetry detectors before the start of the discharge.

The results obtained by FP are only valid for plasma conditions within, or close to, the subspace of the total plasma state space covered by the data base. If a plasma state lies within this subspace, we know that the quality of the reconstruction can be estimated by tables such as table 4.5. A measure for the reliability of the results is therefore:

$$Q = \frac{1}{N_q} \sum_{i=1}^{N_q} \frac{\tilde{q}_i^2}{\lambda_i + \tilde{\varepsilon}_i^2},$$

where N_q is the number of measurements involved, $\tilde{q}_i$ is the value of the transformed measurement i (see section 4.3.4.2), λ_i is the i^{th} eigenvalue of the measurement dispersion matrix (i.e. the variance of the i^{th} transformed measurement in the database), and $\tilde{\varepsilon}_i$ is the error that the transformed measurement $\tilde{q}_i$ suffers due to measurement errors. Thus, Q is an indicator for 'closeness' of a measurement to the 'centre' of the subspace (of the total parameter space) that is covered by the simulations. If $Q \lesssim 1$, the measurement is well represented within the database and the accuracy estimates made above apply. If $Q > 4$, the results obtained by FP are extrapolations beyond the boundaries of the simulated subspace and no indication of the accuracy can be given.

4.3.5 Application to TEXTOR data and comparison to Method I

In order to test the validity of the Function Parametrization method, we have analyzed the temporal evolution of TEXTOR shot # 14214. From the large array of plasma parameters we have selected the quantities R_{geo}, R_{mag}, n_{e0} and q_0 as being indicative of the possibilities of this reconstruction technique.

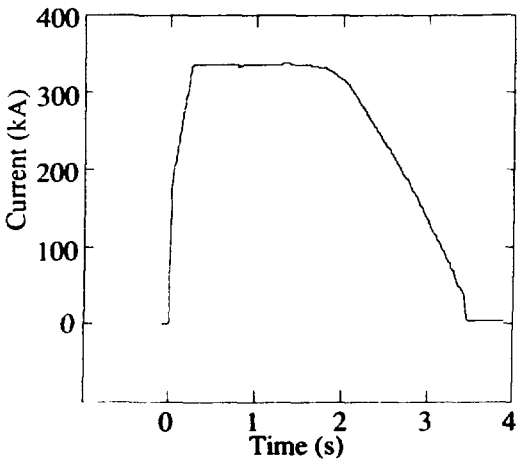

Fig. 4.13a The plasma current vs. time for TEXTOR discharge # 14214.

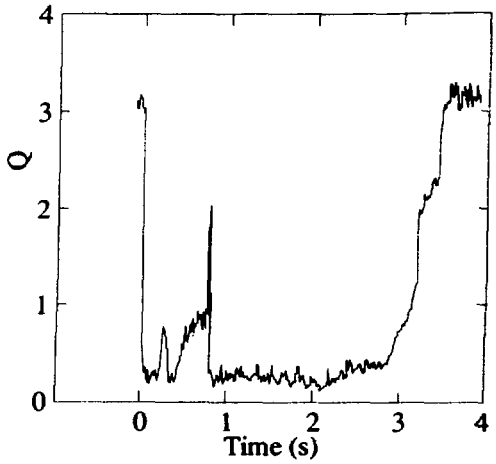

Fig. 4.13b The FP reconstruction quality parameter Q for TEXTOR discharge # 14214.

Figure 4.13a shows the time trace of the plasma current. There is a non-destructive disruption at t = 0.79 s, which changes the discharge characteristics from a non-sawtoothing plasma of relatively high metal content to a cleaner sawtoothing discharge. Figure 4.13b shows the FP reconstruction quality parameter Q. The reconstruction is valid during the entire shot, except at the beginning ($t \leq 0.03$ s) and at the end ($t \geq 3$ s). This is mainly due to the current ramp that is likely to cause profile deformations not covered by the chosen parametrization (see section 4.3.4.2).

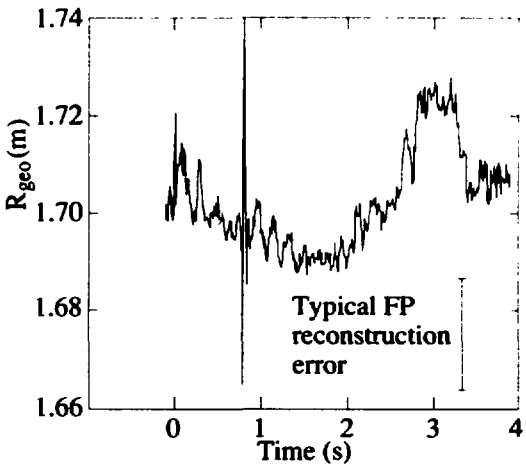

Fig. 4.14a Time trace of R_{geo}, the location of the outer flux surface. The FP error bar shown is ε^{rec}.

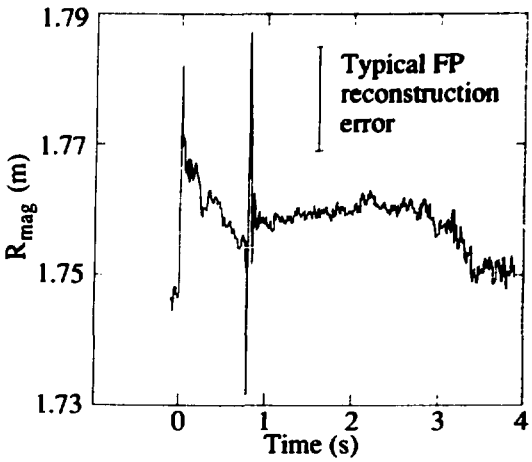

Fig. 4.14b Time trace of R_{mag}, the location of the magnetic axis. The FP error bar shown is ε^{rec}.

Figures 4.14a and b show the time traces of R_{geo} and R_{mag} as computed using FP. The plasma performs a fast inward movement during the disruption. This behaviour is confirmed by the plasma position signal Δ that is computed from the Faraday rotation signals using the method described in [Solt-83] (figure 4.14c). Δ is the zero crossing of the $\alpha(R)$ profile which is closely related to R_{mag} except for a small negative offset due to toroidal effects. An oscillation of amplitude 1 cm on the R_{geo} signal starting at the disruption can be observed. This oscillation is much less pronounced on the R_{mag} signal.

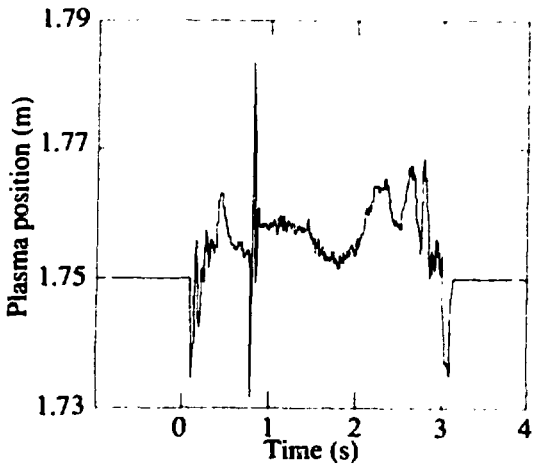

Fig. 4.14c The plasma position signal Δ that is computed using the method described in [Solt-83].

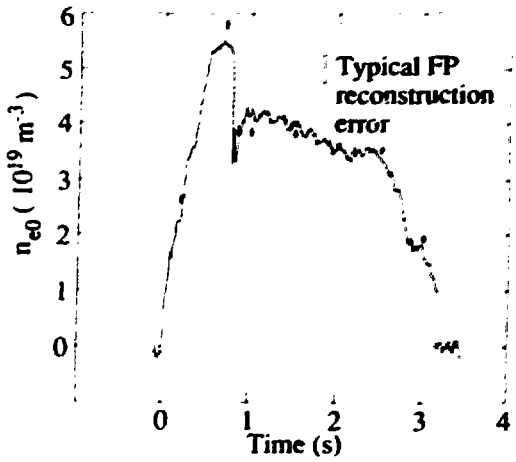

Fig. 4.15 The time trace of the central electron density, n_{e0}. The dots indicate values of n_{e0} as obtained with Method I (cf. Figs. 4.5a-c).

Figure 4.15 shows the time trace of n_{e0} from FP. A steep drop in central electron density at the disruption is followed by a recovery shortly after. The recovery is not complete. The negative density spike is reflected on the Shafranov shift, showing a sharp drop followed by a rapid increase to its original value. The dots indicate n_{e0} values obtained by Method I (cf. Figs. 4.17a-c).

Figure 4.16 shows the time trace of q_0. After the start of the discharge, the signal steeply decreases to a value of around 0.8, crossing the $q_0 = 1$ line at t = 0.32 s (i.e. shortly after the plasma current has reached its plateau value). Prior to the disruption the value increases slightly but stays below 1, although there is no sawtooth activity. Following the disruption, q_0 remains close to 0.8 during the sawtoothing phase of the discharge.

The reconstructed values of n_{e0} and q_0 agree well with the results derived by conventional analysis. For comparison, Figs. 4.17a-c show electron density distributions as obtained by both methods and Figs. 4.17d-f safety factor profiles as obtained by both methods at three different times of the same discharge.

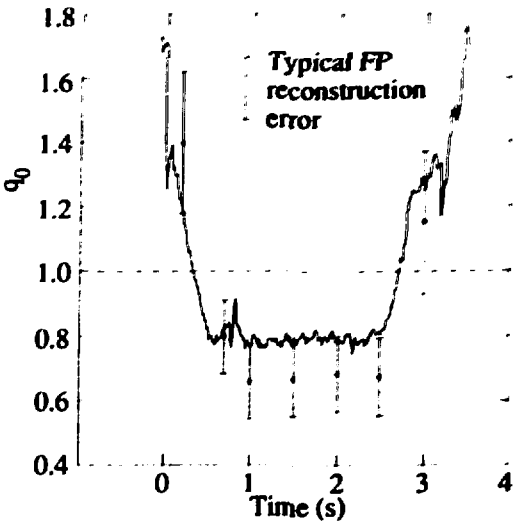

Fig. 4.16 The time trace of q_0. The FP error bar shown is ε^{rec}.

4.3.6 Discussion

4.3.6.1 Results for discharge # 14214

The value of q_0 obtained with FP ($q_0 = 0.8 \pm 0.1$) is the result of a self-consistent method employing ideal MHD equilibria as the basis for the analysis. Given the plasma model we have chosen, we are able to devise a χ^2-test, and reject the hypothesis $q_0 \geq 1$ with 95% certainty. In other words, $q_0 \geq 1$ would require a more complex model than the one adopted here. On the other hand, the data presently available are well reproduced by the present model, and the need for more complexity is not apparent.

Time traces for several important plasma parameters for the typical discharge # 14214 have been obtained using FP analysis. These traces satisfactorily reproduce the traces obtained by method I. In particular, the plasma position signal Δ compares well with R_{mag} (FP). The slow oscillations (having a period $\approx$ 0.25 s) present in the R_{geo} signal but absent in the Δ and

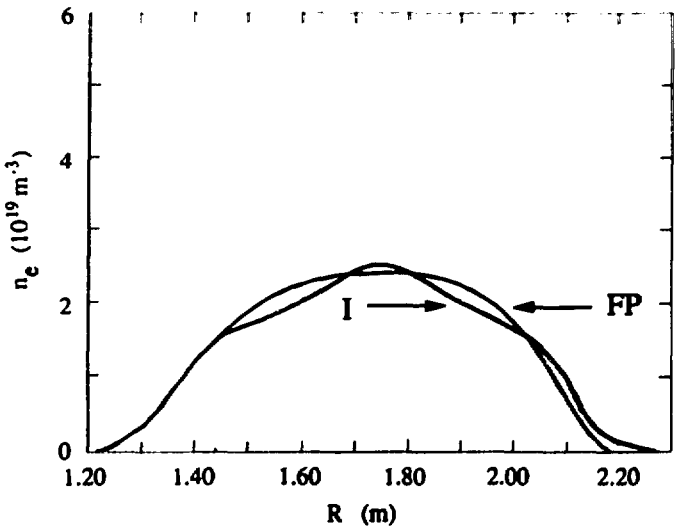

Fig. 4.17a Electron density profiles obtained by Method I and FP at t = 0.2 s.

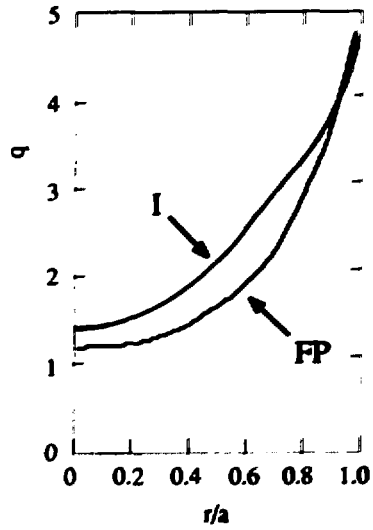

Fig. 4.17d Safety factor profiles obtained by Method I and FP at t = 0.2 s.

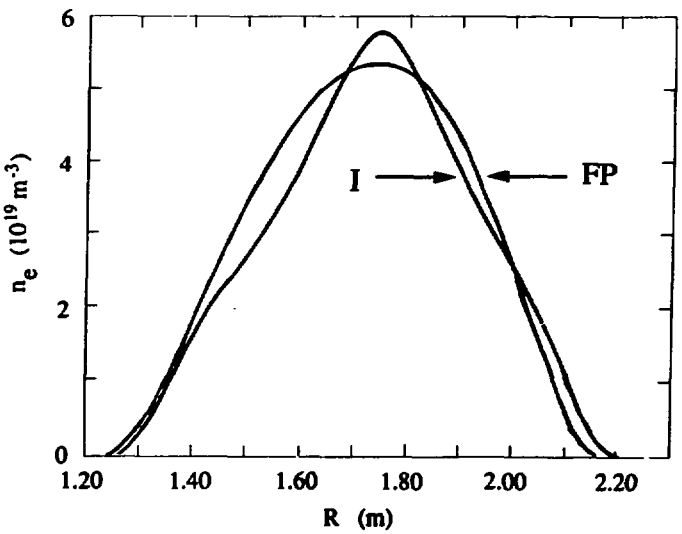

Fig. 4.17b Electron density profiles obtained by Method I and FP at t = 0.7 s.

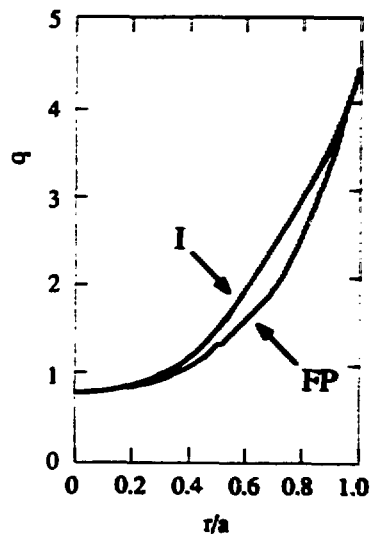

Fig. 4.17e Safety factor profiles obtained by Method I and FP at t = 0.7 s.

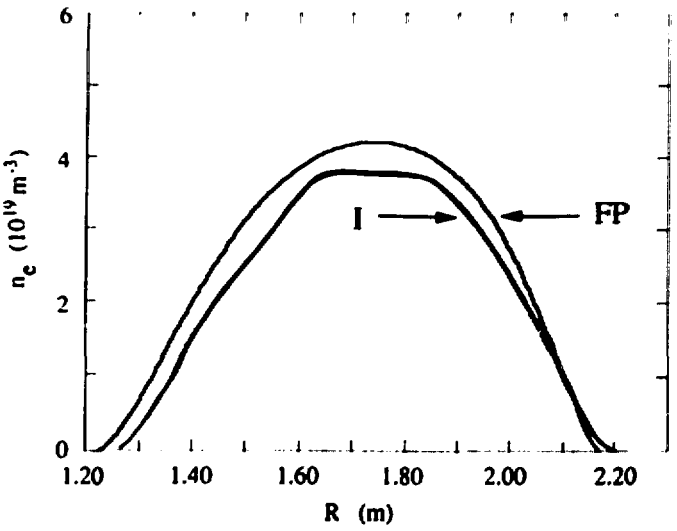

Fig. 4.17c Electron density profiles obtained by Method I and FP at t = 1.0 s. Note that the electron density profiles from FP have a relatively simple shape since they are parametrized with three parameters only, whereas the profiles from Method I are obtained from spline fits to the data.

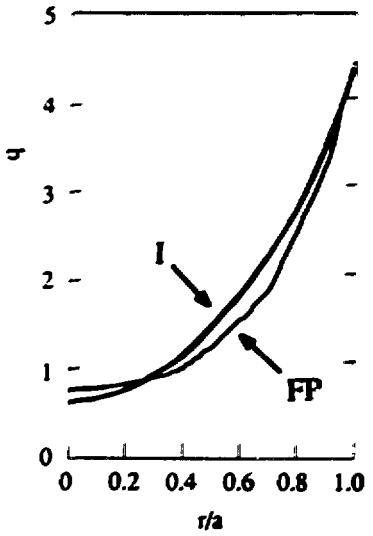

Fig. 4.17f Safety factor profiles obtained by Method I and FP at t = 1.0 s.

the R_{mag} signal are due to the fact that R_{geo} refers to the plasma boundary, whereas the Δ and R_{mag} signals refer to the magnetic axis. The oscillation on the R_{geo} signal following the disruption is also seen on the a_{min} signal, albeit with reversed sign.

4.3.6.2 Future extensions of the method

The analysis presented in this paper employs a very simple flux surface geometry of shifted circles. The method can easily be modified to handle more complex geometries (e.g. allowing for vertical plasma displacement or plasma elongation). In order to do so, however, more geometrical measurement data are required (e.g. Mirnov coil signals could help determine the plasma boundary location and shape).

Another assumption made in this analysis is that the electron density profile is a flux quantity, $n_e = n_e(\psi)$, because it provides an important link between measurement data and flux surface geometry. Therefore this assumption can only be removed if other measurements are

incorporated that give information on the flux surface geometry, such as Soft X-ray tomography.

A minor improvement that will be implemented is the replacement of the approximate equations (4.27a and b) used in computing the simulated interferometry and polarimetry detector signals by a ray-tracing algorithm and a model for the optics and electronics in the detection system. This will not affect any of the results presented here significantly.

The parametrizations of the Π and Γ profiles used now do not allow for e.g. hollow profiles. In order to admit more complex profiles in the formalism, it would be necessary to increase the spatial resolution of the combined interferometric and polarimetric diagnostics.

The prospects for routine use of the data analysis method presented here at TEXTOR are good. The addition of magnetic signals to the analysis is anticipated.

4.3.7 Acknowledgements

The authors would like to thank Bas Braams and Patrick McCarthy for providing many useful insights into the subject of Function Parametrization. The latter also provided some of the algorithms used in the polarimetry simulations. We acknowledge the work of Hans Goedbloed, author of the HBT equilibrium code that formed the basis of our simulations. Guido Huysmans has been of great help in adapting HBT to our purpose. We are endebted to Chris Schüller for many fruitful discussions on the theme of this paper. This work was performed under the Euratom-FOM Association agreement with financial support from NWO and Euratom.

5. The safety factor and MHD mode activity

5.1 Introduction

The existence of MHD modes associated with rational surfaces, as mentioned in chapter 2, affects plasma stability and transport deeply. The observation of such modes is often difficult for various reasons: there may be several modes present simultaneously, and some or all may have small amplitudes. Most diagnostics provide spatially averaged data (e.g. line integrals of the electron density or soft X-ray emission; electron temperatures averaged over certain measuring volumes) or otherwise composite data (e.g. magnetic fluctuations observed by pick-up coils due to modes at different rational surfaces), which makes the interpretation of the data in terms of local mode activity extremely difficult in most cases.

In section 5.2 some of the most basic methods used in the analysis of MHD mode activity are described. In section 5.3 these methods are applied to observations of mode activity during the pre-disruption phase of the plasma at RTP. In section 5.4 the observation of pressure inside island structures at JET is discussed. Finally, section 5.5 reports on MHD activity during Pellet Enhanced Performance (PEP) discharges at JET. This section is a reproduction of the paper *Shear reversal and MHD activity during Pellet Enhanced Performance shots in JET* [Hugo-91b] in which many diagnostics were used to obtain a consistent picture of the local mode activity. The observed modes are linked with rational surfaces, and thus the observations also led to a reassessment of the magnetic equilibrium. The JET shots that were investigated were found to have negative shear in the central region, i.e. $s = \frac{\rho}{q}\frac{\partial q}{\partial \rho} < 0$, in agreement with earlier theoretical predictions [Huys-91].

5.2 Methods used in the analysis of MHD activity

MHD modes or magnetic islands are helical structures associated with rational q-surfaces (see chapter 2). A primary point of interest in the analysis of MHD modes is to establish the relationship between the electron temperature fluctuation δT_e, the electron density fluctuation δn_e and the current fluctuation δI inside the island (at the O-point) with respect to the situation outside the island (at the X-point), as this provides insight into the nature of the islands.

Depending on the sign of the shear, the incremental current δI flowing in the island O-point parallel to the magnetic field on the flux surface is positive or negative [Rebu-90]. If, for simplicity, one considers an equilibrium with circular concentric nested flux surfaces in

cylindrical approximation, the incremental current can be expressed as:

$$\delta I = \sum_{m,n} \delta I_{m,n} \sin(m\theta - n\phi - \chi_{m,n} - \omega_{m,n}t)\, \delta(\rho - \rho_{m,n}) \tag{5.1}$$

where $\delta I_{m,n}$ is the incremental current associated with the (m,n) island, $\chi_{m,n}$ is the phase of island chains on separate flux surfaces and can be taken equal to zero if just one mode is described, and $\omega_{m,n}$ is the rotation velocity of the island, which need not be constant in time. If the shear is positive at the rational surface q = m/n, $\delta I_{m,n}$ is opposite to the main current I_p in the island O-point; otherwise it is in the same direction. Due to the helical symmetry of the structure, it is impossible to distinguish between poloidal and toroidal rotation for modes with m,n > 0 using the magnetic pick-up coils only. The Kronecker δ-function $\delta(\rho - \rho_{m,n})$ is an approximation of the radial current localization on the flux surface; in reality the island width is finite [Bate-80].

The effect of such rotating helical structures on poloidal field pick-up coils is

$$\dot{B}_\theta(\theta,\phi,t) = \sum_{m,n} A_{m,n}\omega_{m,n} \cos(m\theta - n\phi - \chi_{m,n} - \omega_{m,n}t) \tag{5.2}$$

where the amplitude $A_{m,n}$ is related to the incremental current $\delta I_{m,n}$, in cylindrical approximation, by

$$A_{m,n} = \frac{\mu_0\, \delta I_{m,n}}{4\pi\rho_B} \left(\frac{\rho_{m,n}}{\rho_B}\right)^m \tag{5.3}$$

where ρ_B is the radial position of the poloidal field pick-up coil. The spatial dependence of the observed amplitude generally prevents the observation of high m modes with the magnetic diagnostic. In particular, the pick-up coils are often situated at such distances from the plasma that the term between brackets in Eq. (5.3) is of the order of $\frac{1}{2}$ or smaller for most modes, and thus the observed amplitude of the modes decreases approximately exponentially with m.

In Eq. (5.2) the term $A_{m,n}\omega_{m,n}$ appears because of the time derivative. It is possible, however, to determine the amplitude of the oscillating quantity $\tilde{\dot{B}}_\theta = \dot{B}_\theta - \langle \dot{B}_\theta \rangle$ (here $\langle\rangle$ denotes averaging in time over a few periods of oscillation), which is determined by $A_{m,n}$ only. In particular, if a single mode dominates the magnetic field oscillation or if simultaneous modes can be distinguished by means of their frequencies, Eq. (5.3) allows evaluation of the incremental current δI if the radial position $\rho_{m,n}$ of the mode is known.

The expression for the radial island width, w, is given in terms of the radial field

perturbation at the rational surface [Wess-87]:

$$w = 4\left(\frac{\rho\ q\ \hat{B}_\rho}{m\ q'\ B_\theta}\right)^{\frac{1}{2}}, \tag{5.4a}$$

where $\hat{B}_\rho$ is the amplitude of the radial field perturbation due to the island. Using the model for the current distribution given by Eq. (5.1) this can be rewritten in terms of the current flowing in the island:

$$w = \frac{4}{\pi}\left(\frac{\mu_0\ q\ \delta I_{m,n}}{q'\ B_\theta}\right)^{\frac{1}{2}} \tag{5.4b}$$

in which all quantities are evaluated at the rational surface.

It is possible to separate the poloidal and toroidal mode number contributions to the observed oscillations by means of a Fourier analysis with respect to the angles θ or ϕ of the pick-up coils. Define

$$F_m^c = \frac{1}{\pi}\int_0^{2\pi} \dot{B}_\theta(\theta,\phi,t)\cos(m\theta)\,d\theta,$$

$$F_m^s = \frac{1}{\pi}\int_0^{2\pi} \dot{B}_\theta(\theta,\phi,t)\sin(m\theta)\,d\theta \tag{5.5}$$

In practice the integrals (5.5) are replaced by sums over the pick-up coils. These Fourier coefficients can be combined to give

$$\sqrt{(F_m^c)^2 + (F_m^s)^2} = \sum_n A_{m,n}\omega_{m,n} = S_m \tag{5.6}$$

i.e. the combined amplitude of all modes of poloidal mode number m. A similar procedure can be applied to a toroidal set of pick-up coils in order to obtain F_n^c and F_n^s, from which the toroidal mode amplitude S_n can be computed.

As mentioned above, these derivations are made for a simplified circular, concentric flux surface geometry in cylindrical approximation. A more detailed analysis would include the effects of an eccentric plasma position, the Shafranov shift, the non-circularity of the plasma boundary and the toroidal effect [Harl-89]. The simple procedure outlined above already gives quite satisfactory results for modes of low poloidal mode number m at RTP, but is inadequate for poloidal mode determination in the D-shaped JET plasmas. In this case more advanced

techniques are required, such as Singular Value Decomposition [Smeu-91]. At JET, hardware combinations of poloidal pick-up coils in a toroidal set provide signals S_n, for which this type of analysis is valid despite the D-shape. At RTP no toroidal set of pick-up coils is available.

Another important analysis tool is frequency analysis. Standard Fourier methods yield frequency spectra of a single pick-up coil. A peak in the spectrum should correspond to a certain mode number. In particular, with the assumption that the plasma rotation is dominantly toroidal, in agreement with experimental observation [Brau-83], the peaks at different frequencies, f_n, can only be due to modes with different toroidal mode number n. The toroidal rotation velocity profile as a function of minor radius is roughly Gaussian with the peak in the centre. The frequency of an observed mode f_n is related to the average toroidal plasma rotation frequency: $f_{rot} = <v_\phi>/(2\pi R_{geo})$. Even though the plasma rotation is inhomogeneous, it is observed very often that modes at different rational surfaces couple, implying that the magnetic mode-structures do not follow the local plasma rotation exactly [Brau-83]; for coupled modes $\omega_{m,n} = \omega$ or $f_n = nf_1$. Thus the frequency spectrum provides a diagnostic for the toroidal mode numbers involved.

Often it is observed that plasma rotation is not constant in time: the plasma is either spinning up or down (as in the case of modelocking). Then a 'binning' procedure in which the signal is subdivided into short time sections, for each of which a spectrum is made, provides insight into the time development of the dominant frequencies.

The modes at different radial positions can only be distinguished by means of diagnostics that have sufficiently high spatial resolution such that local measurements of quantities that are affected by the MHD modes can be made, e.g. ECE temperature measurements. In addition, line integral measurements from e.g. interferometers or soft X-ray cameras can provide local information. These measurements, however, are more difficult to interpret due to the deconvolution (Abel-inversion) that is needed.

5.3 MHD activity and density limit disruptions at RTP

MHD behaviour of plasmas prior to density limit disruptions has previously been reported in [Wess-89] for JET. In this section observations with a number of fast diagnostics of similar disruptions in RTP are presented.

Fig. 5.1 demonstrates the behaviour of a typical density limit disruption (shot R19900724.006). Fig. 5.1a shows time traces of the plasma current and the horizontal position of the plasma. Fig. 5.1b shows the magnetic activity for m = 1, 2 and 3. After an initial MHD

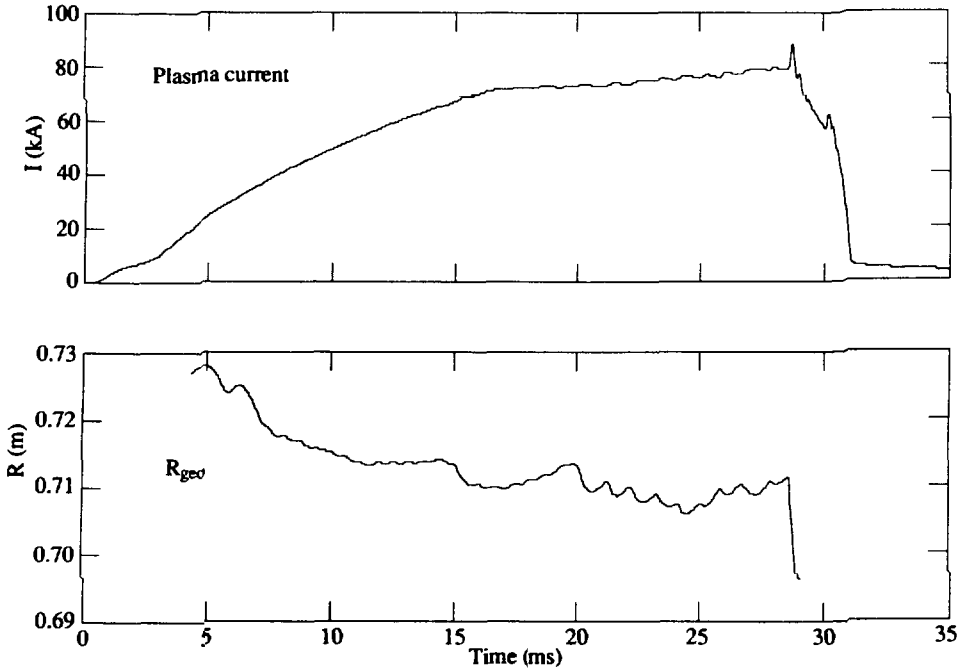

Fig. 5.1a Plasma current and horizontal plasma position for discharge R19900724.006. At t = 28 ms, a disruption occurs.

quiescent phase during the current rise, MHD activity (m = 2) appears at 15 ms. A sequence of minor m = 2 disruptions sets in at 20 ms, leading to a major disruption at 28 ms. Each minor disruption creates an inward movement of the plasma, after which the plasma recovers and moves outward again. The fast inward movement can be seen as a spike on the m = 1 signal.

The explanation of this type of behaviour is thought to be as follows [Wess-89]. Due to increased radiation of impurity ions at high density, the edge region of the plasma cools down. This cooling reduces the current density in the edge, thus creating a current profile with steep gradients inside and near the q = 2 surface, which strongly destabilizes the (m,n) = (2,1) mode. The violent m = 2 mode redistributes the plasma energy around the q = 2 surface: the temperature inside the surface is lowered while the temperature outside the surface is increased. As a consequence, the current density profile is modified and the gradients are reduced, such

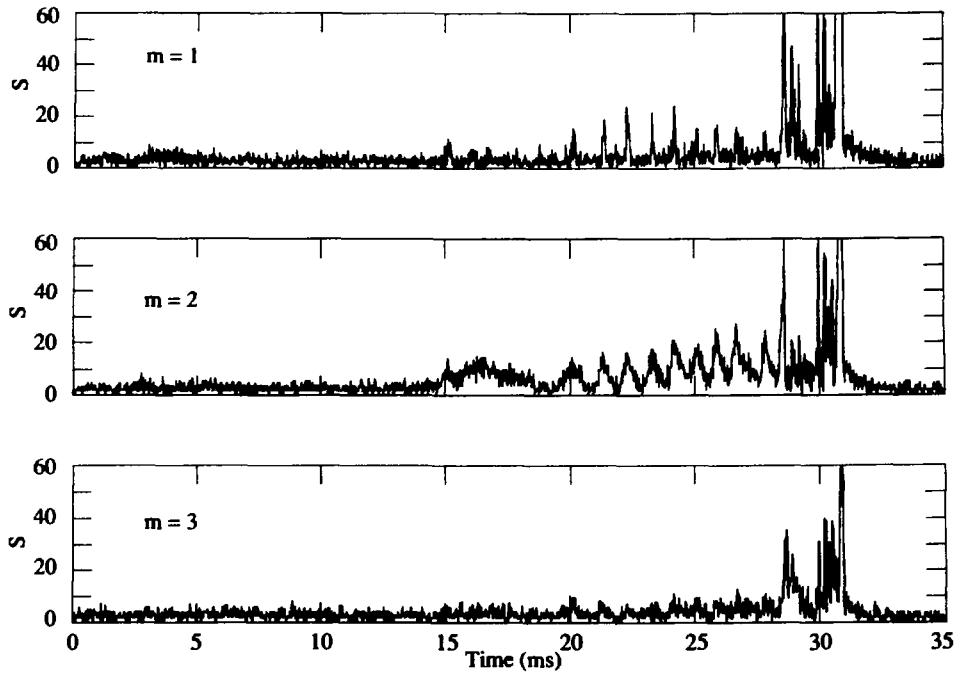

Fig. 5.1b Magnetic activity S_m for m = 1, 2 and 3. A sequence of minor disruptions occurs between 20 ms and 28 ms.

that the m = 2 mode is stabilized. The cooling in the edge region continues, however, and a following minor disruption develops. The sequence of minor disruptions is followed by a major disruption when an m = 1 mode is destabilized.

Due to the sudden reduction of the kinetic energy content of the plasma and the flattening of the current profile during the minor disruptions, the Shafranov parameter $\Lambda = \beta_p + \frac{1}{2} l_i$ drops. The parameter β_p is the ratio of the averaged kinetic pressure of the plasma and the magnetic field pressure exerted by the poloidal magnetic field at the edge (see Appendix). The normalized internal induction l_i is a measure for the peaking of the current density profile. The vertical magnetic field required to keep the plasma at its position $R = R_{geo}$ is

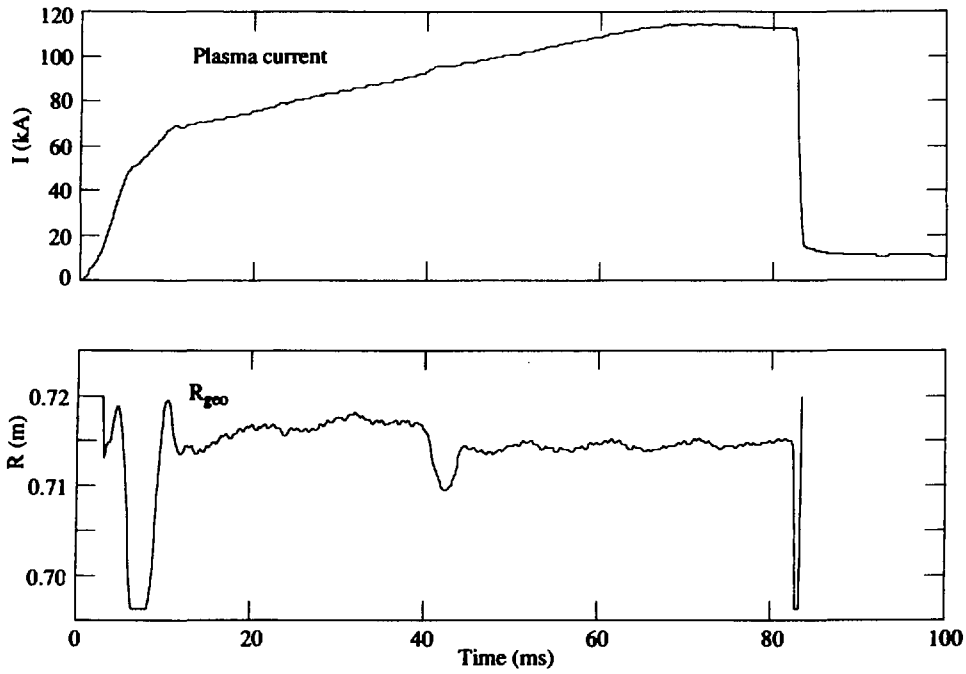

Fig. 5.2a Plasma current and horizontal plasma position for discharge R19900724.005. At t = 83 ms, a disruption occurs.

approximately [Frei-87]:

$$B_v = \frac{\mu_0 I_p}{4\pi R_{geo}}\left(\Lambda - \frac{3}{2} + \ln \frac{8R_{geo}}{a_{min}}\right), \tag{5.7a}$$

from which it can be seen that, since the vertical field B_v and the plasma current I_p are approximately constant on the fast timescale of the disruption,

$$\frac{\Delta R_{geo}}{R_{geo}} = \frac{\Delta\Lambda}{\Lambda - \frac{5}{2} + \ln \frac{8R_{geo}}{a_{min}}} \tag{5.7b}$$

The change in the Shafranov parameter, $\Delta\Lambda$, is negative while the denominator on the right-hand side is positive. Thus the inward movement of the plasma ΔR_{geo} can be understood.

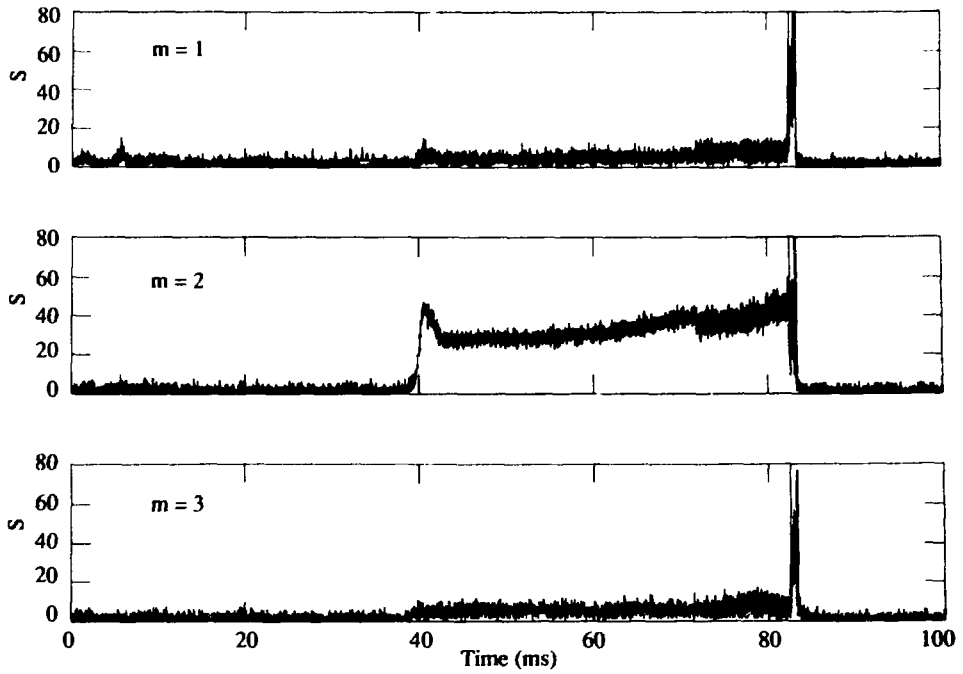

Fig. 5.2b Magnetic activity S_m for m = 1, 2 and 3. A strong m = 2 mode sets in at t = 40 ms.

Eq. (5.7b) allows an estimate of $\Delta\Lambda$ to be made. For the minor disruption at t = 20 ms ΔR_{geo} = –4.5 mm and R_{geo} = 71.3 cm (Fig. 5.1a). Taking a_{min} = 17.5 cm and $\Lambda \approx 1$ (as confirmed by Function Parametrization, see chapter 4) $\Delta\Lambda$ = –0.013, or 1.3% of Λ.

Fig. 5.2 shows an example of a density limit disruption without the prior sequence of minor disruptions (shot R19900724.005). Fig. 5.2a shows the plasma current and the horizontal plasma position. Fig. 5.2b shows the magnetic activity for m = 1, 2 and 3. Strong MHD activity (m = 2) sets in at 40 ms and causes an inward movement of the plasma, from which it can be deduced that it is accompanied by a reduction of Λ. Fig. 5.2c shows a frequency - vs - time plot of a vertical interferometer channel at R = 0.72 m. A frequency analysis of a pick-up coil yields an identical picture. It can be seen that the m = 2 mode, starting at 40 ms at 10 kHz, slows down to 6 kHz at 80 ms, at which time the major disruption occurs.

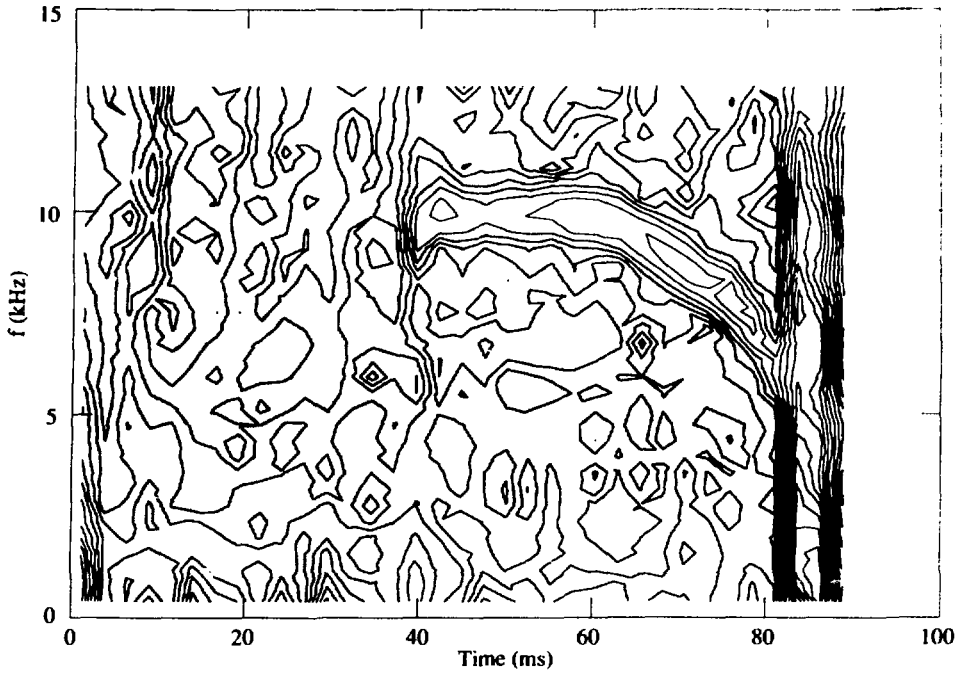

Fig. 5.2c Frequency - vs - time plot of the signal of the 2 mm interferometer, showing the slowing down of the m = 2 mode. For this analysis the signal was divided into 35 time sections of 2.5 ms, and for each section a spectrum was made.

The current in the m = 2 island is computed using Eq. (5.3). The relevant quantities are evaluated at t = 50 ms (m = 2 mode activity signal $S_2 = 30\ Ts^{-1}$; plasma rotation frequency f = 10 kHz; pick-up coils at $\rho_B = 0.213$ m; plasma minor radius $a_{min} = 0.175$ m; major radius $R_{geo} = 0.72$ m; toroidal magnetic field $B_\phi = 1.9$ T; plasma current $I_p = 100$ kA). Assuming that the only mode contributing to the S_2 signal is the (m,n) = (2,1) mode, the observed mode amplitude $A_{2,1} = S_2/(2\pi f) = 0.48$ mT. The safety factor at the plasma boundary is $q_{cyl} = 4.0$ (see Appendix). Assuming that nearly all current flows within the q = 2 surface (in agreement with the destabilization of the q = 2 mode, see the argument above) the q-profile is parabolic outside this surface: $q(\rho) = q_{cyl}(\rho/a_{min})^2$ ($\rho \geq \rho_{2,1}$), so the q = 2 surface is at $\rho_{2,1} \approx 0.12$ m. Thus an estimate of the current flowing in the island is: $\delta I_{2,1} = 46.4 \cdot \rho_{2,1}^{-2} \approx 3.2$ kA.

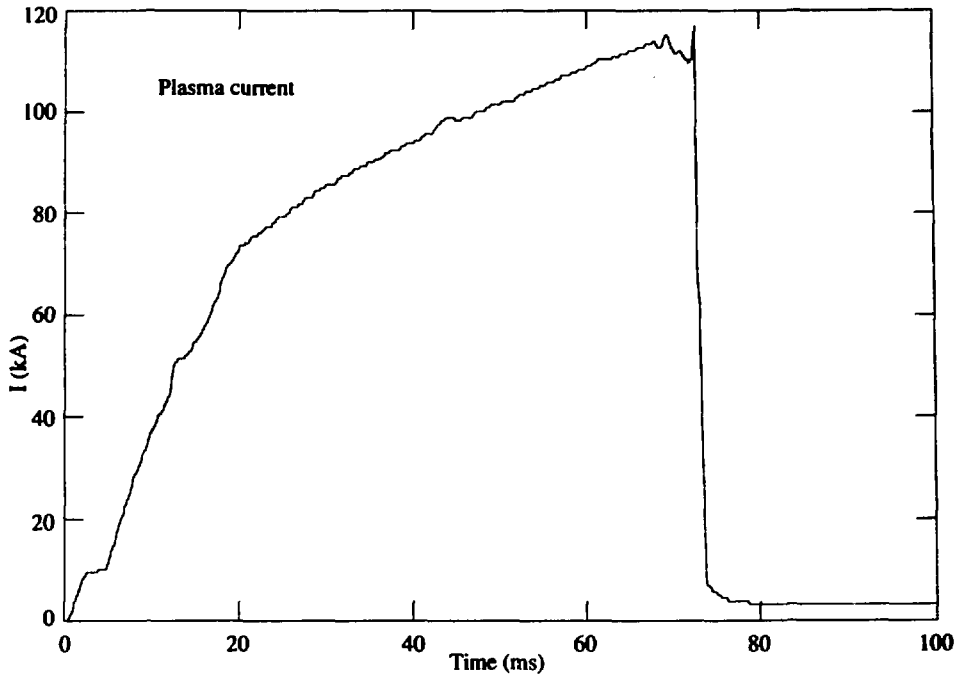

Fig. 5.3a Plasma current for discharge R19900718.013. At t = 73 ms, a disruption occurs.

The radial width of the m = 2 island is computed as follows. If the q-profile is assumed to be parabolic as above, then the derivative $q' = \partial q/\partial \rho \approx 31$ m^{-1} at $\rho = 0.12$ m. The local poloidal magnetic field is found using Eq. (2.28): $q = \rho B_\phi/(RB_\theta)$, so $B_\theta(\rho_{2,1}) = 0.16$ T. Using $\delta I_{2,1}$ as above and Eq. (5.4) it follows that $w = 7.41 \cdot 10^{-4} \cdot \rho_{2,1}^{-2} \approx 5.1$ cm.

This is in agreement with measurements taken in similar discharges with a multichannel interferometer that indicate that the typical width of comparable m = 2 islands is 4 cm [Lamm-91]. It should be noted that the observed island width can be smaller than the width computed from the magnetic measurements due to the presence of a stochastic layer around the island separatrix.

Fig. 5.3 shows another example of a density limit disruption (shot R19900718.013). Fig. 5.3a shows a time trace of the plasma current, in which several 'humps' can be recognized. The plasma ends at 73 ms with a major disruption. Fig. 5.3b shows the magnetic activity for m = 1, 2 and 3. At 12 ms a mode of unknown character is destabilized during

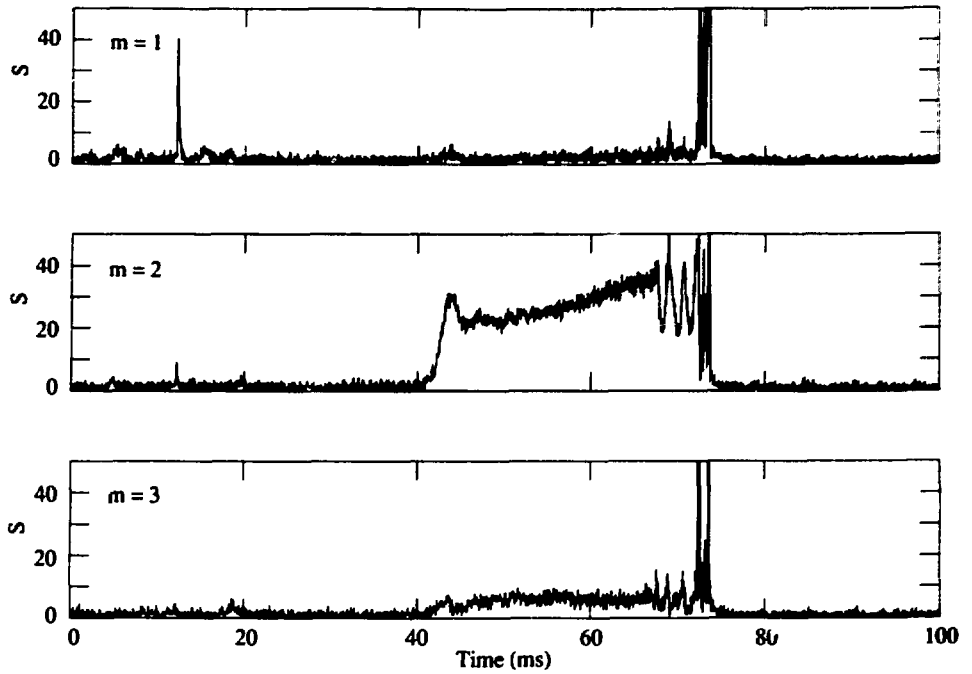

Fig. 5.3b Magnetic activity S_m for m = 1, 2 and 3. A strong m = 2 mode sets in at t = 42 ms. At 68 ms a series of minor disruptions starts, preceding the major disruption.

the current ramp-up and the induced plasma motion shows up in the m = 1 signal as a spike, while the plasma current shows a temporary increase due to the decrease in plasma inductance. At 42 ms a m = 2 mode is destabilized, again accompanied by a temporary increase in plasma current, that grows and at 68 ms leads to a series of m = 2 minor disruptions, terminated at 73 ms by a major disruption. Fig. 5.3c shows a plot of frequency - vs - time of coil $B_\theta(0)$ on the outboard side, showing that the m = 2 mode slows down from 10 kHz to 5 kHz immediately prior to the disruption. This behaviour has also been observed in other tokamaks [Wess-89], where the slowing-down sometimes progresses to a complete standstill ('modelock').

Finally, density limit disruptions without any significant MHD precursor activity have also been seen. The general picture emerging from the reported observations seems to confirm the reported density limit behaviour [Wess-89] in detail.

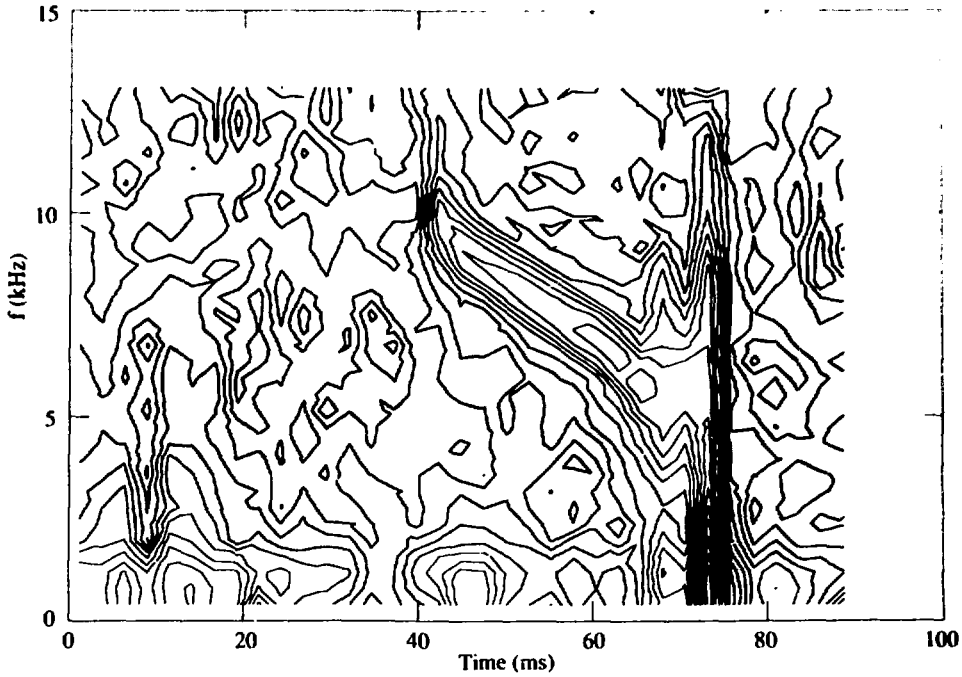

Fig. 5.3c Frequency - vs - time plot of the signal of pick-up coil $B_\theta(0)$, showing the slowing down of the m = 2 mode. For this analysis the signal was divided into 35 time sections of 2.5 ms, and for each section a spectrum was made.

5.4 Observation of pressure inside magnetic islands at JET

At JET, magnetic modes are sometimes observed to rotate slowly with a frequency of around 100 Hz. The density oscillations associated with these modes are measured with the one-channel interferometer sampling at 1 kHz [Fess-87]. These data are correlated with simultaneous measurements from the magnetic pick-up coils, the ECE polychromator and the soft X-ray cameras. The ECE polychromator measures the temperature at discrete points along a horizontal chord in the midplane and the interferometer measures the line-integral density along a vertical chord at R = 3.142 m in the same octant (octant 7, see section 5.5).

Fig. 5.4 compares the measured oscillations of the electron temperature, density and poloidal magnetic field (shot 23085). The electron temperature trace displays the slow mode and a fast mode. Analysis of magnetic and Soft X-ray data shows that the slow mode has (m,n) = (2,1) mode numbers and that it rotates in the direction of the electron diamagnetic drift. Taking account of the symmetry of the mode (m=2) and the poloidal position of the polychromator and the interferometer, the electron temperature and density oscillations are in phase. The poloidal magnetic field oscillations measured by pick-up coils above and below the midplane show that B_p is minimal in the midplane in octant 4 when the electron temperature in octant 7 is close to its maximum (the toroidal separation between the diagnostics is 147°). Due to the toroidal symmetry of the mode (n=1) the poloidal magnetic field and the temperature oscillations are in phase. The oscillations are therefore associated with a rotating island with an O-point corresponding to a minimum of T_e and n_e, assuming that the shear is positive. The pressure is lower at the island O-point than at its X-point by between 3 and 10%.

This conclusion is at variance with observations at RTP where a strong enhancement of electron density inside the islands is observed [Lamm-91]. Similarly, the m = 1 'snake' at JET also displays a strong enhancement of density inside the island, while the temperature decrease is moderate. All observations in JET and RTP agree, however, that with positive shear the temperature inside the island is diminished in accordance with the necessity to have $\delta I_{m,n}$ opposite to the main plasma current to sustain the island. Apparently, the electron pressure increment δp_e in the island can be either positive or negative depending on the ontogenesis of the island.

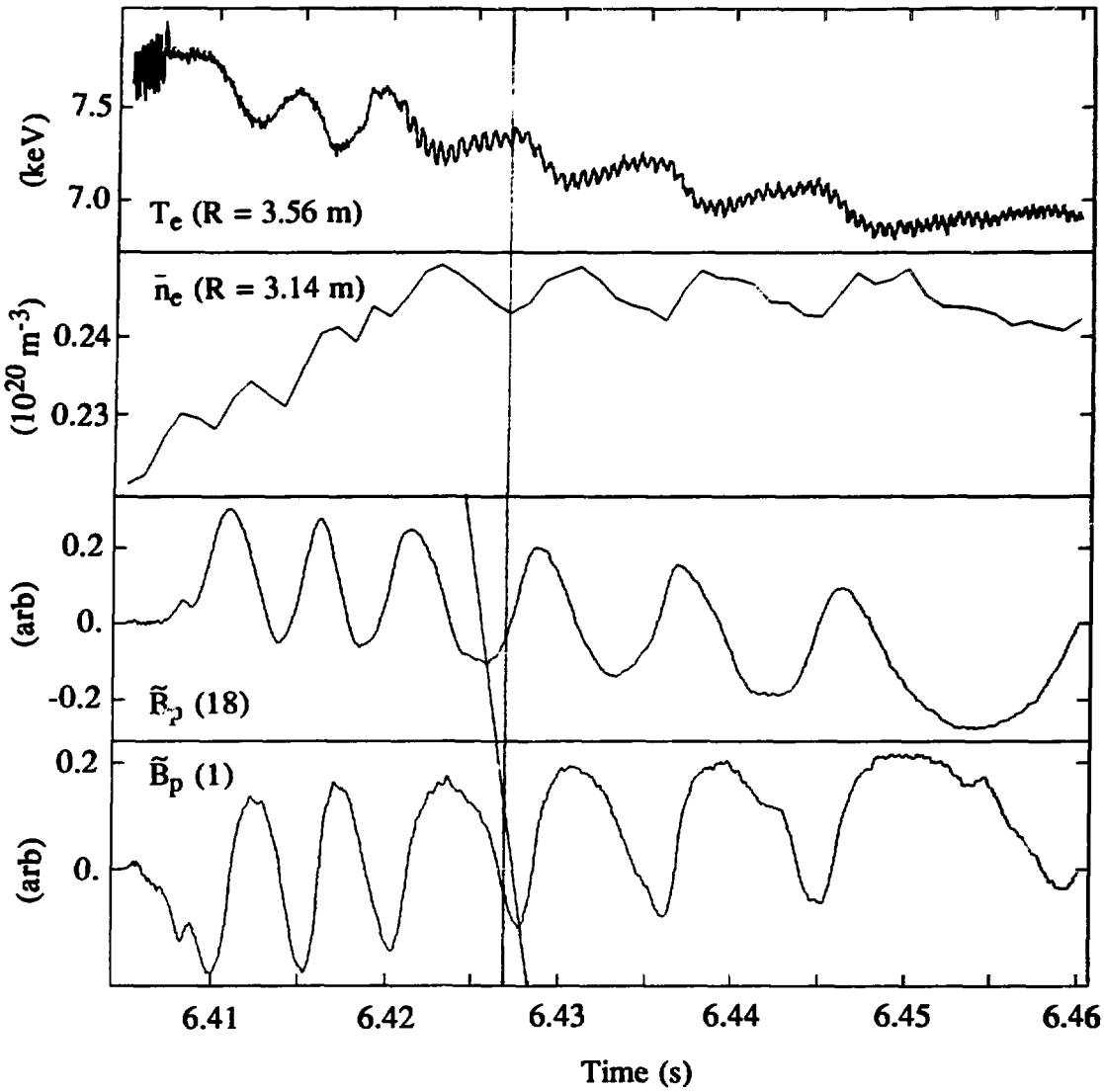

Fig. 5.4 Time traces displaying the correlation between the ECE electron temperature measured at R = 3.56 m by the polychromator, the line integrated electron density (from the 2 mm interferometer) and two poloidal field pick-up coils for a slowly rotating (2,1) mode after termination of the PEP phase (shot 23085).

5.5 Shear reversal and MHD activity during Pellet Enhanced Performance plasmas in JET

M. HUGON, B.Ph. VAN MILLIGEN[1], P. SMEULDERS, L. APPEL[2], D. BARTLETT, D. BOUCHER, A. EDWARDS, L. ERIKSSON, C. GOWERS, T.C. HENDER[2], G. HUYSMANS[1], J. JACQUINOT, P. KUPSCHUS, L. PORTE[3], P.H. REBUT, D. START, F. TIBONE, B.J.D. TUBBING, M. WATKINS, W. ZWINGMANN

JET Joint Undertaking
Abingdon, Oxfordshire OX14 3EA, United Kingdom

[1] FOM Instituut voor Plasma Fysica "Rijnhuizen"
PO Box 1207, 3430 BE Nieuwegein, The Netherlands

[2] UKAEA / Euratom Fusion Association
Culham Laboratory, Abingdon, Oxfordshire OX14 3DB, United Kingdom

[3] University of Strathclyde, Glasgow G4, United Kingdom

5.5.1 Abstract

Analysis of MHD activity in Pellet Enhanced Performance (PEP) pulses is used to determine the position of rational surfaces associated with the safety factor q. This gives evidence for negative shear in the central region of the plasma. The plasma equilibrium calculated from the measured q values yields a Shafranov shift in reasonable agreement with the experimental value of about 0.2 m. The corresponding current profile has two large off-axis maxima in agreement with the bootstrap current calculated from the electron temperature and density measurements. A transport simulation shows that the bootstrap current is driven by the steep density gradient, which results from improved confinement in the plasma core where the shear is negative. During the PEP phase (m,n) = (1,1) fast MHD events are correlated with collapses in the neutron rate. The dominant mode preceding these events usually is n = 3, whereas the mode following them is dominantly n = 2. Toroidal linear MHD stability calculations assuming a non-monotonic q-profile with an off-axis minimum decreasing from above to below 1 describe this sequence of modes (n = 3, 1, 2), but always give a larger growth rate for the n = 1 mode than for the n = 2 mode. This large growth rate is due to the high central poloidal beta of 1.5 observed in the PEP pulses. Finally, a rotating (m,n) = (1,1) mode is observed as a hot spot with a ballooning character on the low field side. The hot spot has some of the properties of a 'hot' island consistent with the presence of a region of negative shear.

5.5.2 Introduction

A regime of enhanced performance in tokamaks can be accessed by deep pellet injection leading to strongly peaked density profiles in centrally heated plasmas, as first proposed in [Furt-86, Rebu-86a, Schm-86]. This regime has been achieved in JET by injection of deuterium pellets into L-mode limiter ICRF heated plasmas [Schm-88]: it is known as the Pellet-Enhanced Performance (PEP) mode. Similar results, but with neutral beam heating, have been obtained in DIII [Seng-85], JT60 [Naga-89] and JFT 2-M [Odaj-86].

Compared to similar non-PEP pulses the PEP mode is characterized by a substantial increase of the neutron rate (by about 5 times), a very strong peaking of the electron density n_e and kinetic pressure near the plasma centre and a relatively small increase of the global energy confinement time τ_E (by about 20%). The PEP mode is a transient phenomenon, lasting typically 1 to 2 s. It is terminated by a rapid loss of central pressure, often associated with MHD phenomena. It has been suggested [Schm-88] that the abrupt termination of the PEP mode could be associated with the presence of an unstable non-monotonic profile of the safety factor q. The negative shear region in the plasma core is thought to be created by a substantial bootstrap current. The central electron and ion thermal conductivities derived from the experimental data are reduced by a factor 2 - 3 with respect to the usual anomalous values [Taro-88]. This reduction of transport parameters could be due to the existence of negative shear in the plasma centre [Rebu-88].

More recently, in JET the PEP mode has been combined with an H-mode [Tubb-91, Kups-91]. These shots have produced large values of thermonuclear neutron rate of approximately 10^{16} s^{-1} and fusion product $n_D(0)T_i(0)\tau_E \approx 7 \cdot 10^{20}$ m^{-3} keV s in plasmas having nearly the same electron and ion temperatures ($T_e \approx T_i \approx 10$ keV). The projected deuterium-tritium fusion rate in JET is much larger in the PEP mode than in non-enhanced plasmas. In next-step devices, the transient PEP-H mode could be used to ignite the plasma.

It is therefore of great interest to have a better understanding of the MHD behaviour, plasma equilibrium and transport to improve the performance during the PEP phase. This paper reports on the analysis of MHD activity measured by several diagnostics at a high sampling rate in the recent PEP-H mode discharges. Section 5.5.3 gives a brief description of the diagnostics and of the data analysis methods involved. Section 5.5.4 discusses the experimental results and their theoretical interpretation and conclusions are given in section 5.5.5. A typical PEP-H mode pulse is described in section 5.5.4.1 and the MHD behaviour during the PEP phase is discussed in section 5.5.4.2. The position of rational q-surfaces obtained from MHD mode

analysis provides experimental evidence for negative shear in the plasma core and this is presented in section 5.5.4.3. A PEP plasma is simulated with a predictive time dependent 1-D transport code in section 5.5.4.4. The MHD modes observed during the PEP phase are compared with the predictions of two toroidal linear MHD codes in section 5.5.4.5. In section 5.5.4.6 the topology of a rotating (m,n) = (1,1) mode is analyzed in detail in the region of negative shear.

5.5.3 Diagnostics and data analysis

5.5.3.1 Diagnostics

The study of MHD activity in JET involves many diagnostics which are located at different poloidal and toroidal positions. The JET vacuum vessel consists of 8 octants, numbered from 1 to 8 in the counterclockwise direction as seen from the top. The following diagnostics have been used in these studies:

Magnetic diagnostic: the poloidal field is measured by a poloidal set of 18 pick-up coils in octant 4 and a toroidal set of 8 such coils located on the outboard side above the midplane inside the vacuum vessel. Each coil has a frequency cutoff at 10 kHz with a slope of 6 dB per octave. In addition, a hardware combination of pick-up coils at different toroidal locations allows measurement of the toroidal mode number n of rotating magnetic modes up to n = 4.

Polychromator: a 12-channel grating polychromator measures the electron temperature locally from the 2nd harmonic extraordinary mode electron cyclotron emission (ECE) on a horizontal chord in the midplane in octant 7 [Tubb-85]. The spatial resolution is approximately 0.06 m radially and 0.15 m in the transverse direction.

Radiometer: the electron temperature is also measured by a 44-channel microwave heterodyne radiometer from the 1st harmonic ordinary mode ECE on a horizontal chord in the midplane in octant 7 [Port-91]. This emission may suffer from cutoff at the plasma frequency in high density pulses. Its spatial resolution is approximately 0.02 m radially and 0.15 m in the transverse direction.

Soft X-rays: the soft X-ray diagnostic is equipped with a 38-channel vertical camera and a 62-channel horizontal camera in octant 2 and 16 toroidal diodes (4 of each in octants 1, 3, 5 and 6 at various elevations above the midplane) [Edwa-86]. The transverse resolution is 0.07 m in the midplane for the vertical cameras.

LIDAR: the LIDAR time-of-flight Thomson scattering diagnostic measures the electron density and temperature profiles every 1.2 s along a horizontal chord in the mid-plane of octant 5 [Salz-88].

5.5.3.2 Data analysis and correlation between diagnostics

It is difficult to determine the poloidal mode number m from the poloidal set of pick-up coils, because the signals are affected by the D-shape of the vacuum vessel, the shape of the plasma for double null discharges and the plasma position. In addition, the pick-up coils measure the combined effects of all modes present in the plasma with a weight which depends on their relative amplitude, radial position and mode number. In the PEP pulses, most of the MHD activity takes place in the central region of the plasma, making the mode number analysis for these central modes very difficult.

The soft X-ray diagnostic provides a powerful tool for local mode number determination. From the toroidal cameras in combination with a selection of horizontal channels it it possible to determine the toroidal mode numbers up to n = 4. Analysis of the horizontal and vertical camera raw data can yield mode numbers up to m = 4. In addition, a static 2-dimensional tomographic reconstruction technique can distinguish between poloidal mode numbers m = 0, 1 and 2 [Gran-88]. If m = 0 (m = 1) can be excluded, m = 4 (m = 3) can be assumed taking into account the symmetries appearing in both cameras and also the properties of the q-profile. A single-camera (vertical or horizontal) rotational tomographic reconstruction technique is also available, which can handle mode numbers up to m = 4 [Smeu-83].

In correlating the data measured by the various diagnostics, care has been taken to take proper account of their relative timing and position. In the present study the direction of the toroidal magnetic field is counterclockwise and the plasma current is in the clockwise direction as seen from the top of the vacuum vessel, which determines the helicity of the magnetic field. Knowledge of the direction of rotation, frequency and mode numbers of an observed mode is essential for the correlation. For diagnostics located in the midplane it is only necessary to know the toroidal mode number, assuming that the plasma rotation is purely toroidal.

5.5.4 Results and discussion

5.5.4.1 A typical PEP-H mode shot

The PEP-H mode pulses investigated here are obtained by injecting one or several pellets into double null plasmas during the current rise before the q-profile has fully evolved. Fig. 5.5

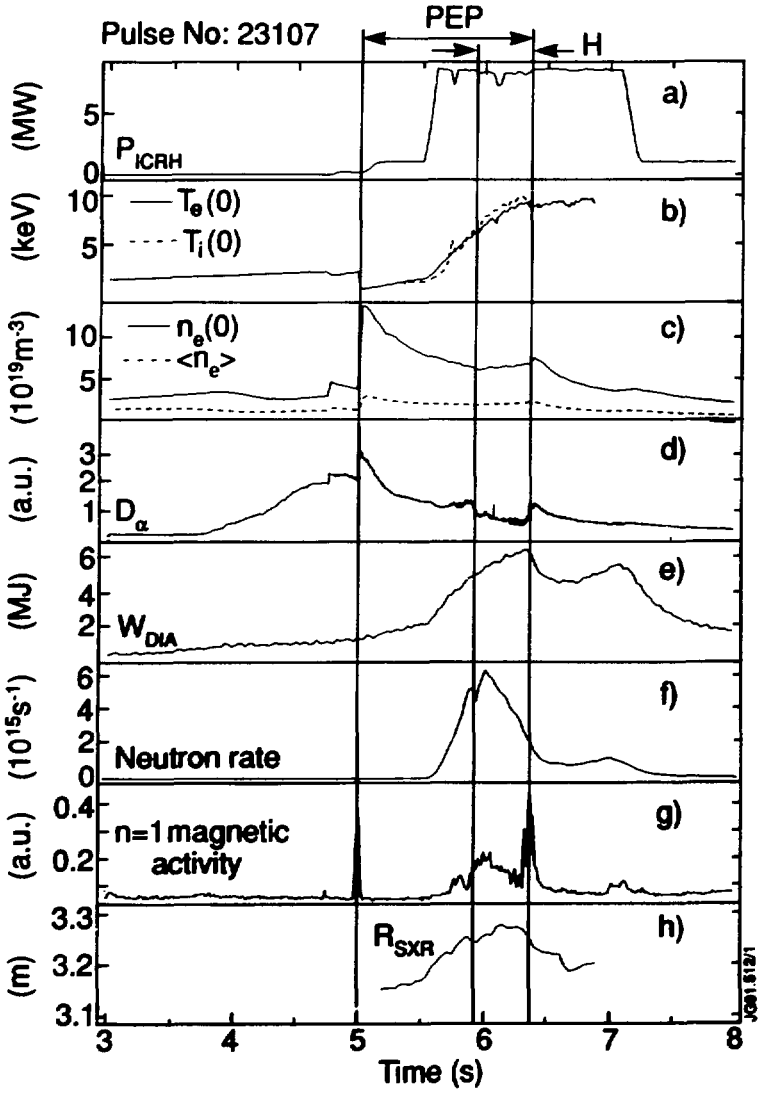

Fig. 5.5 Time traces of some indicative quantities of a typical PEP plasma. Shown are: (a) the ICRH input power (there is no NBI in this pulse); (b) the central electron temperature from the ECE Michelson interferometer and the central ion temperature from He-like nickel radiation line-broadening; (c) the central and volume-average electron density from the far-infrared interferometer; (d) the D_α emission measured along a vertical chord viewing near the X-point region; (e) the total kinetic plasma energy derived from the diamagnetic loop measurements; (f) the total neutron rate; (g) the n = 1 magnetic activity; and (h) the soft X-ray centroid radius closely related to the magnetic axis radius.

shows the time variation of signals characterizing a typical PEP-H mode discharge (Pulse No. 23107). The toroidal magnetic field is 2.9 T. The plasma current reaches a constant value of 3.6 MA at 6.0 s. The X-points are formed at 4.0 s, marked by an increase in the D_α signal. Deuterium pellets are injected at 4.75 s (2.7 mm) and at 5.0 s (4.0 mm), causing a decrease in electron temperature T_e and a sharp increase in the central density $n_e(0)$ and the D_α signal. The 4mm pellet causes a strong peaking of the density profile indicating the beginning of the PEP mode as can be seen in Fig.5.5c. Subsequently the electron density decreases gradually. At 5.5 s, the ICRF heating is ramped up to 9 MW. In this particular pulse NBI heating is not applied. During the PEP-L phase, the electron and ion temperatures and the neutron rate increase sharply from the moment ICRF heating is applied. At 5.9 s there is an L to H transition, indicated by a slight decrease in the D_α signal. During the PEP-H phase the neutron rate reaches a peak value of $6{\cdot}10^{15}$ s^{-1}. At 6.35 s a central n = 1 MHD event terminates both the PEP phase and the H-mode and the plasma energy content W_{DIA} decreases sharply. It should be noted that in many pulses the PEP phase terminates before the end of the H-mode. The PEP phase always takes place well before the onset of the ordinary sawtooth activity (about 8 s in these shots). The H to L transition can be seen from an increase in the D_α signal and a drop in $\langle n_e \rangle$. The PEP phase can be diagnosed by the evolution of the soft X-ray centroid radius, R_{SXR}, which is closely related to the magnetic axis radius, R_{mag}. R_{SXR} is the position of the maximum of the soft X-ray emission profile in the midplane as determined by means of the static tomography technique. R_{SXR} is observed to move strongly outward after starting the ICRF heating due to the build-up of central pressure caused by the central temperature increase at high density. At 6.35 s, a sudden inward movement is observed corresponding to the termination of the PEP phase.

5.5.4.2 MHD behaviour during the PEP phase.

During the PEP phase, collapses in the neutron rate occur that are often correlated with fast MHD events. From the soft X-ray measurements most of these events are found to have (m,n) = (1,1) mode numbers. The n = 1 mode number is confirmed by the magnetic pick-up coils. From the soft X-ray and the magnetic diagnostics it is found that rotating modes preceding the (1,1) event by several tens of ms generally have an n = 3 mode number. In some cases, their poloidal mode number is determined to be m = 4 from soft X-ray emission analysis. Often a fast-growing rotating n = 2 mode starts already in the precursor phase of the fast event with a frequency twice that of the n = 1 mode, indicating that the n = 2 mode arises as a non-linear

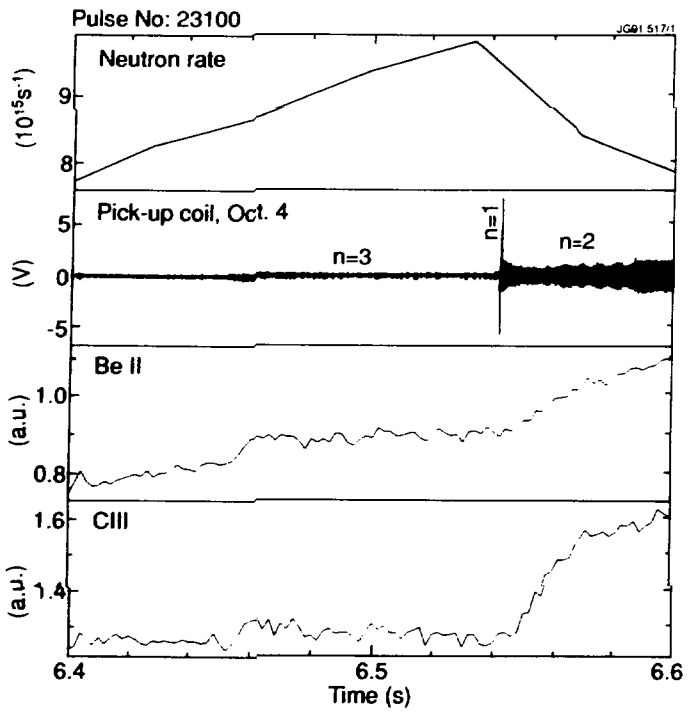

Fig. 5.6 Time traces showing the neutron rate, the signal from a magnetic pick-up coil and the Be II and C III emissions measured on vertical chords through the plasma. Note that the decay in neutron rate coincides with the fast n = 1 MHD event. This event triggers impurity influx.

consequence of the n = 1 mode [Smeu-91]. After the fast event, generally the n = 1 mode amplitude decreases strongly and a dominant n = 2 mode is observed with a weak n = 3 mode. Fig. 5.6 shows a typical example of this behaviour observed in Pulse No. 23100. Impurity radiation at the plasma edge is enhanced by the crash. The resulting impurity influx may lead to a long-term dilution of deuterium in the plasma core and a decrease of the neutron rate. Note that the central ion (from charge exchange measurements) and electron temperatures remain approximately constant during these crashes, indicating that the D-D cross section is not affected.

5.5.4.3 Determination of the q-profile

Fig. 5.7 shows the behaviour of the electron temperature T_e at various positions in the plasma as seen by the polychromator (Pulse No. 23100). As discussed in the previous section, the fast event at 6.542 s is an n = 1 mode, which is preceded by a dominant n = 3 mode and followed by dominant n = 2 modes. The (1,1) fast MHD event does not affect the central electron temperature. Note the non-sinusoidal character of the oscillations after this event and

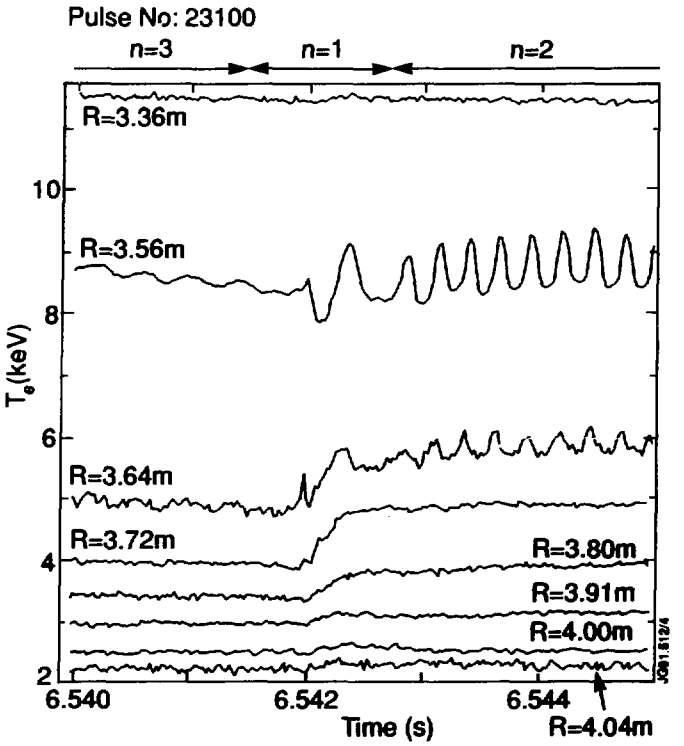

Fig. 5.7 Time traces of the electron temperature from the ECE polychromator at various radii inside the plasma. The event at 6.542 s is the same as the one shown in Fig. 5.6.

the slight phase shift between the channels at R=3.56 and R=3.64 m, suggesting that distinct but coupled modes (on different rational surfaces) may be involved. There is an error of about 0.1 m in the absolute value of the major radii corresponding to the polychromator channel positions. This is due to the uncertainty in calculating the total magnetic field for these plasmas with a large bootstrap current and a total current which has not reached a steady state (see below). The n = 2 modes last about 200 ms until a fast MHD event terminates the PEP phase. The electron temperature oscillations are in phase with the poloidal field oscillations for the n = 3 and n = 2 modes as expected for rotating magnetic islands.

Fast Soft X-ray data (sampling at 200 kHz) allow determination of the mode numbers of the oscillations after the n = 1 event. The soft X-ray centroid radius, R_{SXR} = 3.30 m, indicates a large Shafranov shift. Detailed analysis reveals a (3,2) mode of small amplitude at r = 0.14 m and a (2,2) mode of large amplitude at r = 0.25 m. The effective relative amplitudes of the oscillations are plotted as a function of minor radius in Fig. 5.8. Taking into account the variation in the measured Shafranov shift, the rational surfaces are believed to be at R = 3.15 and 3.42 m for the (3,2) mode and R = 3.02 and 3.52 m for the (2,2) mode. This shows that the shear is negative in the central region of the plasma. The error in the allocation of the

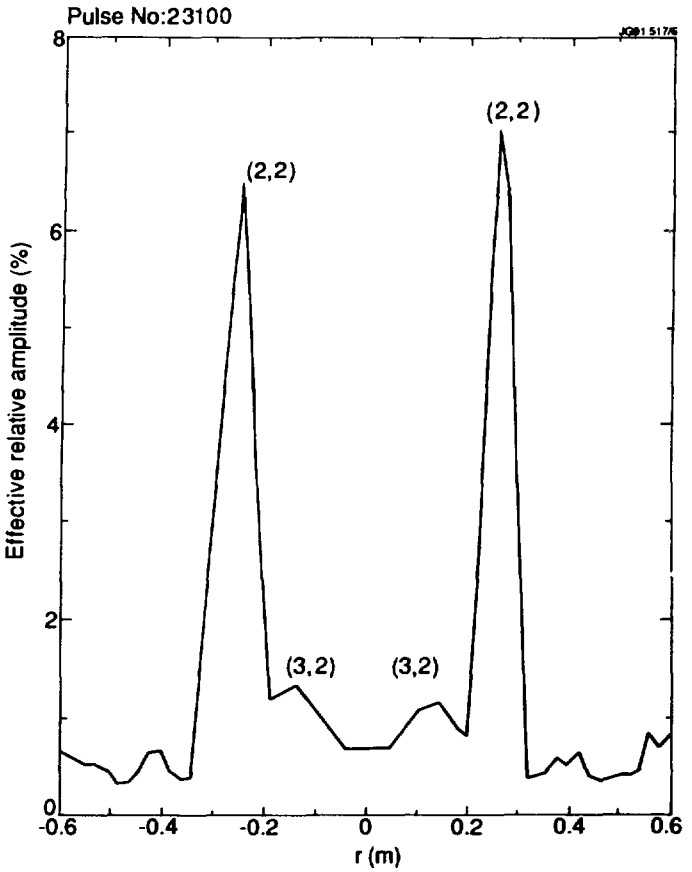

Fig. 5.8 The effective relative amplitude of soft X-ray oscillations associated with rotating MHD modes versus horizontal minor radius as determined from rotational tomography. The corresponding mode numbers are indicated in the figure.

maximum amplitude of a mode is typically the spacing between two diodes, which is of the order of 0.05 m. The radial displacement of the (2,2) and (3,2) modes has a maximum of about 0.05 m and extends over around 0.15 m of the plasma.

The positions of the rational surfaces deduced from the soft X-ray measurements after the n = 1 event are used as additional constraints on the plasma equilibrium calculated by the IDENTD code [Blum-90]. The equilibrium identification is done by minimizing a cost function that evaluates the deviation between simulated and observed measurements with the constraint of the Grad-Shafranov equation. IDENTD accommodates measurements of 14 flux loops and 18 pick-up coils at the vacuum vessel, the plasma current, the diamagnetic signal, the total pressure and safety factor at discrete points. The magnetic flux at the position of the flux loops is used directly as a boundary condition for the Grad-Shafranov equation and the total plasma current I_p is equal to the surface integral of the current density. All other quantities are fitted via minimization of the cost function. The total pressure is approximated by $p = \alpha p_e$ with the

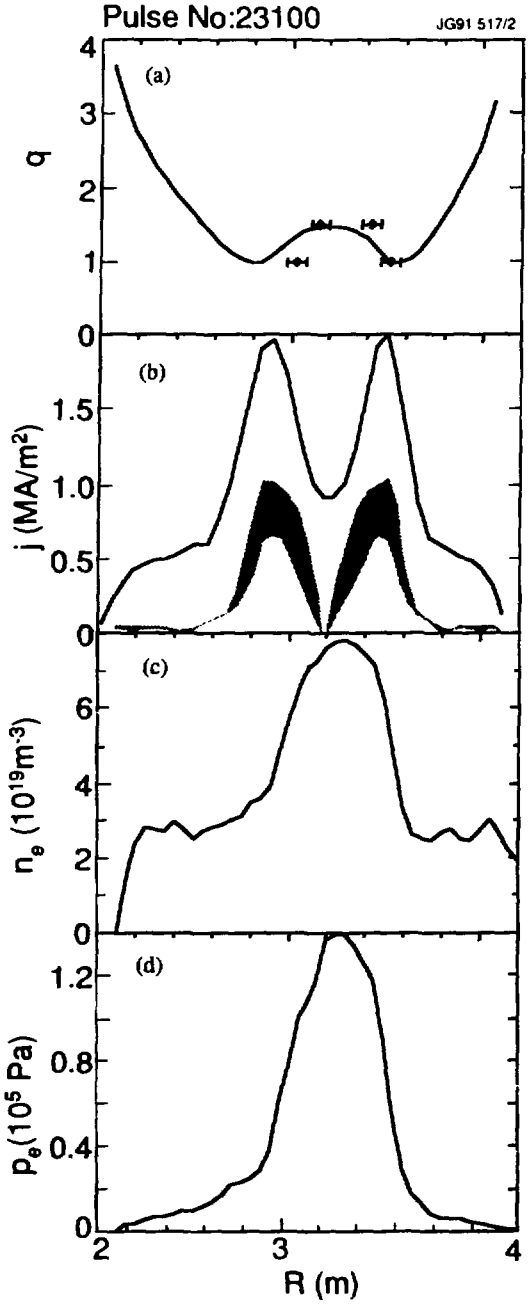

Fig. 5.9 Computed and measured profiles for Pulse No. 23100 at t = 6.605 s: (a) a q-profile calculated using IDENTD and rational q-values determined from soft X-ray data analysis; (b) current density profile, averaged over the flux surfaces, obtained from IDENTD and bootstrap current contribution to the total current. The indicated shaded area reflects the uncertainty in the bootstrap current calculated from the local gradients of the measured LIDAR density and temperature profiles; (c) LIDAR electron density profile; (d) LIDAR electron pressure profile.

constant factor α of the order of 2 and p_e is the electron pressure from LIDAR (see Fig. 5.9d). The electron temperature T_e is approximately equal to the ion temperature T_i as shown in Fig. 5.5. The remaining uncertainty on the pressure is taken into account by choosing a low weight in the cost function.

The calculated q-profile is shown in Fig. 5.9a. The discrepancy between the q-profile and the positions of the rational surfaces deduced from the observed mode activity on the high field side is partly due to a convergence problem of the algorithm when an attempt is made to enforce better agreement with the measurements. In addition, the flux surfaces are assumed to be concentric ellipses (i.e. in-out symmetric) in the soft X-ray reconstruction used to determine the island positions, whereas the q-profile is asymmetric because of the large Shafranov shift. The soft X-

ray centroid radius is R_{SXR} = 3.30 m and the position of the maximum in the electron pressure is at R = 3.28 m (see Fig. 5.9d), both comparing fairly well with the magnetic axis radius calculated by IDENTD (R_{mag} = 3.21 m).

The current density j obtained from IDENTD computations is shown in Fig.5.9b. Note that the central current density is too low by about 20% from the value of q(0) shown in Fig. 5.9a: this is due to a numerical problem of the equilibrium code, when computing strongly hollow j-profiles. The innermost 'twin peaks' of the j-profile are correlated with the steep density gradients in the central region (see Fig. 5.9c). Fig. 5.9b also shows the bootstrap current contribution to the total current as computed from the LIDAR data [Hirs-88]. The radial position and amplitude of the calculated bootstrap current matches the deviation of the reconstructed current profile from a roughly parabolic profile having the same central current density.

5.5.4.4 Transport simulation of the PEP mode

The evolution of temperature, current and density profiles of Pulse No. 23100 has been simulated using a predictive time dependent 1-D transport code [Bouc-91] based on the critical temperature gradient model of plasma transport [Rebu-88]. The simulations provide insight into the formation of the region of negative shear and into the consequences for transport within this region.

The computation starts just before the injection of the first pellet at 4.75 s. A large region (about 40% of the minor radius) with slightly negative shear is created after the injection of the second and last pellet at 5 s by a combination of three factors: (i) the broad current and q-profiles in the early phase; (ii) the transient inversion of the temperature profile and consequently of the current profile by the pellet injection; (iii) a small bootstrap current driven mainly by the density gradient. The region of negative shear is maintained during the 1 second of ohmic heating and weak ICRF heating (about 1.5 MW). After the onset of additional power (10 MW ICRH and 2.5 MW NBI), the bootstrap current increases strongly producing a more hollow q-profile. Fig. 5.10a compares the simulated q-profile at 6.6 s with that obtained from IDENTD computations: there is a reasonable agreement, bearing in mind that the transport code is 1-D, with nested circular flux surfaces that take little account of elongation or shifts in the magnetic axis, which are considered elsewhere [Taro-91].

The calculated temperature and density profiles are in good agreement with the LIDAR profiles at 6.6 s (see Fig. 5.10b) and time variations of the central electron temperature (Fig.

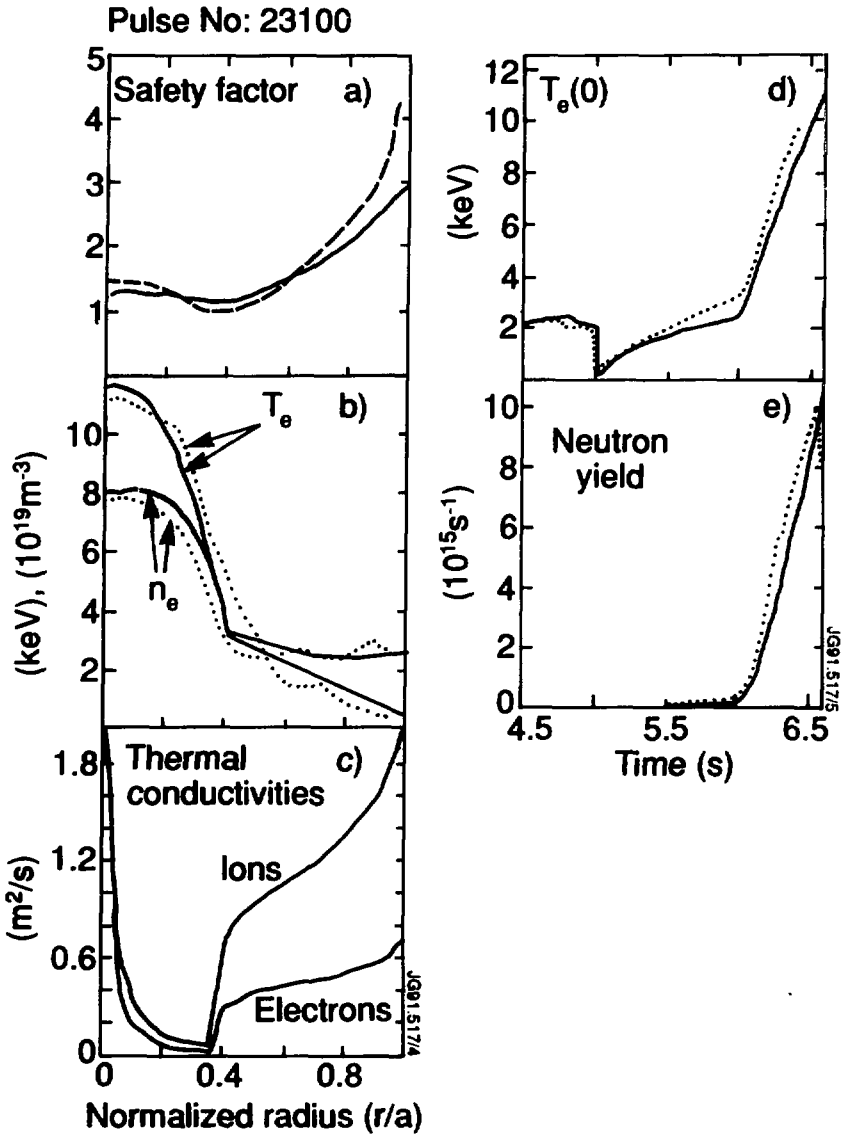

Fig. 5.10 Results of a PEP pulse simulation obtained with a time dependent 1-D transport code (solid curves). (a) The dashed curve is the q-profile calculated by IDENTD. (b) The dotted curves are the electron temperature T_e and density n_e profiles measured by LIDAR. (c) The transport is reduced within the region of negative shear as shown by the lower thermal conductivities. (d) The dotted line is the central electron temperature $T_e(0)$ measured by the Michelson interferometer as a function of time. (e) The dotted curve is the experimental neutron yield versus time.

5.10d) and neutron yield (Fig. 5.10e) are also well reproduced. In line with the critical electron temperature gradient model, it is necessary to reduce ion heat conduction and particle transport to neoclassical levels within the region of reversed shear. It is also necessary to reduce the electron transport to about 0.5 to 1 times ion neoclassical levels, that is, comparable to electron neoclassical levels, if poloidal variations in the electric potential are important [Stri-91]. The reduced transport inside the region of negative shear is shown in Fig. 5.10c by the lower thermal conductivities. Outside this region experimental data are well represented by the anomalous transport of the critical electron temperature gradient model. The conclusions of this simulation are similar to those obtained previously for other discharges with a predictive $1\frac{1}{2}$ D equilibrium-transport code [Taro-91].

5.5.4.5 Mode stability computation

To see how the n = 3,1,2 sequence of modes observed in shot 23100 compares with theory, a series of toroidal MHD calculations have been performed. For these calculations the resistive linear MHD code FAR [Char-90] is used. The equilibria are specified by defining the plasma boundary shape and the pressure and q profiles. The plasma boundary shape, determined from external magnetic measurements, has an elongation of 1.67 and a triangularity of 0.27. The pressure profile is obtained from the LIDAR data and its magnitude is adjusted to match the measured diamagnetic pressure to take into account

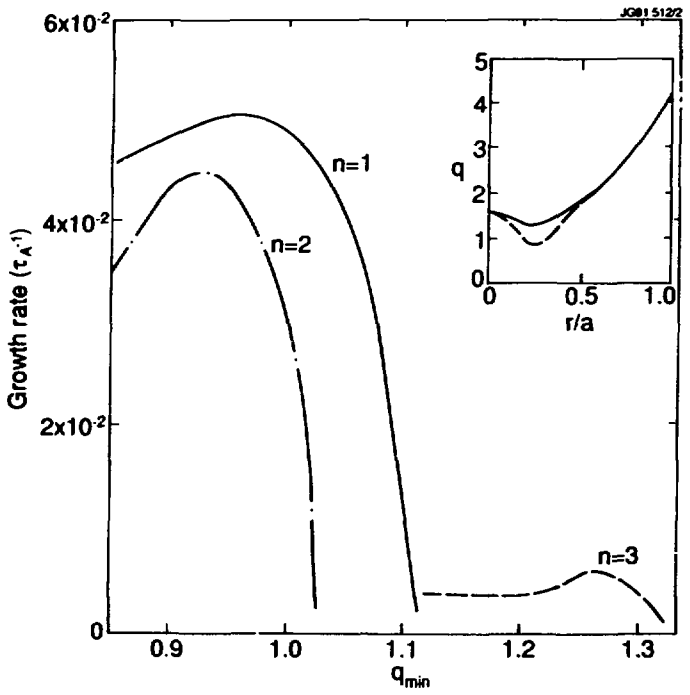

Fig. 5.11 The growth rate of instabilities with toroidal mode numbers n = 1, 2 and 3, computed for a range of q-profiles. Non-monotonic q-profiles are used with a q on axis of 1.6 and an off-axis minimum q_{min} at r/a = 0.3. An example of some of these q-profiles is shown in the inset.

the ion contribution. The average β_p is 0.29 during the n = 3 activity and is 0.38 during the n = 1 and 2 activity. The q-profile is constrained to match the experimental total plasma current, which essentially determines the edge q. The central q is fixed at 1.6 and a sequence of q-profiles are considered ranging from slightly to strongly non-monotonic, with a minimum q_{min} at r/a = 0.3, as shown in the inset in Fig. 5.11. This series of q-profiles is consistent with the experimental data discussed in section 5.5.4.3: the soft X-ray analysis indicates that the q-profile is inverted with q = 3/2 and q = 1 rational surfaces at r = 0.14 m and 0.25 m respectively after the fast (m,n) = (1,1) MHD event; in addition, the off-axis minimum of q is well above 1 just after pellet injection and decreases slowly towards a value below 1 as shown by the change from (m,n) = (4,3) to (2,2) activity. The results of the computation of the n = 1,2,3 growth rates (normalized to the poloidal Alfvén time $\tau_A \approx 0.2$ μs) are plotted in Fig. 5.11 versus q_{min}. These calculations are resistive with a magnetic Reynolds number (as defined in [Char-90]) of $s = 10^6$. The n = 1 and 2 modes are ideally unstable kinks as is the n = 3 mode for $q_{min} \lesssim 1.15$. It can be seen from Fig.5.11 that as q_{min} decreases the instabilities appear in the correct experimental sequence n = 3,1,2. A difficulty is that the n = 2 mode always grows more slowly than the n = 1 mode contrary to the experimental observation. It may be that a nonlinear simulation or the addition of terms not included in the MHD model could make the n = 2 mode dominant for $q_{min} \lesssim 1$. The very large growth rate of the n = 1 mode for $q_{min} \lesssim 1.1$ arises because the central poloidal beta [Buss-75] calculated from the LIDAR pressure profile is about 1.5, well above the critical value of around 0.3 when $q_{min} \approx 1$.

As the q-profile is not directly determined during the n = 3 activity, the sensitivity of the n = 3 growth rate to variations of q has been examined. For example, when raising the central q to 2, the dependence of the n = 3 growth rate on q_{min} is very similar to that shown in Fig. 5.11, though its maximum is 25% larger. It can thus be concluded that the n = 3 results are not very sensitive to details of the q-profile within the likely experimental range.

The growth rates of the n = 1, 2 and 3 modes have also been computed with the toroidal linear resistive MHD code CASTOR [Kern-91]. The results of the calculation confirm those obtained with the FAR code.

The question arises what is the effect of fast ions produced by ICRF heating on the stability of the m = 1 kink during the PEP mode. For Pulse No. 23100, the ICRF heating power is of the order of 10 MW and creates a significant fraction of fast ions; their total energy, calculated using a Fokker-Planck code, is of the order of 0.5 - 1.0 MJ, compared to about 6 MJ for the total plasma energy. The computed kinetic energy of the fast ions is in the range 100 - 200 keV, when the q = 1 surface appears in the plasma. The radial profile of their energy

density is found to have its maximum within 0.03 m of the magnetic axis and to be almost zero at 0.3 m from the magnetic axis. Thus, most of the fast ions are located within the q = 1 surface measured at 0.25 cm (see Section 5.5.4.3). Under these conditions, for the non-monotonic q-profile observed during the PEP mode, the fast ions should be destabilizing for the m = 1 kink, when q_{min} is just above 1 [Porc-91].

5.5.4.6 Topology of a rotating (m,n) = (1,1) mode

Fig. 5.12 shows the temporal behaviour of the electron temperature from the ECE radiometer (Pulse No. 23103). The oscillations at R = 3.61 m are of large amplitude and appear in a few channels only, indicating that they are localized radially, and show non-sinusoidal behaviour. They are located in a region where the electron temperature gradient is very steep. The toroidal mode number measured by the magnetic pick-up coils is n = 1 and the poloidal mode number is m ≈ 5 due to mode coupling. We have performed a correlation analysis between the temperature (from the ECE radiometer) and poloidal magnetic field oscillations, taking into account the toroidal separation of these diagnostics and the n = 1 symmetry of the

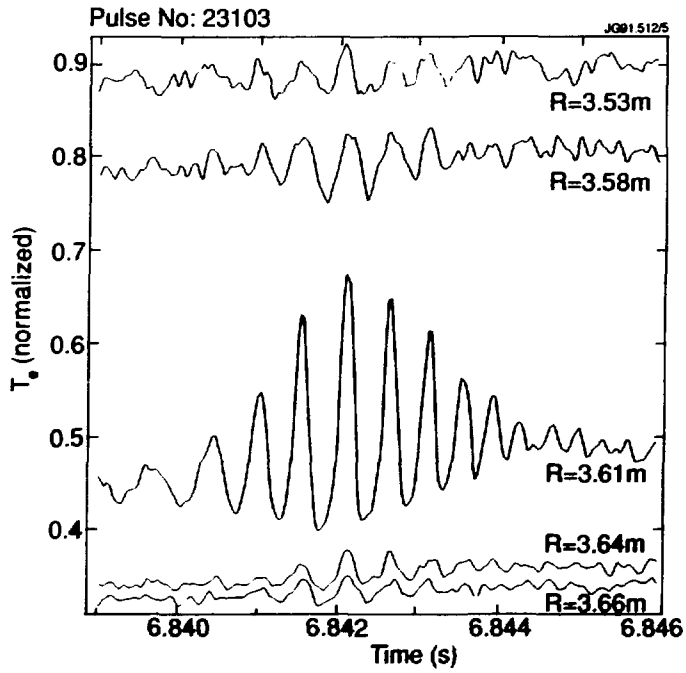

Fig. 5.12 Electron temperature versus time as measured by various channels of the ECE radiometer. Note the large amplitude of the oscillations at R = 3.61 m and their non-sinusoidal behaviour. Due to difficulties in the absolute calibration for this pulse, only normalized temperatures are shown. The relative (channel-to-channel) uncertainty in the profile is ± 5 %.

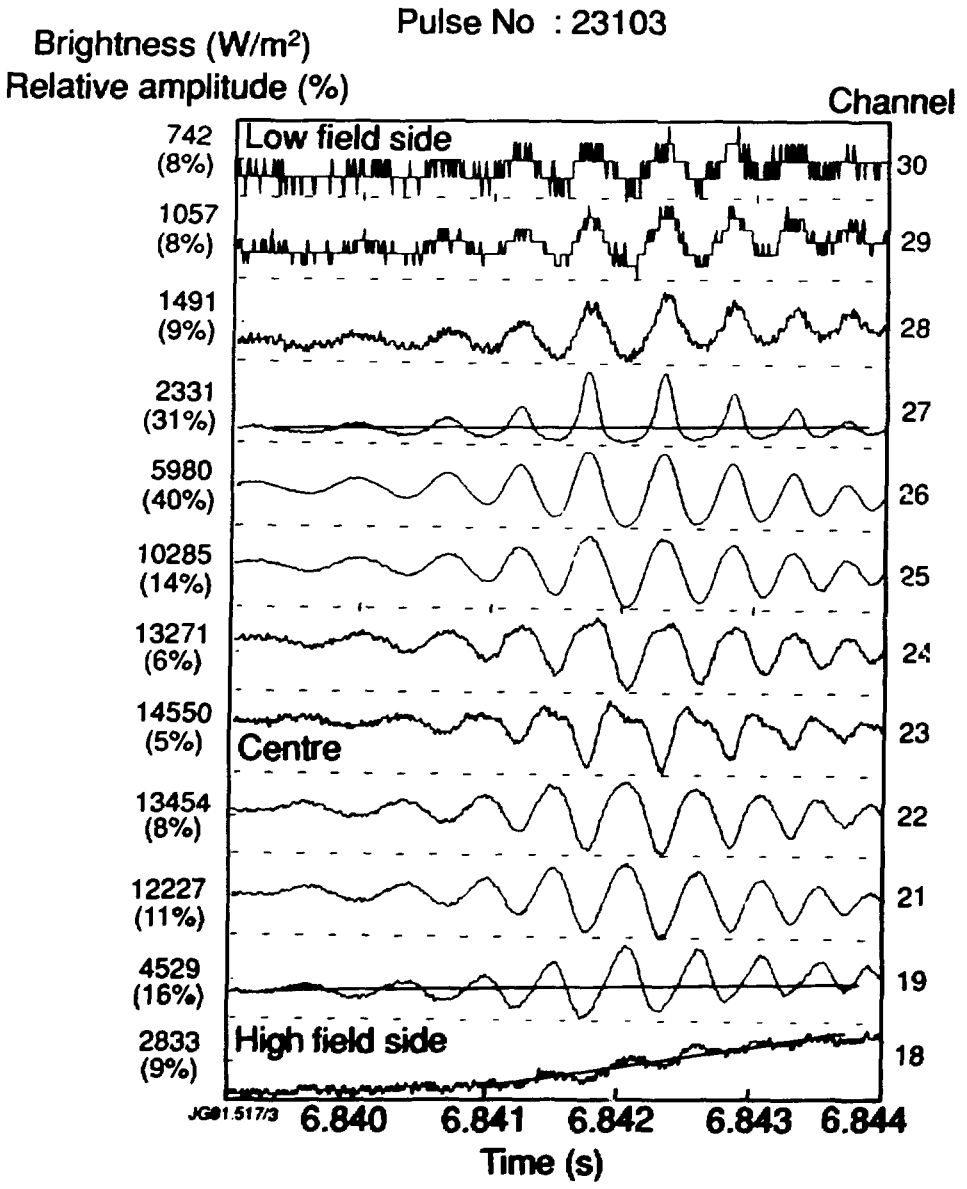

Fig. 5.13 Line integrated soft X-ray emissivity measured by the vertical camera showing the ballooning character of the (1,1) mode. The brightness measured in W/m² by each channel is given with the relative amplitude of the oscillation. The plasma centre at R = 3.30 m is viewed by channel 23. The (1,1) mode amplitude is larger on the low-field side (channel 27) than on the high-field side (intermediate between channels 18 and 19).

mode: the maximum in electron temperature corresponds to a maximum in poloidal field. From SXR fast data (200 kHz sampling) we find that the central dominant mode is (m,n) = (1,1). The temperature maximum corresponds to a maximum in soft X-ray emission. The mode rotates counter-clockwise toroidally, i.e. in the direction of the electron diamagnetic drift and opposite to the neutral beams. In addition, the measurements from the vertical camera displayed in Fig. 5.13 indicate that the mode has a ballooning character: it is stronger on the low field side (channel 27) than on the high field side (intermediate between channels 18 and 19). The soft X-ray centroid has a radius $R_{SXR} \approx 3.30$ m.

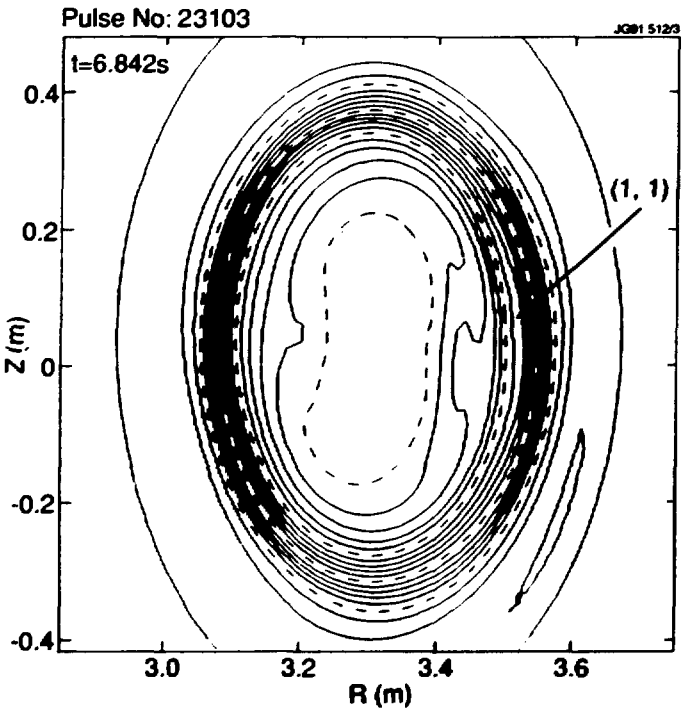

Fig. 5.14 Rotational tomographic reconstruction of the soft X-ray emissivity showing an (m,n) = (1,1) mode.

The soft X-ray rotational tomographic reconstruction (Fig. 5.14) displays the (1,1) mode at r ≈ 0.22 m. The rotating structure has a small poloidal extent and does not affect the core of the plasma. It corresponds to a radial displacement, which has a maximum of around 0.05 m and extends over about 0.1 m of the plasma. It could be interpreted as the O-point of a (1,1) island.

The soft X-ray measurements suggest the existence of another mode near the plasma centre (r ≈ 0.1 m), which has tentatively been identified as (m,n) = (2,1). A plasma equilibrium with a central value of q around 2 can indeed be obtained with the IDENTD code; so a (2,1) island cannot be excluded close to the magnetic axis.

Magnetic islands can be sustained by a current perturbation δj flowing inside. In this case, the core of the island with nested surfaces is expected to have a smaller poloidal extension

than the region surrounding the X-points of the separatrix, which is easily destroyed by chaos, since filaments carrying parallel current attract each other. From Ampère's law, it follows that the current perturbation δj inside the island is opposite to the main plasma current j when the shear q' is positive and in the same direction as j when q' is negative. If the current perturbation δj is due to a thermal instability inside the island, it depends on the electron temperature through the resistivity and Ohm's law. The resulting island is then colder than the surrounding plasma when q' is positive and warmer when q' is negative [Rebu-84]. It follows that the electron temperature oscillations associated with a rotating thermal island measured at a fixed location in the plasma are expected to be non-sinusoidal: for a 'hot' island, the maximum is of shorter duration than the minimum.

The non-sinusoidal behaviour of the oscillations observed by the ECE and soft X-ray diagnostics seems to suggest at first the (1,1) mode structure is a 'hot' island. This agrees with the existence of negative shear in the central region of the plasma as inferred above. However, the ballooning character of the (1,1) mode observed experimentally is not explained by the thermal island model [Rebu-84]. In addition, from the shear computed by IDENTD of $q' \approx -5$ m^{-1} and the relative temperature oscillation amplitude $\delta T_e/T_e \approx 0.5$ at the island position, the width calculated for a thermal island is about 0.5 m, much larger than that observed. Although there is a large uncertainty in the shear determination, this calculation suggests that the island could be strongly stabilized by some mechanism reducing its width such as bootstrap current in the region of negative shear.

There remains the difficulty that the ideal MHD internal kink should be violently unstable when the off-axis minimum of q is less that unity (see Fig. 5.11). Thus, if the (1,1) mode is a true island, the internal kink must be stabilized by some unidentified mechanism or by a nonlinear process taking into account the change in topology due to the presence of the island. Alternatively, the (1,1) mode might be a local distortion of the flux surfaces with the minimum in q just below the marginal value for the $n = 1$ mode destabilization (≈ 1.1 for the case shown in Fig 5.11). However, the topology of the nonlinearly saturated state computed in [Holm-88] does not evidently explain the observation of a localized hot spot on the low field side.

5.5.5 Conclusions

MHD modes occurring during the Pellet Enhanced Performance (PEP) mode have been studied in this paper. Analysis of soft X-ray data has led to the determination of the position of rational q-surfaces, showing that the shear is negative in the central region of the plasma. In a particular pulse, (m,n) = (3,2) and (2,2) modes are found at radii r = 0.14 and 0.25 m respectively. The measured positions of the q = 1 and q = 1.5 surfaces are used as additional constraints to the plasma equilibrium which shows a Shafranov shift in reasonable agreement with that obtained from the soft X-ray measurements (about 0.20 m). The calculated current profile displays large off-axis peaks consistent with the bootstrap current computed from the measured electron density and temperature profiles. A predictive time-dependent 1-D transport code shows that the bootstrap current is maintained by the improved confinement in the central region of the plasma where the shear is negative: the ion transport coefficients are reduced to their neoclassical values in line with the critical temperature gradient model; electron transport coefficients also have to be reduced within this region and in this case are set to about 0.5 to 1 times ion neoclassical levels.

During the PEP phase fast (m,n) = (1,1) MHD events often occur close to the maximum in the neutron rate. These events are usually preceded by n = 3 modes and followed by dominant n = 2 modes. This sequence of modes (n = 3, 1, 2) appears in calculations obtained with two different toroidal linear MHD codes assuming a non-monotonic q-profile with an off-axis minimum q_{min} which is decreasing from above to below 1. However, the n = 2 mode is always less unstable than the n = 1 mode, contrary to the experiment. The large growth rate calculated for the n = 1 mode for $q_{min} \lesssim 1.1$ is due to the high value of the central poloidal beta of 1.5 characteristic of the PEP mode. A rotating (m,n) = (1,1) mode has been studied in detail: it has the appearance of a localized hot spot ballooning at the low field side of the plasma. This hot spot has some characteristics of a 'hot' island consistent with the presence of negative shear in the plasma core. Both experimental observations (n = 2 mode after the (1,1) MHD events and hot spot) suggest that the internal kink is strongly stabilized by some mechanism or by a nonlinear process taking into account the change in topology due to the presence of islands.

5.5.6 Acknowledgements

The authors are very grateful to B. Balet, H. de Blank, C.D. Challis, S. Corti, A.E. Costley, J. Ellis, J. Fessey, G. Fishpool, R. Gill, N. Gottardi, M. von Hellermann, B. Keegan, E. Lazzaro, P. Morgan, C. Nardone, G. Neill, H. Oosterbeek, J. O'Rourke, D. Pasini, F. Porcelli, C. Sack, G. Sadler, F.C. Schüller, G. Sips, A. Taroni, J. Wesson and S. Wolfe for providing experimental data, helping with data analysis or for fruitful discussions. The authors acknowledge the support of the entire JET Team. Part of this work was performed under the Euratom-FOM Association agreement, with financial support from NWO and Euratom.

References

[Abra-65] M. ABRAMOWITZ, I.A. STEGUN, *Handbook of mathematical functions*, National Bureau of Standards, 4th printing (1965)

[Alla-86] F. ALLADIO, F. CHRISANTI, *Analysis of MHD equilibria by toroidal multipolar expansions*, Nucl. Fusion **26** (1986) 1143

[Bart-86] D.V. BARTLETT, H. BINDSLEV, M. BRUSATI, D.J. CAMPBELL, A.E. CORDEY, S.E. KISSEL, N.J. LOPES CARDOZO, B.Ph. VAN MILLIGEN, P.E. STOTT, *Investigation of electron temperature profile behaviour in JET*, in Contr. Fusion and Plasma Phys. (Proc. 13th Eur. Conf. Schliersee, 1986), Vol. 10C, Part I, European Physical Society (1986) I-236

[Batc-67] G.K. BATCHELOR, *An Introduction to Fluid Dynamics*, Cambridge University Press (1967)

[Bate-80] G. BATEMAN, *MHD Instabilities*, The MIT Press, Cambridge, Massachusetts (1980)

[Bick-87] R.J. BICKERTON, A. TARONI, M.L. WATKINS, J. WESSON, *Comparison between experiment and theory*, Phil. Trans. R. Soc. Lond. A322 (1987) 173

[Bitt-86] J.A. BITTENCOURT, *Fundamentals of plasma physics*, Pergamon Press, Oxford, England (1986)

[Blum-90] J. BLUM, E. LAZARRO, J. O'ROURKE, B. KEEGAN, Y. STEPHAN, *Problems and methods of self-consistent reconstruction of tokamak equilibrium profiles from magnetic and polarimetric measurements*, Nucl. Fusion **30**, (1990) 1475

[Bouc-91] D. BOUCHER, P.-H. REBUT, M.L. WATKINS, *The simulation of energy and particle transport, heat and density pulse propagation and H-mode confinement in JET and a reactor*, in Contr. Fusion and Plasma Phys. (Proc. 18th Eur. Conf. Berlin, 1991), Vol. 15C, Part I, European Physical Society (1991) I-177

[Braa-86a] B.J. BRAAMS, *Computational studies in tokamak equilibrium and transport*, Thesis (1986)

[Braa-86b] B.J. BRAAMS, W. JILGE, K. LACKNER, *Fast determination of plasma parameters through Function Parametrization*, Nucl. Fusion **26** (1986) 699

[Brag-65] S.I. BRAGINSKII, *Transport processes in a plasma*, Reviews of Plasma Physics, **1** (1965) 205

[Brau-83] K. BRAU, M. BITTER, R.J. GOLDSTON, D. MANOS, K. MCGUIRE, S. SUCKEWER, *Plasma rotation in the PDX tokamak,* Nucl. Fusion **23** (1983) 1643

[Brus-84] M. BRUSATI, J.P. CHRISTIANSEN, J.G. CORDEY, K. JARRETT, E. LAZZARO, R.T. ROSS, *Analysis of magnetic measurements in a tokamak,* Computer Physics Reports **1** (1984) 345

[Buss-75] M.N. BUSSAC, R. PELLAT, D. EDERY, J.L. SOULE, *Internal kink modes in toroidal plasmas with circular cross sections,* Phys. Rev. Letters **35** (1975) 1638

[Camp-87] D.J. CAMPBELL, A. EDWARDS, R. GILL, R. GRANETZ, N.J. LOPES CARDOZO, N.J., B.Ph. VAN MILLIGEN, H. TAMMEN, B.J.D. TUBBING, A. WELLER, J.A. WESSON, *Studies of the sawtooth instability in JET,* Bull. Am. Phys. Soc. **32** (1987) 1838

[Char-90] L.A. CHARLTON, J.A. HOLMES, V.E. LYNCH, B.A. CARRERAS, T.C. HENDER, *Compressible linear and nonlinear resistive MHD calculations in toroidal geometry,* Journal of Comp. Phys. **86** (1990) 270

[Desh-83] G.N. DESHKO, T.G. KILOVATAYA, Yu.K. KUZNETSOV, V.N. PYATOV, I.V. YASIN, *Determination of the plasma column shape in a tokamak from magnetic measurements,* Nucl. Fusion **23** (1983) 1309

[Edwa-86] A.W. EDWARDS, H.-U. FAHRBACH, R.D. GILL, R. GRANETZ, E. OORD, G. SCHRAMM, S. TSUJI, A. WELLER, D. ZASCHE, *JET soft X-ray diode array diagnostic,* Rev. Sci. Instrum. **57** (1986) 2142

[Fene-84] W. FENEBERG, K. LACKNER, P. MARTIN, *Fast control of the plasma surface,* Comp. Phys. Comm. **31** (1984) 143

[Fess-87] J.A. FESSEY, C.W. GOWERS, C.A.J. HUGENHOLTZ, K. SLAVIN, *Plasma electron density measurements from the JET 2 mm wave interferometer,* J. Phys. E: Sci. Instrum. **20** (1987) 169

[Fock-32] V.A. FOCK, Fiz. Zh. Sovietunion **1** (1932) 215

[Frei-87] J.P. FREIDBERG, *Ideal Magnetohydrodynamics,* Plenum Press, New York (1987)

[Furt-86] H.P. FURTH, *Enhancement of confinement in tokamaks,* Plasma Physics and Controlled Fusion, **28** (1986) 1305.

[Goed-84] J.P. GOEDBLOED, *Some remarks on computing axisymmetric equilibria,* Computer Phys. Commun., **2&3** (1984) 123

[Grad-58] H. GRAD, H. RUBIN, *Hydromagnetic equilibria and force-free fields,* in Proceedings of the second United Nations International Conference on the peaceful uses of atomic energy, United Nations, Geneva, **31** (1958) 190

[Gran-88] R.S. GRANETZ, P. SMEULDERS, *X-ray tomography on JET*, Nucl. Fusion **28** (1988) 457

[Hakk-87] S.P. HAKKARAINEN, J.P. FREIDBERG, *Reconstruction of vacuum flux surfaces from diagnostic measurements in a tokamak*, MIT, Cambridge (USA), PFC/RR-87-22 (1987)

[Harl-89] T.R. HARLEY, D.A. BUCHENAUER, J.W. COONROD, K.M. MCGUIRE, *TFTR Mirnov coil analysis with toroidal effects at plasma startup*, Nucl. Fusion **29** (1989) 771

[Hint-76] F.L. HINTON, R.D. HAZELTINE, Reviews of Modern Physics, **48** (1976) 239

[Hirs-88] S.P. HIRSCHMANN, Physics of Fluids **31** (1988) 3150

[Hoff-88] F. HOFFMANN, G. TONETTI, *Tokamak equilibrium reconstruction using Faraday rotation measurements*, Nucl. Fusion **28** (1988) 1871

[Holm-88] J.A. HOLMES, B.A. CARRERAS, L.A. CHARLTON, V.E. LYNCH, R.J. HASTIE, T.C. HENDER, *Nonlinear evolution of the internal kink mode in toroidal geometry for shaped tokamak plasmas*, Phys. Fluids **31** (1988) 1202

[Hugo-91a] M. HUGON, B. BALET, J.P. CHRISTIANSEN, A. EDWARDS, G. FISHPOOL, C.G. GIMBLETT, N. GOTTARDI, R.J. HASTIE, P. LOMAS, B.Ph. VAN MILLIGEN, G. NEILL, J. O'ROURKE, G. SIPS, P. SMEULDERS, P.M. STUBBERFIELD, T. TAGLE, S. WOLFE, *Current rise studies*, in Contr. Fusion and Plasma Phys. (Proc. 18th Eur. Conf. Berlin, 1991), Vol. 15C, Part I, European Physical Society (1991) I-41

[Hugo-91b] M. HUGON, B.Ph. VAN MILLIGEN, P. SMEULDERS, L. APPEL, D. BARTLETT, D. BOUCHER, A. EDWARDS, L. ERIKSSON, C. GOWERS, T.C. HENDER, G. HUYSMANS, J. JACQUINOT, P. KUPSCHUS, L. PORTE, P.H. REBUT, D. START, F. TIBONE, B.J.D. TUBBING, M. WATKINS, W. ZWINGMANN, *Shear reversal and MHD activity during Pellet Enhanced Performance plasmas in JET*, Submitted to Nucl. Fusion 1991

[Huys-91] G.T.A. HUYSMANS, T.C. HENDER, O.J. KWON, J.P. GOEDBLOED, E. LAZZARO, P. SMEULDERS, *MHD stability analysis of high-β JET discharges*, Accepted for publication in Plasma Physics and Contr. Nucl. Fusion 1991

[Kern-91] W. KERNER, S. POEDTS, J.P. GOEDBLOED, G.T.A. HUYSMANS, B. KEEGAN, E. SCHWARZ, *Computing the damping and destabilization of global Alfvén waves in tokamaks*, in Contr. Fusion and Plasma Phys. (Proc. 18th Eur. Conf. Berlin, 1991), Vol. 15C, Part IV, European Physical Society (1991) IV-89

[Kups-91] P. KUPSCHUS, B. BALET, D. BARTLETT, D. BOUCHER, C. CHALLIS, G. CORRIGAN, S. CORTI, A. EDWARDS, L.G. ERIKSSON, R. GILL, C. GORMEZANO, C. GOWERS, H. HOLM, M. HUGON, J. JACQUINOT, K. LAWSON, H. MORSI, G. NEILL, H.

OOSTERBEEK, J. O'ROURKE, D. PASINI, L. PORTE, F. RIMINI, G. SADLER, G. SCHMIDT, G. SIPS, P. SMEULDERS, D. START, P.M. STUBBERFIELD, A. TARONI, F. TIBONE, B.J.D. TUBBING, M. VON HELLERMANN, B.Ph. VAN MILLIGEN, W. ZWINGMANN, *High thermonuclear yield on JET by combining enhanced plasma performance of ICRH-heated, pellet-peaked density profiles with H-mode confinement*, in Contr. Fusion and Plasma Phys. (Proc. 18th Eur. Conf. Berlin, 1991), Vol. 15C, Part I, European Physical Society (1991) I-1

[Lack-76] K. LACKNER, *Computation of ideal MHD equilibria*, Comput. Phys. Comm. **12** (1976) 33

[Lamm-91] A.C.A.P. VAN LAMMEREN, J.C.M. TIMMERMANS, G.M.D. HOGEWEIJ, S.K. KIM, A.J.H. DONNÉ AND THE RTP TEAM, *The effects of MHD-activity on the density in the RTP tokamak*, in Contr. Fusion and Plasma Phys. (Proc. 18th Eur. Conf. Berlin, 1991), Vol. 15C, Part II, European Physical Society (1991) II-73

[Lao-81] L.L. LAO, S.P. HIRSCHMANN, R.M. WIELAND, *Variational moment solutions to the Grad-Shafranov equation*, Phys. Fluids **24** (1981) 1431

[Lao-84] L.L. LAO, *Variational moment method for computing magnetohydrodynamic equilibria*, Comp. Phys. Comm. **31** (1984) 201

[Lao-85] L.L. LAO, H.St. JOHN, R.D. STAMBAUGH, A.G. KELLMAN, W. PFEIFFER, *Reconstruction of current profile parameters and plasma shapes in tokamaks*, Nucl. Fusion **25** (1985) 1611

[Lee-81] D.K. LEE, Y.-K.M. PENG, *An approach to rapid plasma shape diagnostics in tokamaks*, J. Plas. Phys. **25**, part 1 (1981) 161

[Luxo-82] J.L. LUXON, B.B. BROWN, *Magnetic analysis of non-circular cross section tokamaks*, Nucl. Fusion **22** (1982) 813

[McCa-86] P.J. MCCARTHY, M.C. SEXTON, *Plasma profile recovery by function parametrization*, Max-Planck Institut für Plasmaphysik, Report IPP 5/12 (1986)

[Mill-88] B. Ph. VAN MILLIGEN, N.J. LOPES CARDOZO, *Tokamak equilibrium determination through function parametrization*, in Contr. Fusion and Plasma Phys. (Proc. 15th Eur. Conf. Dubrovnik, 1988), Vol. 12B, Part I, European Physical Society (1988) I-318

[Mill-89] B.Ph. VAN MILLIGEN, *Expansion of the flux and current density in toroidal systems and applications in fusion research*, in Contr. Fusion and Plasma Phys. (Proc. 16th Eur. Conf. Venezia, 1989), Vol. 13B, Part I, European Physical Society (1989) I-459

[Mill-90a] B.Ph. VAN MILLIGEN, *Exact relations between multipole moments of the flux and moments of the toroidal current density in tokamaks*, Nucl. Fusion **30** (1990) 157

[Mill-90b] B.Ph. VAN MILLIGEN, H. SOLTWISCH, N.J. LOPES CARDOZO, *Application of Function Parametrization to the analysis of polarimetry and interferometry data at TEXTOR*, in Contr. Fusion and Plasma Phys. (Proc. 17th Eur. Conf. Amsterdam, 1990), Vol. 14B, Part IV, European Physical Society (1990) IV-1660

[Mill-91a] B.Ph. VAN MILLIGEN, H. SOLTWISCH, N.J. LOPES CARDOZO, *Application of Function Parametrization to the analysis of polarimetry and interferometry data at TEXTOR*, Nucl. Fusion **31** (1991) 309

[Mill-91b] B.Ph. VAN MILLIGEN, N.J. LOPES CARDOZO, *Function Parametrization: a fast inverse mapping method*, Accepted for publication in Comp. Phys. Comm. 1991

[Mors-53] P.M. MORSE, H. FESHBACH, *Methods of Theoretical Physics*, McGraw-Hill, New York (1953)

[Mukh-71] V.S. MUKHATOV, V.D. SHAFRANOV, *Plasma equilibrium in a tokamak*, Nucl. Fusion **11** (1971) 606

[Naga-89] M. NAGAMI AND JT-60 TEAM, *Recent results in JT-60 experiments*, Plasma Physics and Controlled Fusion, **31** (1989) 1597.

[Odaj-86] K. ODAJIMA, A. FUNAHASHI, K. HOSHINO, *et al., Confinement studies of additionally heated plasma in the JFT-2M tokamak*, in Plasma Physics and Controlled Nuclear Fusion Research 1986 (Proc. 11th Int. Conf. Kyoto, 1986), Vol. 1, IAEA, Vienna (1987) 151.

[ORou-88] J. O'ROURKE, J. BLUM, J.G. CORDEY, A. EDWARDS, N. GOTTARDI, B. KEEGAN, E. LAZARRO, G. MAGYAR, Y. STEPHAN, P. STUBBERFIELD, D. VÉRON, D. ZASCHE, *Polarimetric measurements of the q-profile*, in Contr. Fusion and Plasma Phys. (Proc. 15th Eur. Conf. Dubrovnik, 1988), Vol. 12B, Part I, European Physical Society (1991) I-155

[Polm-90] R. POLMAN, R. VAN ANDEL, R. BOSMAN, R. DAMSTRA, D.F. DA CRUZ JR., B. DE GROOT, C.A.J. HUGENHOLTZ, J.J. KONING, W. KOOIJMAN, O.G. KRUYT, J. LOK, B.Ph. VAN MILLIGEN, A.A.M. OOMENS, F.C. SCHÜLLER, F.M.A. SMITS, P.H.M. SMEETS, J. STAKENBORG, A.J.H. TIELEMANS, C.J. TITO, A.G.A. VERHOEVEN, E. WESTERHOF, *ECRH sustained breakdown plasmas in RTP*, in Contr. Fusion and Plasma Phys. (Proc. 17th Eur. Conf. Amsterdam, 1990), Vol. 14B, Part III, European Physical Society (1990) III-1121

[Porc-91] F. PORCELLI, *private communication*

[Port-91] L. PORTE, D.V. BARTLETT, D.J. CAMPBELL, A.E. COSTLEY, *First results with the upgraded ECE heterodyne radiometer on JET,* in Contr. Fusion and Plasma Phys. (Proc. 18th Eur. Conf. Berlin, 1991), Vol. 15C, Part IV, European Physical Society (1991) IV-357

[Rebu-84] P.-H. REBUT, M. HUGON, *Thermal instability and disruptions in a tokamak,* in Plasma Physics and Controlled Nuclear Fusion Research 1984 (Proc. 10th Int. Conf. London, 1984), Vol. 2, IAEA, Vienna (1985) 197

[Rebu-86a] P.-H. REBUT AND JET TEAM, *JET latest results and future prospects,* in Plasma Physics and Controlled Nuclear Fusion Research 1986 (Proc. 11th Int. Conf. Kyoto, 1986), Vol. 1, IAEA, Vienna (1987) 31

[Rebu-86b] P.-H. REBUT, M. BRUSATI, M. HUGON, P.P. LALLIA, *Magnetic islands and chaos induced by heat flow,* in Plasma Physics and Controlled Nuclear Fusion Research 1986 (Proc. 11th Int. Conf. Kyoto, 1986), Vol. 2, IAEA, Vienna (1987) 187.

[Rebu-88] P.-H. REBUT, P. LALLIA, M.L. WATKINS, *The critical temperature gradient model of plasma transport: applications to JET and future tokamaks,* in Plasma Physics and Controlled Nuclear Fusion Research 1988 (Proc. 12th Int. Conf. Nice, 1988), Vol. 2, IAEA, Vienna (1989) 191.

[Rebu-90] P.-H. REBUT, M. HUGON, *Magnetic turbulence self-sustainment by finite Larmor radius effect,* Submitted for publication in Plasma Physics and Controlled Fusion, 1990

[Salz-88] H. SALZMANN, J. BUNDGAARD, A. GADD, C. GOWERS, K.B. HANSEN, K. HIRSCH, P. NIELSEN, K. REED, C. SCHRÖDTER, K. WEISBERG, *The LIDAR Thomson scattering diagnostic on JET,* Rev. Scientific Instr. **59** (1988) 1451

[Schm-86] G.L. SCHMIDT, S.L. MILORA, V. ARUNASALAM, *et al., Pellet injection results during TFTR ohmic and neutral beam heating experiments,* in Plasma Physics and Controlled Nuclear Fusion Research 1986 (Proc. 11th Int. Conf. Kyoto, 1986), Vol. 1, IAEA, Vienna (1987) 171

[Schm-88] G.L. SCHMIDT AND JET TEAM, *Heating of peaked density profiles produced by pellet injection in JET,* in Plasma Physics and Controlled Nuclear Fusion Research 1988 (Proc. 12th Int. Conf. Nice, 1988), Vol. 1, IAEA, Vienna (1989) 215

[Schü-91] F.C. SCHÜLLER, C.J. BARTH, A.J.H. DONNÉ, D. FERREIRA DA CRUZ, B. DE GROOT, P.C. VAN HAREN, S.H. HEIJNEN, G.M.D. HOGEWEIJ, C.A.J. HUGENHOLTZ, L.C. INGESSON, S.K. KIM, J.A. KONINGS, W. KOOIJMAN, A.C.A.P. VAN LAMMEREN,

K.W. LEE, J. LOK, N.J. LOPES CARDOZO, A.C. MAAS, B.Ph. VAN MILLIGEN, A.A.M. OOMENS, R.W. POLMAN, B.C. SCHOKKER, F.M.A. SMITS, P.H.M. VAESSEN, A.G.A. VERHOEVEN, M. VERRECK, *Experimental observations of ohmic and ECR heated tokamak plasmas in RTP*, in Contr. Fusion and Plasma Phys. (Proc. 18th Eur. Conf. Berlin, 1991), Vol. 15C, Part I, European Physical Society (1991) I-121

[Seng-85] S. SENGOKU, M. NAGAMI, M. ABE, *et al., Improvement of energy confinement time by continuous pellet fuelling in beam-heated Doublet III limiter discharges*, Nucl. Fusion **25** (1985) 1475

[Shaf-58] V.D. SHAFRANOV, *On magnetohydrodynamical equilibrium configurations*, Sov. Phys. JETP. **6** (1958) 545; J. Exper. Theor. Phys. (USSR) **33** (1957) 710

[Smeu-83] P. SMEULDERS, *A fast plasma tomography routine with second-order accuracy and compensation for spatial resolution*, Rep. IPP-2/252, Max Planck Institut für Plasmaphysik Garching (1983)

[Smeu-91] P. SMEULDERS, D. BARTLETT, A. EDWARDS, G. FISHPOOL, T.C. HENDER, M. HUGON, B.Ph. VAN MILLIGEN, C. NARDONE, G. NEILL, L. PORTE, S. WOLFE, W. ZWINGMANN, *MHD studies in JET*, in Contr. Fusion and Plasma Phys. (Proc. 18th Eur. Conf. Berlin, 1991), Vol. 15C, Part II, European Physical Society (1991) II-53

[Solt-80] H. SOLTWISCH, *Combined interferometric and polarimetric diagnostics for TEXTOR*, Report KFA Jülich 1638 (1980)

[Solt-83] H. SOLTWISCH, *Plasma position detection and control in the TEXTOR tokamak by means of a far-infrared interferometer/polarimeter*, Nucl. Fusion **23** (1983) 1681

[Solt-86a] H. SOLTWISCH, *Current distribution measurement in a tokamak by FIR polarimetry (invited)*, Rev. Sci. Instrum. **57** (1986) 1939

[Solt-86b] H. SOLTWISCH, *Interferometry and Faraday rotation on tokamaks, Part I: Experimental techniques; Part II: Data analysis*, Proc. course and workshop on basic and advanced plasma diagnostic techniques, Varenna, EUR 10797 EN, Vol. II (1986) 343

[Stri-91] T.E. STRINGER, *Inclusion of poloidal potential variation in neoclassical transport*, Phys. Fluids **B3** (1991) 981

[Taro-88] A. TARONI, B. BALET, G. BETELLO, *et al., Global power balance and local heat transport in JET*, in Plasma Physics and Controlled Nuclear Fusion Research 1988 (Proc. 12th Int. Conf. Nice, 1988), Vol. 1 (1989) 367

[Taro-91] A. TARONI, Ch. SACK, E. SPRINGMANN, F. TIBONE, *Local transport analysis in L and H regimes,* in Contr. Fusion and Plasma Phys. (Proc. 18th Eur. Conf. Berlin, 1991), Vol. 15C, Part I, European Physical Society (1991) I-181

[Tubb-85] B.J.D. TUBBING, E. BARBIAN, D.J. CAMPBELL, C.A.J. HUGENHOLTZ, R.M. NIESTADT, Th. OYEVAAR, H.W. PIEKAAR, *A twelve-channel grating polychromator for measurement of electron temperature in JET,* in Contr. Fusion and Plasma Phys. (Proc. 12th Eur. Conf. Budapest, 1985), Vol. 9F, Part II, European Physical Society (1985) II-215

[Tubb-91] B.J.D. TUBBING, B. BALET, D.V. BARTLETT, C.D. CHALLIS, S. CORTI, R.D. GILL, C. GORMEZANO, C. GOWERS, M. VON HELLERMANN, M. HUGON, J.J. JACQUINOT, H. JAECKEL, P. KUPSCHUS, K. LAWSON, H. MORSI, J. O'ROURKE, D. PASINI, F. RIMINI, G. SADLER, G.L. SCHMIDT, D. START, P. STUBBERFIELD, A. TANGA, F. TIBONE, *H mode confinement in JET with enhanced performance by pellet-peaked density profiles,* Nucl. Fusion **31** (1991) 839

[Webs-74] J.T. WEBSTER, R.F. GUNST, R.L. MASON, *Latent Root Regression Analysis,* Technometrics, Vol. 16, No. 4 (1974) 513

[Wess-78] J.A. WESSON, *Hydromagnetic stability of tokamaks*, Nucl. Fusion **18** (1978) 87

[Wess-87] J.A. WESSON, *Tokamaks*, Clarendon Press, Oxford (1987)

[Wess-89] J.A. WESSON, R.D. GILL, M. HUGON, *et al., Disruptions in JET*, Nucl. Fusion **29** (1989) 641

[Wind-72] H. WIND, *Function parametrization,* in Proceedings of the CERN Computing and Data Processing School, CERN 72-21 (1972) 53

[Wind-84] H. WIND, (a) *Principal component analysis and its application to track finding,* (b) in *Formulae and Methods in Experimental Data Evaluation*, Vol. 3, European Physical Society, Geneva (1984).

[Woot-79] A.J. WOOTTON, *Measurements of plasma shape in a tokamak,* Nucl. Fusion **19** (1979) 987

[Zakh-73] L.E. ZAKHAROV, V.D. SHAFRANOV, *Equilibrium of a toroidal plasma with noncircular cross section*, Sov. Phys. Tech. Phys. **18** (1973) 151; Zh. Tekh. Fiz. (USSR) **43** (1973) 225

Appendix

Table of symbols and definitions

Most of the symbols used are explained where they appear, unless their meaning is assumed to be known. Here, some of the more important symbols are listed along with their definitions. Note: ψ is normalized such that $\psi = 0$ on the magnetic axis and $\psi = 1$ at the plasma boundary. The symbol R_p refers to the pole of the toroidal coordinate system and does not necessarily coincide with R_0, the major radius of the tokamak.

Symbol	*Unit*	*Definition*
A_p	{m^2}	Area of a poloidal plasma cross-section: $\int_{\psi \le 1} dRdZ$
V_p	{m^3}	Plasma volume: $2\pi \int_{A_p} R\, dA$
I_p	{A}	Total current: $\int_{A_p} j_\phi\, dA$
a_{min}	{m}	Minor radius: $(R_{max}(\psi = 1) - R_{min}(\psi = 1))/2$
b_{min}	{m}	Minor radius: $(Z_{max}(\psi = 1) - Z_{min}(\psi = 1))/2$
R_{geo}	{m}	Position of pl. bound.: $(R_{max}(\psi = 1) + R_{min}(\psi = 1))/2$
Z_{geo}	{m}	Position of pl. bound.: $(Z_{max}(\psi = 1) + Z_{min}(\psi = 1))/2$
R_{cur}	{m}	Current centre: $\left[\frac{1}{I_p} \int_{A_p} R^2 j_\phi\, dA\right]^{1/2}$
Z_{cur}	{m}	Current centre: $\left[\frac{1}{I_p} \int_{A_p} Z j_\phi\, dA\right]$
R_{mag}	{m}	Position of magnetic axis: $R(\psi = 0)$
Z_{mag}	{m}	Position of magnetic axis: $Z(\psi = 0)$
δ	{dimensionless}	Normalized Shafranov shift: $[R_{mag} - R_{geo}]/a_{min}$
ε	{dimensionless}	Inverse aspect ratio: a_{min}/R_{geo}

Symbol	*Unit*	*Definition*
$q = q_\psi$	{dimensionless}	Safety factor: $\frac{1}{2\pi} \int_{\substack{\psi=\text{const} \\ \phi=\text{const}}} \frac{1}{R} \frac{B_\phi}{B_\theta} ds$
q_{cyl}	{dimensionless}	Cylindrical safety factor: $\frac{2A_p B_\phi}{\mu_0 R_{geo} I_p}$
s	{dimensionless}	Shear: $\frac{\rho}{q} \frac{\partial q}{\partial \rho}$
β	{dimensionless}	Local beta: $\frac{2\mu_0 p}{B^2}$
β_t	{dimensionless}	Toroidal beta: $\frac{2\mu_0 \langle p \rangle}{B_\phi^2}$, $\langle p \rangle = \frac{1}{V_p} \int_{V_p} p(V)\, dV$
β_p	{dimensionless}	Poloidal beta: $\frac{2\mu_0 \langle p \rangle}{\langle B_\theta \rangle^2}$, $\langle B_\theta \rangle = \frac{\mu_0 I_p}{L}$, $L = \int_{\partial A_p} dl$
l_i	{dimensionless}	Internal induction: $\frac{4\pi}{R_{cur} \mu_0^2 I_p^2} \int_{A_p} B_\theta^2 R\, dA$
Λ	{dimensionless}	Shafranov parameter: $\beta_p + \frac{1}{2} l_i$